COMPUTATIONAL MODELING AND RATIONAL DESIGN OF FLEXOELECTRIC METAMATERIALS AND DEVICES

Alice Mocci

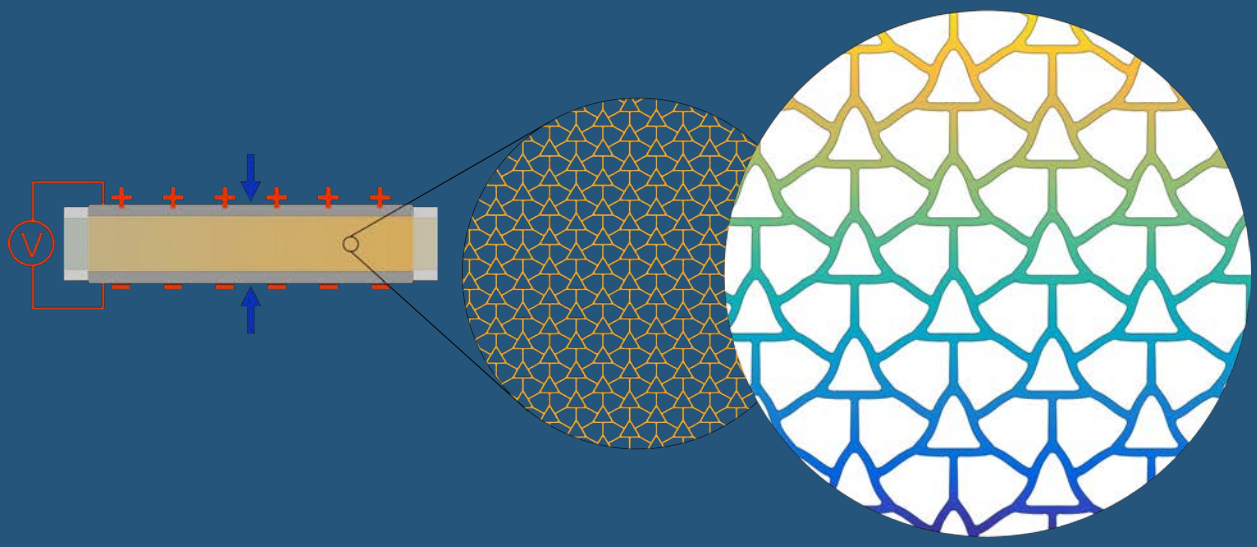

Doctoral Thesis
Barcelona, June 2021

UNIVERSITAT POLITÈCNICA DE CATALUNYA BARCELONATECH

Computational modeling and rational design of flexoelectric metamaterials and devices

Alice Mocci

COMPUTATIONAL MODELING AND RATIONAL DESIGN OF FLEXOELECTRIC METAMATERIALS AND DEVICES

Alice Mocci

Doctoral Thesis
Advisor: Irene Arias
Barcelona, June 2021

Doctoral degree in Civil Engineering
Department of Civil and Environmental Engineering
Universitat Politècnica de Catalunya

UNIVERSITAT POLITÈCNICA DE CATALUNYA

Abstract

Computational modeling and rational design of flexoelectric metamaterials and devices

by Alice Mocci

Piezoelectricity, the two-way coupling between electric polarization and strain is the basic mechanism behind most electromechanical transduction technologies. It is possible only in a limited number of materials, namely those exhibiting a non-centrosymmetric atomic or molecular structure. Flexoelectricity, the two-way coupling between strain gradient and polarization, and conversely polarization gradient and strain, is a universal property of all dielectrics. For most materials the flexoelectric coupling is relatively weak, and thus requires large gradients, which are attainable at small scales. Flexoelectricity thus provides a route to design alternative materials and devices for electromechanical transduction exploiting field gradients at small scales, by itself or as a complement to piezoelectricity. It also broadens the class of materials that can be used in these applications, overcoming the limitations of piezoelectrics regarding biocompatibility, toxicity and operating temperature. The present thesis focuses on exploring theoretically the engineering concepts for the rational design of piezoelectric metamaterials and devices exploiting the flexoelectric effect in general dielectrics, including non-piezoelectrics.

This work relies on the premise that the material polarity required for an effective piezoelectric response, can be imprinted in the metamaterial through material architecture at the microscale, thus eliminating the need for a non-centrosymmetric atomic and molecular structure of the base-material. This concept is explored in detail and demonstrated in the thesis through accurate self-consistent simulations, showing that significant effective piezoelectricity can be achieved in non-piezoelectrics by accumulating the flexoelectric response of small features under bending or torsion. This thesis proposes low area-fraction bending-dominated piezoelectric 2D periodic lattice metamaterial designs. The effective piezoelectric response is quantified and the effect of lattice geometry, orientation, feature size and area-fraction is revealed. Through computational homogenization, the full effective piezoelectric tensor is characterized, and a simple shape optimization study is presented, showing significant enhancements relative to the initial designs. Designs for flexoelectric devices combining multiple materials are also proposed, analyzed and quantified. As a possible building block for three-dimensional metamaterials, the flexoelectric response of bars under torsion is studied in detail, identifying the conditions under which such a response is possible. Furthermore, this study has allowed us to propose an experimental setup to quantify the elusive shear flexoelectric coefficient, one of the three independent components in cubic flexoelectric systems.

Acknowledgements

At first, I would like to express my sincere gratitude to my supervisor, Prof. Irene Arias for sharing her deep knowledge enthusiastically, for creating an enjoyable environment that stimulates original thinking and initiatives, and for allowing me to work on such a challenging project. I truly appreciate her humanity and politeness, and her being continuously supportive, and patient.

I also want to acknowledge Dr. Amir Abdollahi for his kindness, support, and precious advice during the first years of my research. I am grateful for all the enjoyable moments and to have had the opportunity to work with him.

I extend my gratitude to Prof. Sonia Fernández-Méndez and my closer colleagues David, Jordi, and Prakhar. I enjoyed debating with them and I truly appreciate their constant support and help.

I want to thank all my friends, for their true friendship and all the great shared moments. A special thanks to Caterina, for being the most amazing officemate, for her unfailing good humor, the relaxing coffee breaks and the happy times. To Carmen, my favorite flatmate and Spanish teacher other than a true friend, for all the wonderful memories.

I finally owe my heartfelt thankfulness to Luca and my family for their unconditional love, support, and encouragement throughout all these years.

I gratefully acknowledge the financial support of the European Research Council (Starting Grant 679451 to Prof. Irene Arias).

Contents

Abstract iii

Acknowledgements v

1 Introduction 1
- 1.1 Motivation . . . 1
- 1.2 Flexoelectricity: state of the art . . . 4
  - 1.2.1 Evidence of flexoelectricity in various materials . . . 5
  - 1.2.2 Characterization of flexoelectricity . . . 7
  - 1.2.3 Harnessing flexoelectricity as a functional property . . . 10
  - 1.2.4 Coexistence and competition between flexoelectricity and piezoelectricity . . . 12
- 1.3 Objectives of the thesis . . . 13
- 1.4 Chapter overview . . . 15
- 1.5 List of publications . . . 15
  - 1.5.1 Publications derived from this thesis . . . 15
  - 1.5.2 Other related publications . . . 16
- 1.6 Patents . . . 16
- 1.7 Conference proceedings . . . 16

2 Continuum model and two computational approaches for flexoelectricity 19
- 2.1 Continuum model . . . 19
- 2.2 Variational models . . . 20
  - 2.2.1 Direct flexoelectric form . . . 20
  - 2.2.2 Lifshitz-invariant flexoelectric form . . . 23
- 2.3 Numerical methods . . . 25
  - 2.3.1 Immersed boundary hierarchical B-splines approach . . . 26
    - Nitsche's method . . . 26
    - B-spline basis functions . . . 27
    - Immersed boundary method . . . 28
  - 2.3.2 Meshfree approximation scheme . . . 29

3 Flexoelectricity-based piezoelectric metamaterials and devices 31
- 3.1 Introduction . . . 31
- 3.2 Flexural scalable flexoelectric transducers . . . 33
- 3.3 Geometrically polarized architected dielectrics with effective piezoelectricity 34
  - 3.3.1 Theoretical model and setup . . . 35
  - 3.3.2 Bending-dominated non-centrosymmetric lattices . . . 37
  - 3.3.3 Anisotropy and area fraction . . . 39
  - 3.3.4 Effective piezoelectric performance . . . 41

3.3.5 Generalized-periodic boundary conditions, validation and convergence 42
Generalized-periodic boundary conditions . . . 42
Validation . . . 44
Convergence . . . 44
3.4 Concluding remarks . . . 45

4 Computational homogenization of flexoelectric metamaterials 47
4.1 Introduction . . . 47
4.2 Energy equivalence . . . 48
4.3 Effective material tensors in the homogenized piezoelectric medium . . . 51
4.3.1 Computational homogenization: numerical approach . . . 52
4.4 Results and Discussions . . . 53
4.4.1 Surface representation and symmetries . . . 53
4.4.2 Effect of the nominal material properties . . . 55
4.5 Concluding remark . . . 59

5 On-going work 61
5.1 Optimization methods . . . 61
5.1.1 Gradient-based methods . . . 61
5.1.2 Genetic, population-based methods . . . 63
5.2 Shape optimization of Design D′ . . . 64
5.2.1 Longitudinal operation mode . . . 65
5.2.2 Effect of the nominal material properties on the geometrically polarized lattice . . . 66
5.3 On-going work . . . 69
5.3.1 Transverse and shear operation mode . . . 69

6 Towards 3D flexoelectric metamaterials and devices: flexoelectricity under torsion 71
6.1 Torsion of a conical shaft with general cross section . . . 72
6.2 Self consistent quantification of flexoelectric roads under torsion . . . 73
6.3 Chasing the elusive shear flexoelectricity . . . 79
6.4 Concluding remarks . . . 84

7 Conclusions and future work 87
7.1 Future work . . . 88

A Immersed boundary B-Spline framework 91
A.1 Material tensors . . . 91
Elasticity tensor **C** . . . 91
Strain gradient elasticity tensor **h** . . . 91
Dielectricity tensor $\boldsymbol{\kappa}$ . . . 92
Electric field gradient dielectricity **b** . . . 92
Flexoelectricity tensor $\boldsymbol{\mu}$ . . . 92
A.1.1 Strain gradient elasticity and electric field gradient dielectricity: sensitivity analysis . . . 92
Cantilever beam bending . . . 92
Bending-dominated lattice metamaterials . . . 93

B Piezoelectric coefficients and boundary conditions derivation for the homogenized RVE **95**
B.1 Piezoelectricity . . . 95
B.1.1 Energy forms . . . 95
Internal energy $\mathcal{U}\ (\boldsymbol{\varepsilon}, \mathbf{D})$, h-form . . . 95
Gibbs energy $\Phi\ (\boldsymbol{\sigma}, \mathbf{E})$, d-form . . . 96
Electric enthalpy $\mathcal{H}\ (\boldsymbol{\varepsilon}, \mathbf{E})$, e-form . . . 97
Elastic Gibbs function $\mathcal{G}_1\ (\boldsymbol{\sigma}, \mathbf{D})$, g-form . . . 97
B.1.2 Relationship between piezoelectric tensors . . . 98
B.2 Tensor surface representation . . . 99

C Meshfree approximation method **101**
C.1 Material characterization . . . 101
Elasticity tensor $\mathbf{C}$ . . . 101
Dielectricity tensor $\boldsymbol{\kappa}$ . . . 101
Flexoelectricity tensor $\boldsymbol{\mu}$ . . . 101
Gradient operators $\mathbf{B_u}$ and $\mathbf{B}_\phi$ . . . 102
Hessian operators $\mathbf{H_u}$ and $\mathbf{H}_\phi$ . . . 102
C.2 Derivation of the elastic torsion problem in cylindrical coordinates . . . 102
C.3 Mesh and convergence . . . 103

Bibliography **105**

List of Figures

1.1 Electromechanical systems, adapted from Dagdeviren et al.[1]. 1
1.2 Comparison of the main distinctive features of piezoelectricity, electrostriction and flexoelectricity. 3
1.3 Number of publications on flexoelectricity from 1974 to 2020. Data has been obtained from `https://www.scopus.com/`. 4
1.4 Flexoelectric mechanism in liquid crystals (LCs). 5
1.5 Flexoelectricity in cellular membranes. 6
1.6 Flexoelectricity in stereocilia in inner hair cells. 6
1.7 Flexoelectricity in bones. 7
1.8 Flexoelectricity in hard materials. 7
1.9 Quantification of transverse and longitudinal flexoelectricity 9
1.10 Deformation mode in truncated pyramid under compression. 10
1.11 Piezoelectric vs flexoelectric high-frequency bending resonator [42]. 10
1.12 Polarization switching in ferroelectric thin films due to flexoelectricity [51]. . 11
1.13 Nonpiezoelectric 2D sheets with circular and triangular inclusions 11
1.14 Piezoelectric composites based on flexoelectricity. 12
1.15 Interplay between piezoelectricity and flexoelectricity. 13
1.16 A properly designed flexoelectric metamaterial behaves as a piezoelectric material at the macroscale. An electrical output is generated when a homogeneous deformation is applied, or conversely it deforms under a uniform electrical bias. 14

3.1 Publications on *lead-free piezoceramics*, from `https://www.scopus.com/`. . . . 32
3.2 Sketch of a piezoelectric device. 32
3.3 Scalable effect in thin structural elements under bending 33
3.4 Scalable flexoelectric device. 34
3.5 Schematic depiction of a periodic metamaterial in sensor or actuation mode . 35
3.6 Illustration of the generalized-periodic boundary conditions on a unit cell of the periodic metamaterial. 36
3.7 Electric potential and displacements in centrosymmetric and non-centrosymmetric devices under an applied deformation (sensor mode) and electric field (actuator mode). 37
3.8 Geometrical parameters of the unit cell. 37
3.9 Electric field and $y-$displacement plotted on the deformed configuration for various material designs in sensor and actuator mode. 38
3.10 Anisotropy of the effective piezoelectric coefficient in sensor and actuator mode for Designs A to D. 40
3.11 Systematic examination of effective piezoelectric response of the architected dielectrics, considering the optimal orientation and varying area fraction. . . 41

3.12 Representative volume element (RVE) or unit cell of lattice design D. 43
3.13 Electric potential jump as a function of the number of vertically stacked unit cells for lattice Design C in displacement sensor mode. 44
3.14 Relative error of two quantities of interest as a function of the element mesh size h. The inset shows three representative computational mesh details. All simulations in this work have been computed with mesh level M1. 45

4.1 Heterogeneous structure and its equivalent homogeneous medium. 47
4.2 Effective elasticity, dielectricity and piezoelectricity tensors for Design A and their surface representation. 53
4.3 Effective elasticity, dielectricity and piezoelectricity tensors for Design B and their surface representation. 54
4.4 Effective elasticity, dielectricity and piezoelectricity tensors for Design C and their surface representation. 55
4.5 Effective elasticity, dielectricity and piezoelectricity tensors for Design D and their surface representation. 56
4.6 Effective elasticity, dielectricity and piezoelectricity tensors for Design D′ and their surface representation. 56
4.7 Non-zero independent components for the dielectricity, elasticity and piezoelectricity tensors as a function of the nominal Young's modulus. 58
4.8 Non-zero independent components for the dielectricity, elasticity and piezoelectricity tensors as a function of the nominal Young's modulus. 59

5.1 Gradient-based algorithm for optimization. 62
5.2 At each step the trust region is identified in order to better approximate the objective function $f(x_k)$. The picture has been taken from `https://optimization.mccormick.northwestern.edu/index.php/Trust-region_methods`. 63
5.3 Population-based algorithm for optimization and terminology. 64
5.4 The geometrical configuration of the most performant lattice design D′ is defined by 8 parameters. 65
5.5 Shape optimization process for design D′ in longitudinal sensor h_{22} and g_{22} operation mode. A slab of the dimension of $L = 10 \times 10\mu$m have been extracted from our 2D lattice, therefore the resulting optimal shapes are in the same scale and have the same fixed thickness $t = 160$nm. 66
5.6 Shape optimization process for design D′ in longitudinal actuator d_{22} and e_{22} operation mode. A slab of the dimension of $L = 10 \times 10\mu$m have been extracted from our 2D lattice, therefore the resulting optimal shapes are in the same scale and have the same fixed thickness $t = 160$nm. 67
5.7 Cubic flexoelectric tensor 67
5.8 69
5.9 Shape optimization process for design D′ in transverse d_{122} and shear d_{121} operation mode. A slab of the dimension of $L = 10 \times 10\mu$m have been extracted from our 2D lattice, therefore the resulting optimal shapes are in the same scale and have the same fixed thickness $t = 160$nm. 70

6.1 Prismatic shaft under an applied constant torque T. The Cartesian $(Ox_1x_2x_3)$ and the cylindrical $(O\rho\theta z)$ reference systems are also reported. 72

6.2 Twisting of a bar under an applied torque T around the z-axis. The infinitesimal angle $d\phi$ is the angle of torsion between a pair of cross-sections with the infinitesimal distance dz apart. Cylindrical (ρ, θ, z) coordinate system is depicted. 74
6.3 Electric potential distribution in (a) circular cross-section and (b) square cross-section. Electric potential is not generated in these setups.For visualization purposes, deformations are amplified by a factor of 30. 75
6.4 Cone geometrical parameters, R_1, R_2 and L. 75
6.5 Distribution of electric potential for (a) anisotropic flexoelectricity and (b) isotropic flexoelectricity. A non-ferroelectric electric potential pattern is observed for the case of anisotropic flexoelectricity only. Isotropic elastic properties and circular cross-section are considered to isolate flexoelectric anisotropy from other sources of material or geometrical anisotropy.For visualization purposes, deformations are amplified by a factor of 30. 75
6.6 Vector plot of the electric displacement $\mathbf{D} = \boldsymbol{\mu}\nabla\boldsymbol{\varepsilon} - \kappa\nabla\phi$ along a circle on the cross-section not located on the lateral surface of the cone. Both individual contributions to $\mathbf{D}$ are shown, the first one is decomposed into the angular and radial components, $(\boldsymbol{\mu}\nabla\boldsymbol{\varepsilon})_\theta = \boldsymbol{\mu}\nabla\boldsymbol{\varepsilon} - \boldsymbol{\mu}\nabla\boldsymbol{\varepsilon}\cdot\mathbf{n}$ and $(\boldsymbol{\mu}\nabla\boldsymbol{\varepsilon})_\rho = \boldsymbol{\mu}\nabla\boldsymbol{\varepsilon}\cdot\mathbf{n}$, $\mathbf{n}$ being the outward unit normal to the circular cross-section. 76
6.7 Distribution of electric potential in a truncated cone under (g) compression and (h) bending. The yellow arrows represent the polarization direction. The applied displacements are represented by the black arrows. For visualization purposes, deformations are amplified by a factor of 30. 76
6.8 (a) Distribution of electric potential in three different simulations with flexoelectric tensors rotated different angles $\theta = 0, \pi/6$ and $\pi/4$, respectively. (b) Maximum magnitude of electric potential as a function of the flexoelectric anisotropy parameter for different geometrical configurations. 78
6.9 Maximum magnitude of electric potential on the surface as a function of the geometrical parameters. 79
6.10 Truncated cone having radius R_1, R_2, respectively and length L. A ground electrode is placed on the clamped end of the shaft while a torque T is applied on the free-end. 80
6.11 Distribution of the electric potential ϕ in a half truncated cone where a constant torque is applied on the right-end while the displacement and electric potential are fixed on the left end. 81
6.12 Longitudinal and radial polarization in a half truncated cone under torsion. . 82
6.13 a) Deviation between the simulation and analytical results as a function of the longitudinal μ_l and transversal μ_t flexoelectric coefficients. (b) Cross-sections of the deviation plot where $\mu_l = 0$ (right) and $\mu_t = 0$ (left). 84

7.1 Electric potential distribution in the 3D extruded scalable flexoelectric device under bending. 89

A.1 Flexoelectric cantilever beam with thickness $t = 160$nm. (a) Sensor mode, a force F is enforced at the free end of the cantilever beam, the electric potential ϕ, reported in the contour plot, is measured at the top surface. (b) Actuator mode, an electric potential V is applied on the top face, while the bottom side has been grounded. The deflection φ is measured. 93
A.2 Sensitivity analysis for Design D, with $t = 40$nm and $t = 400$nm. 94

B.1 Spherical reference system $Or\theta\phi$. 100

C.1 (a) The rotation of the structured mesh by an angle $\zeta = 20$ degrees does not affect the generation of the patterns in the electric potential distribution. Yellow lines have been added to highlight the rotation of the mesh. (b) Convergence study of the numerical simulations. The electric potential distribution does not change upon mesh refinement. 104

List of Tables

1.1 Centrosymmetric and non-centrosymmetric point groups 4

3.1 Material parameters 34
3.2 Material parameters 36

4.1 Numerical boundary conditions used to determine the unknown concentration tensors and their derivatives. 52
4.2 Effective tensors coefficients 57

5.1 Lower and upper bounds for the 8 design variables selected as minimizers for this problem. 65
5.2 Lower and upper bounds for the 7 design variables selected as minimizers for this problem. 68

6.1 Barium Strontium Titanate (BST). Material parameters. 74
6.2 f coefficients 83

A nonno Antonino,
che oggi sarebbe fiero di me.

Chapter 1

Introduction

1.1 Motivation

The electromechanical coupling, the link between electrical and mechanical properties, plays an essential role in the physics of solids and their practical applications. This effect exists in a wide variety of materials, natural as well as artificial, which are capable of converting mechanical energy into electrical and vice-versa, termed *electro-active materials*. Nowadays, their technological uses are manifold, including *energy harvesting* by which the ambient energy (e.g. mechanical, wind, solar, body movement) is converted and stored into electrical energy, *sensing* where a mechanical input, such as stress, is converted in an electrical output, and *actuation* where an applied electric field produces a controlled mechanical output, e.g. a force. Figure 1.1, taken from Dagdeviren et al. [1], shows a few of the possible applications.

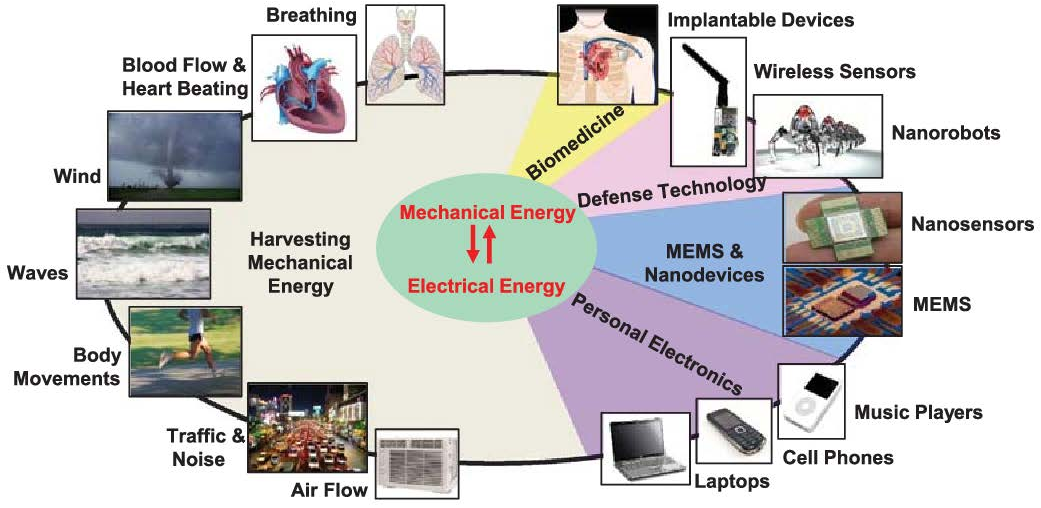

FIGURE 1.1: Electromechanical systems convert electrical energy into mechanical and vice-versa. Some example of conversion and storage of mechanical energy into electrical (energy harvesting) and some usage as sensors/actuators are shown. The figure was adapted from Dagdeviren et al.[1].

The most well-known and widely used electromechanical coupling is piezoelectricity [2–4], by which some materials polarize under the application of homogeneous stress. Mathematically, it is written as the linear relationship between the stress σ and the polarization $\mathbf{P}$

$$P_l = d_{lij}\sigma_{ij,}$$

where **d** is the third-rank tensor of piezoelectricity [5]. The converse effect also exists, i.e. piezoelectric materials deform under an applied electrical field **E**,

$$\varepsilon_{ij} = d_{lij} E_l,$$

where $\boldsymbol{\varepsilon}$ is the strain tensor. Note that piezoelectric deformation reverses sign upon electric field sign reversal, and it is scale-invariant. Consistent with the odd-rank nature of the piezoelectric tensor, piezoelectricity is possible only in materials exhibiting a non-centrosymmetric atomic or molecular structure. For instance, in the case of ionic crystals, only 20 of the 32 point groups are piezoelectric, Table 1.1, and only a few of them exhibit good piezoelectric properties. The best known piezoelectrics are ferroelectric ceramics, which are ubiquitous in current technologies, but are brittle, many of them lead-based, and exhibit a limited range of operating temperatures [6, 7]. European and international regulation have incited a quest for lead-free piezoelectric materials (Restriction of Hazardous Substances Directive). Although significant progress has been made, the wide replacement of the most used piezoelectric PZT (60% lead) is still far away [8–11].

Another electromechanical coupling which has received significant attention in soft materials is electrostriction or Maxwell-stress effect [12]. It refers to the electrostatic forces arising from the Coulombic attraction of charges of opposite sign at the electrodes leading to deformation, Fig. 1.2. Mathematically, the electrostrictive stress depends quadratically on the polarization, and thus does not reverse sign upon polarization sign reversal (contrary to piezoelectricity). Although electrostriction is present in all dielectrics, its effect is weak and only significant in soft materials, such as dielectric elastomers or piezoelectric polymers. In addition, it is not a two-way coupling as piezoelectricity, since deformation does not produce an electric field, and thus electrostriction cannot be used for sensing applications.

The study of piezoelectricity has a long history in mechanics of materials since it was first demonstrated by Pierre and Jacques Curie in 1880. In the last decades, a third electromechanical coupling is receiving increasingly attention, namely flexoelectricity.

Flexoelectricity, is a reversible two-way coupling effect not restricted by symmetry and thus possible in all dielectrics. It couples polarization and strain gradient through the fourth-order flexoelectric tensor $\boldsymbol{\mu}$

$$P_i = \mu_{ijkl} \varepsilon_{ij,k}.$$

Converse flexoelectricity couples polarization gradient and stress

$$\sigma_{ij} = \mu_{ijkl} P_{k,l}.$$

Figure 1.2 summarizes and compares the main features of the three mentioned couplings. Since field gradients are able to break centrosymmetry in nominally centrosymmetric materials, flexoelectricity is possible in all dielectrics. Nevertheless, flexoelectricity is weak in most materials, and thus requires large gradients to be significant by itself, which are only attainable at small scales in stiff materials.

Recent advances in nanotechnology and the continuous development of nanomaterials potentially enable to exploit the flexoelectric effect in micro- (MEMS) and nano-electromechanical systems (NEMS). With these advances, flexoelectricity provides a route to designing alternative materials and devices for electromechanical transduction exploiting gradients, by itself or as a complement to piezoelectricity. It also broadens the class of materials that can be

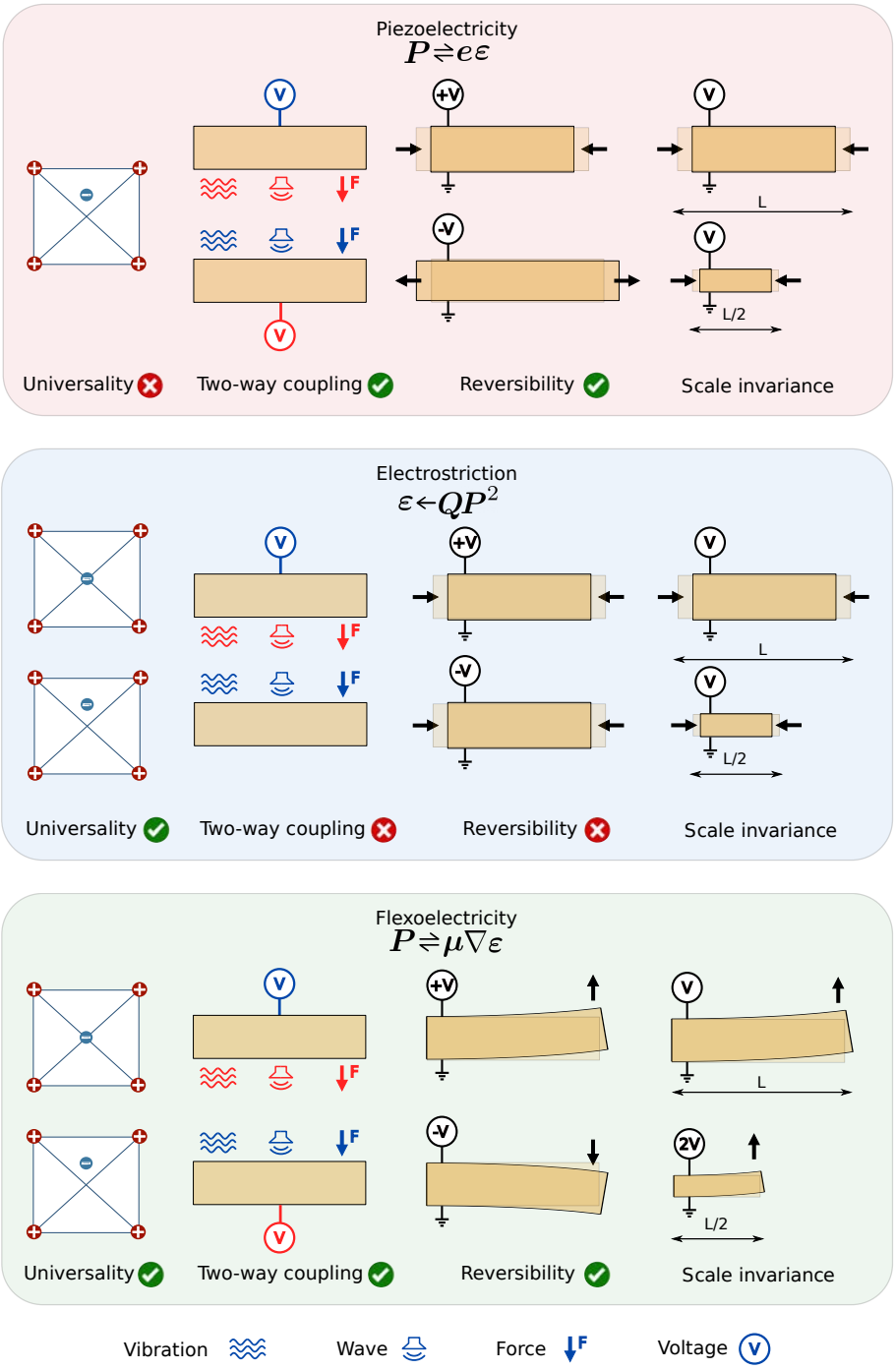

FIGURE 1.2: Comparison of the main distinctive features of piezoelectricity, electrostriction and flexoelectricity. These features are illustrated in ionic crystals, for simplicity. *Universality*: piezoelectricity is possible only in materials exhibiting a non-centrsymmetric atomic, while electrostriction and flexoelectricity are universal for dielectrics. Nevertheless, Flexoelectricity is significant at small scales and electrostriction is significant only in soft materials. *Two-way coupling*: electrostriction is a one-way coupling. A mechanical output can be generated by applying a voltage, but a mechanical load does not produce any polarization. In contrast, both piezoelectricity and flexoelectricity are two-way coupled, they can equally behave as sensors or actuators. *Reversibility* represents the capability to switch the sign of the output by reversing the input. Electrostriction, due to its quadratic form, does not have this ability. *Scale invariance*: flexoelectricity, in contrast to piezoelectricity and electrostriction, mobilizes gradients and thus is a scale-dependent phenomenon significant only at sub-micron scales. The figure was adapted from [13].

used in these applications, overcoming the limitations of piezoelectrics regarding biocompatibility, toxicity and operating temperature. Hence, by exploiting field gradients at small scale features, one can envision metamaterials and devices that effectively behave as piezoelectrics at the macroscale but are built from non-piezoelectric materials specifically chosen to meet other application requirements.

TABLE 1.1: Centrosymmetric and non-centrosymmetric point groups

Point groups		
Centrosymmetric	Non-centrosymmetric (piezoelectric)	Crystal system
$\bar{1}$	1	Triclinic
$2/m$	$2, m$	Monoclinic
mmm	$222, mm2$	Orthorombic
$4/m, 4/mmm$	$4, \bar{4}, 422, 4mm, \bar{4}2m$	Tetragonal
$\bar{3}, \bar{3}m$	$3, 32, 3m$	Trigonal
$6/m, 6/mmm$	$6, \bar{6}, 622, 6mm, \bar{6}m2$	Hexagonal
$m3, m3m$	$23, \bar{4}3m, 432$	Cubic

1.2 Flexoelectricity: state of the art

Flexoelectricity was discovered barely 60 years ago by Mashkevich and Tolpygo [14]. In the 1960s, the first phenomenological theory was formulated by Kogan [15] and the first experimental demonstration of the effect was presented by [16], but it is only in the last decades, concomitantly with the advent and progress of nanotechnologies, that the interest in this field has increased significantly and continues today, as shown in Fig. 1.3 which reports the number of scientific publications on flexoelectricity from 1974 to 2020 (source https://www.scopus.com/). In the following sections, the main aspects and latest discoveries about flexoelectricity will be reviewed.

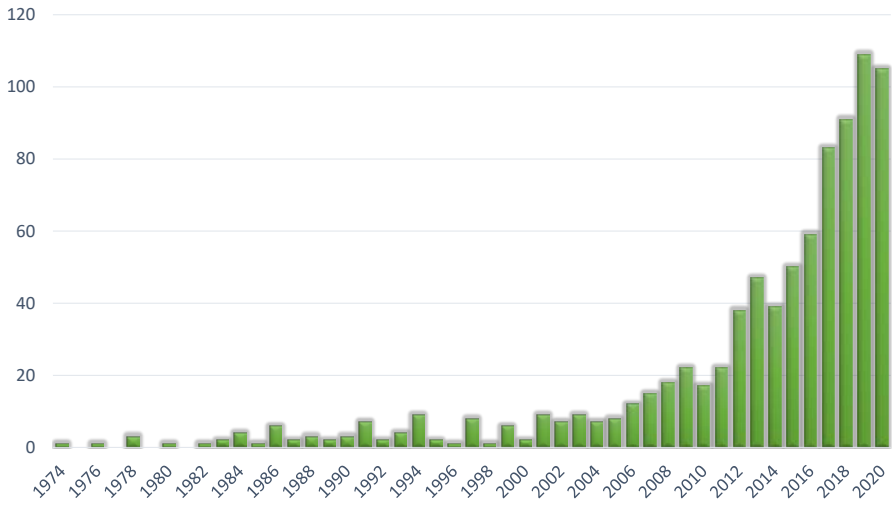

FIGURE 1.3: Number of publications on flexoelectricity from 1974 to 2020. Data has been obtained from https://www.scopus.com/.

.

1.2.1 Evidence of flexoelectricity in various materials

The very first evidence of flexoelectricity dates back to 1968 when Bursian [16] performed a series of tests on Barium Titanate $BaTiO_3$ thin films. In these experiments the crystals were treated as actuators, namely, an electric field was applied in the transversal direction, leading to inhomogeneous deformation (bending) in the samples. Since then, flexoelectricity has been observed in a wide variety of materials.

Flexoelectricity in liquid crystals. In 1969, a strain gradient coupling was predicted by Meyer [17] while investigating the piezoelectric effect in a particular class of soft materials called liquid crystals (LCs). The mechanism in liquid crystals is explained in Fig. 1.4 [18], adapted from Meyer [17]. In both pear and banana shapes, each molecule is polarized due to its asymmetric form. However, in a tension-free configuration Fig. 1.4(a,c) the molecules are oriented in such a way that the overall polarization is zero. Conversely, when an inhomogeneous deformation such as a splay or a bending is applied Fig. 1.4(b,d), the most energetically convenient configuration ensures that the molecules rotate, re-orienting themselves and generating more dipoles aligned in the same direction thus leading to a net non-zero polarization. The rotation of the asymmetric shapes in LCs is the fundamental mechanism of flexoelectricity in soft materials and can be extended to polymers [19] such as liquid-crystal elastomers or thermoplastic and thermosetting polymers or bio-membranes [20, 21].

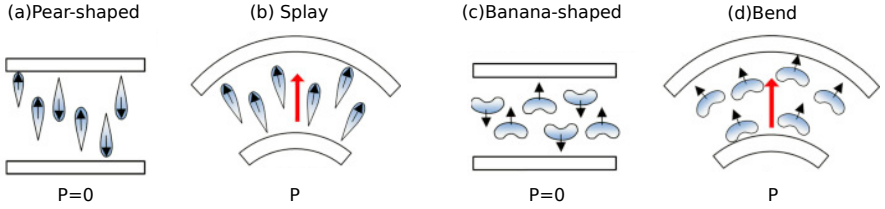

FIGURE 1.4: Flexoelectric mechanism in liquid crystals (LCs). In an undeformed configuration, the asymmetric pear (a) and banana (c) shapes are randomly oriented in such a way that the overall polarization across the bulk is zero. Under an applied inhomogeneous deformation such as a splay (b) or a bending (d), the most energetically convenient configuration leads to a rotation and re-orientation of the molecules. Therefore, the majority of the dipoles are aligned in the same direction resulting in an overall non-zero polarization. The figure has been adapted from Huang et al. [18].

Flexoelectricity in biological systems. Many important biological systems manifest relevant electromechanical behaviors attributable to flexoelectricity. The cellular membrane itself is a lipid bilayer that behaves similarly to liquid crystals [22, 23]. In Fig. 1.5, adapted from Chen et al. [23] the membrane behavior is shown. A spontaneous membrane curvature generates a strain gradient field that activates a mechanism similar to that of LCs. The molecules of the cellular membranes re-orient themselves thus leading to an unbalance between the positive and negative dipoles and thus generating a polarization through the membrane. Both direct (curvature-induced) and converse (electric field-induced) effects are possible in cellular membranes.

Stereocilia in hair cells can be considered a biological flexoelectric sensor for sound[24]. Figure 1.6 depicts a sketch of the mechanism in the auditory system. In the inner part of the hair cell, where stereocilia are placed, the hair cell membranes convert the acoustic vibrations

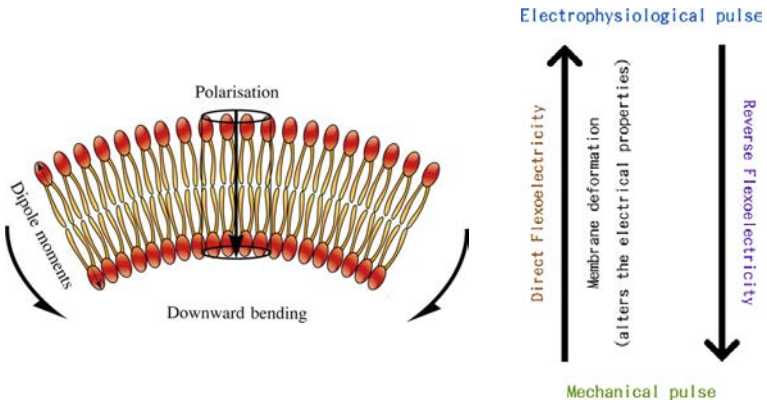

FIGURE 1.5: The bending of the membrane generates a strain gradient accountable for the re-orientation of the cellular membrane molecules, similarly to LCs. The alignment of the dipole moments in the same direction induces a polarization through the membrane. Direct flexoelectricity is responsible for that. On the contrary, the converse effect might lead to changes in the spontaneous curvature due to the application of electrophysiological impulses. The figure was adapted from Chen et al. [23].

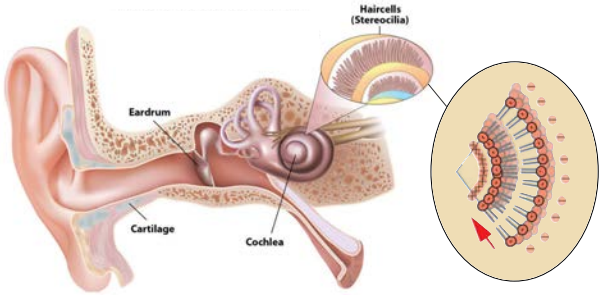

FIGURE 1.6: Stereocilia in inner hair cells are flexoelectric sensors able to convert mechanical vibrations into electrical signals. The stereocilia membrane undergoes bending produces an action potential due to the flexoelectric effect. Credit for the figure at the following link and adapted from Breneman et al.[24].

into electrical signals thus amplifying the sound. Neuronal activities are also influenced by ultrasound. Neurons are driven under an action potential that might be associated with an electromechanical coupling other than chemical and electrical pulses [25].

Recently, Vasquez et al. [26] suggested that the effective piezoelectricity of bone may emerge from microscopic flexoelectricity. The giant strain gradients produced in the vicinity of a microcrack generate a substantial electric field to start the crack-healing and drive the process responsible for the mineralization of the bone. A sketch of the mechanism attributable to flexoelectricity is shown in Fig. 1.7.

Flexoelectricity in hard materials. Flexoelectricity in ionic crystal has a different origin than that of soft materials. When a non-uniform deformation (e.g. bending) is applied on a two-dimensional plate the difference in tensions between the upper part (stretched) and the bottom (compressed) will generate a strain gradient in the transversal direction. Due to flexoelectricity, a polarization, having the same direction of the applied strain gradient, will be generated. This mechanism can be readily explained by considering the centrosymmetric ionic crystal structure, depicted in Fig. 1.8. The applied inhomogeneous stress is responsible for symmetry breaking of the crystalline structure, in such a way that the center of gravity of

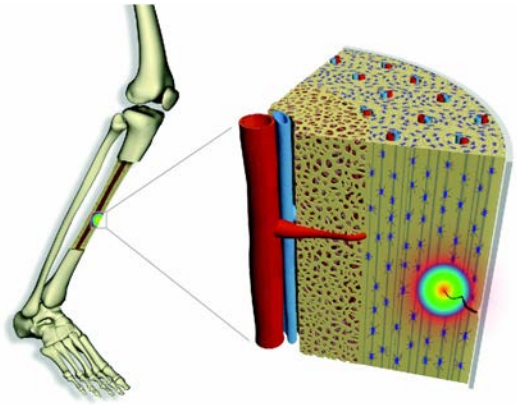

FIGURE 1.7: Flexoelectricity can be considered responsible for triggering the process of damage repair in bones. Structural singularities such as micro cracks generate strain gradients thus producing substantial electric field to activate the crack-healing process through the re-mineralization of the bone. Figure taken from Vasquez et al. [26].

the positive and negative charges relatively move, thereby generating a dipole which results in a non-zero polarization through the bulk [27].

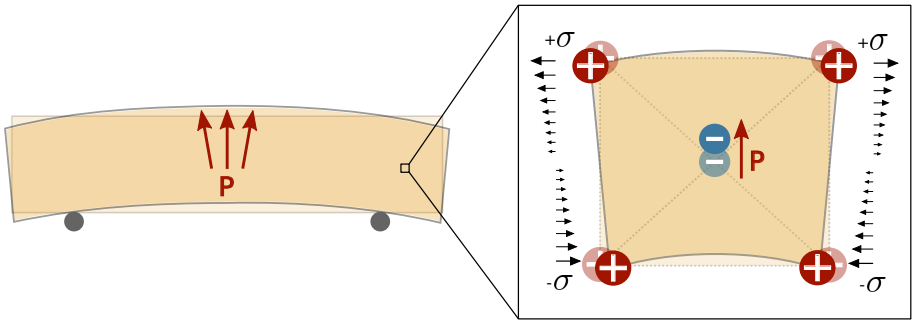

FIGURE 1.8: Flexoelectric effect in hard materials. A plate under an applied bending will polarize due to flexoelectricity. By moving deeper into the crystalline structure the mechanism can be easily explained. The crystal ionic structure is modified by the applied inhomogeneous stress in such a way that the gravity center of the positive and negative charges relatively moves, thus generating a dipole moment in the direction of the applied strain gradient.

Every crystalline material regardless of its symmetry exhibits the flexoelectric coupling. Nevertheless, the flexoelectricity is weak in most materials, and thus requires large gradients to be significant by itself, which are only attainable at small scales in stiff materials. The flexoelectric coefficients have been shown to be proportional to the dielectric constant [27], and thus flexoelectricity is expected to be stronger in ferroelectrics at their paraelectric phase.

1.2.2 Characterization of flexoelectricity

As introduced in Sec. 1.1 flexoelectricity is one of the fundamental properties of all 32 point groups of crystal structures reported in Table 1.1. The symmetries of the flexoelectric tensor have been studied by Shu et al. [31, 32] and Quang [33] considering the invariance of the fourth-order flexoelectric tensor $\mu_{ijkl} = \mu_{ikjl}$ respect to the first two indices as a consequence of the symmetry of the strain tensor. Following this approach, the flexoelectric tensor is fully

characterized once the 54 independent components for the least-symmetrical crystal system are defined, namely *triclinic* or *anorthic*.

Nevertheless, for most crystal symmetry groups the number of the independent components is considerably smaller. For instance, the strongest flexoelectric crystals, ferroelectric perovskites, in their paraelectric phase, belong to the *cubic* point group $m3, m3m$ having only three independent flexoelectric components [32, 33] called *longitudinal* μ_ℓ, *transverse* μ_t and *shear* μ_s, defined as

$$\mu_{iiii} = \mu_\ell \qquad i = 1,2,3; \tag{1.1a}$$

$$\mu_{ijji} = \mu_t \qquad i,j = 1,2,3; \quad \text{such that} \quad i \neq j \tag{1.1b}$$

$$\mu_{iijj} = \mu_{ijij} = \mu_s \qquad i,j = 1,2,3; \quad \text{such that} \quad i \neq j. \tag{1.1c}$$

A further simplification can be introduced if an isotropic flexoelectric tensor is considered. As for the elastic tensor, the independent components for the isotropic case are reduced to two so that the third one can then be expressed as a function of the other two as:

$$\mu_\ell - \mu_t - 2\mu_s = 0. \tag{1.2}$$

Even with fewer flexoelectric coefficients to determine, flexoelectricity characterization is challenging, involving difficult experiments at very small scales, and unavoidably inhomogeneous mechanical and electric fields which make their interpretation far from trivial. Indeed, simple analytical models ignoring 2D effects or the two-way coupling used in the interpretation of experiments have been shown to lead to order-of-magnitude discrepancies in the estimated flexoelectric parameters [34]. Furthermore, it is difficult to experimentally isolate flexoelectricity from other physics, including piezoelectricity from residual piezoelectric nanoregions. For all these reasons, there is currently a large dispersion in experimental characterization of flexoelectricity, and a large discrepancy between experimental measurements and theoretical predictions [27].

Most experimental and theoretical studies to date have focused on obtaining the longitudinal and transverse coefficient whereas the shear component is still most frequently neglected [27]. Until now, two different setups have been used to characterize the flexoelectric coefficients: the cantilever beam under bending and the truncated pyramid under compression [34, 35], both shown in Fig. 1.9. Measurements refer both to the *direct* effect when a voltage is induced by an applied inhomogeneous mechanical field and to the *converse* effect when instead a deformation is obtained due to an input inhomogeneous electric field. Many recent works by Ma and Cross have focused on the evaluation of the transverse flexoelectricity in different cubic perovskites [35–39] by exploiting the cantilever beam setup. The flexoelectric mechanism in a slab under bending has already been discussed in sec. 1.2.1. The non-uniform distribution of the tensions in the cross-section reported in Fig. 1.9(a), generated by the applied bending, results in a strain gradient in the transversal direction thus generating a polarization in the same direction. Therefore, the cantilever beam configuration mobilizes the transverse flexoelectric coefficient and allows to isolate it from other contributions. The resulting polarization can be measured, and thus assuming a 1D model, Fig. 1.9a, the transverse flexoelectric coefficient is expressed as:

$$\mu_{12} = \frac{P_3}{\varepsilon_{11,3}}. \tag{1.3}$$

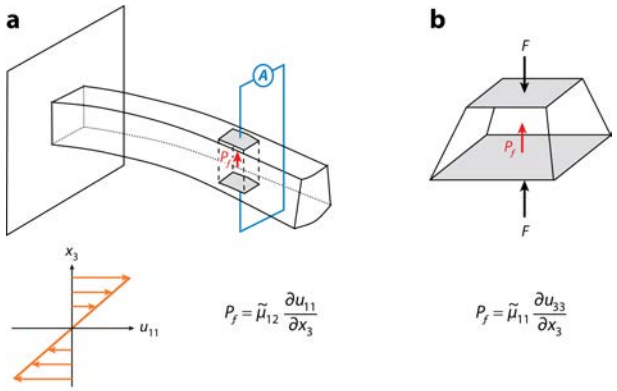

FIGURE 1.9: Quantification of transverse and longitudinal flexoelectricity. (a) Cantilever beam clamped on one side on charged at the free-end is used for the characterization of the effective transverse flexoelectric coefficient $\tilde{\mu}_{12}$. (b) Truncated pyramid under compression used for quantification of the effective longitudinal flexoelectric coefficient $\tilde{\mu}_{11}$. The figure has been taken from Zubko et al. [27]

Note that ignoring Poisson's effect allows to decouple the transverse flexoelectric coefficients. This can be a crude assumption in some cases. The measured transverse coefficient $\tilde{\mu}_{12}$ in these cases combines contributions from the nominal transverse and longitudinal coefficients as

$$\tilde{\mu}_{12} = -\nu\mu_{11} + (1-\nu)\mu_{12}, \tag{1.4}$$

being ν the Poisson's ratio. Furthermore, the strain gradients cannot be directly measured and need to be estimated from other measured quantities. In these experiments, $\varepsilon_{11,3}$ is estimated from elasticity alone, thereby neglecting the converse flexoelectric effect. Abdollahi et al. [40] have shown that using these oversimplifications in the interpretation of experimental observations can lead to order-of-magnitude overestimation of the flexoelectric coefficients.

The second most commonly used setup is a three dimensional truncated pyramid undergoing uniaxial compression [35, 41], as shown in Fig. 1.9(b). When a force F acts on the top A^t and bottom A^b surfaces of the truncated pyramid the corresponding stresses ($\sigma^t_{33} = F/A^t \neq \sigma^b_{33} = F/A^b$) acting on the two surfaces are different. Therefore, a longitudinal strain gradient is produced and consequently a polarization:

$$P_3 = \mu_{11}\varepsilon_{33,3}, \tag{1.5}$$

Abdollahi et al. [34] highlighted the limitation of this method by computationally solving the 3D pyramid. They found that the oversimplified analytical models used to obtain longitudinal flexoelectric coefficients from experimental measurements were largely overestimated, partially justifying the discrepancy with theoretical evaluations [27]. Two main sources of distortion were identified, both related to the geometrical setup and the applied boundary conditions. The first one was associated with the strongly non-uniform distribution of the gradient fields, mainly concentrated at the edges and corners. The second one is related to the deformation mode of the sample. If the support is not stiff enough and for particular geometrical configurations, the bending might also become the dominant deformation, as shown in Fig. 1.10.

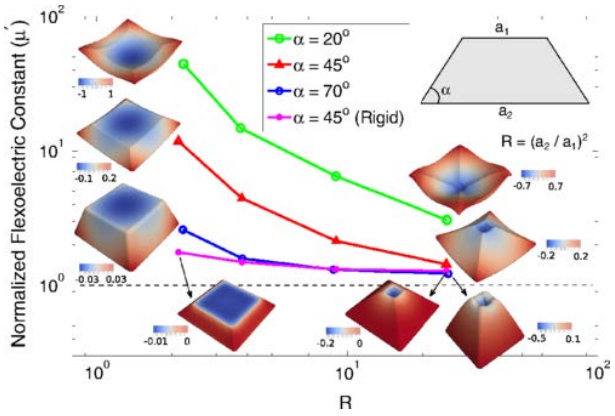

FIGURE 1.10: Deformation mode for different geometrical configurations of the truncated pyramid setup under compression. The figure was taken by Abdollahi et al. [34].

1.2.3 Harnessing flexoelectricity as a functional property

Sophisticated and generally expensive equipments required for manufacturing, as well as several remaining open questions related with flexoelectricity, still limit the presence of flexoelectric devices in technology. However, fabrication of technological devices is progressively moving toward smaller scales, where flexoelectricity is not negligible.

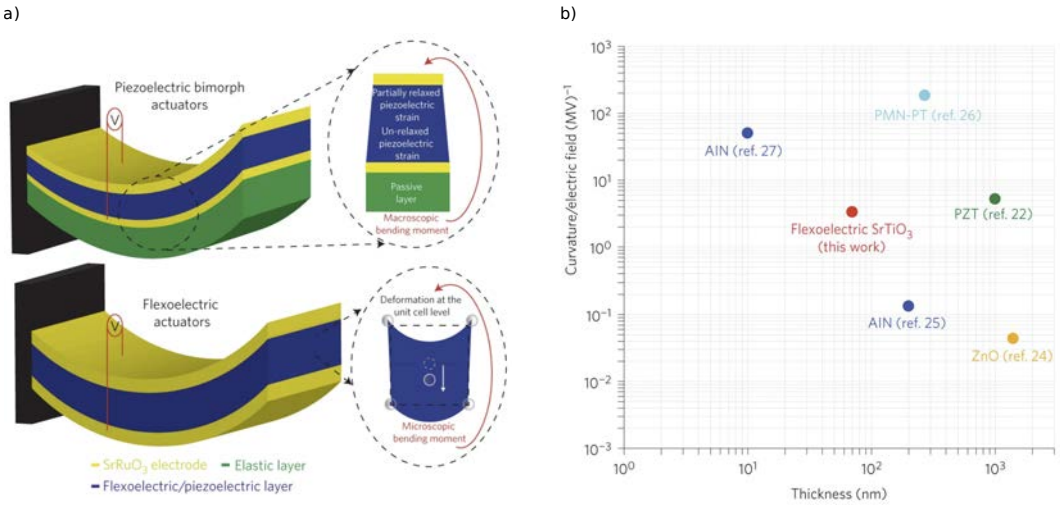

FIGURE 1.11: (a) Piezoelectric and flexoelectric actuators. The electrical voltage applied on the piezoelectric layer generates a strain, converted into a strain gradient (and thus a flexural deformation) due to the elastic non-piezoelectric layer clamped to the piezoelectric bimorph. On the other hand, the flexoelectric actuator achieves bending by breaking the centrosymmetry at the unit cell level and does not require to be clamped to any support. (b) the performance of the flexoelectric device is compared with devices fabricated from strong piezoelectrics. The figure was taken from [42].

A few flexoelectric sensors have been recently proposed, which are able to convert mechanical deflections into significant induced charges [43, 44]. An efficient micro-curvature flexoelectricity-based sensor was proposed by [45]. A noteworthy design of a high-frequency bending resonator was presented by Bhaskar et al. [42]. The comparison with a piezoelectric bimorph actuator seems to tip in favor of the flexoelectric device. If the piezoelectric bimorph is limited by its operating temperature range and can bend only if clamped to

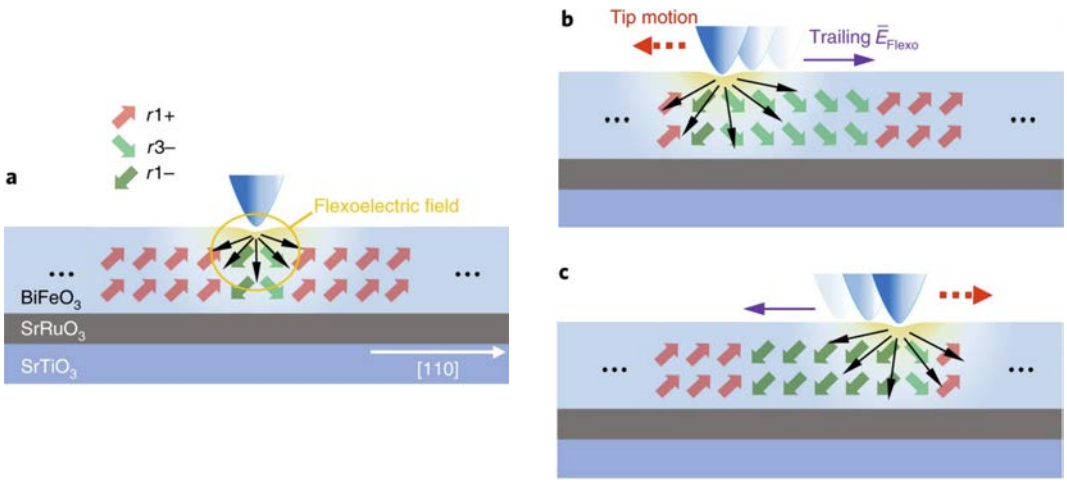

FIGURE 1.12: Polarization switches in ferroelectric thin films due to the mechanical gradients induced by (a) scanning probe in static contact, (b,c) tip motion along two opposite directions. Figure taken and adapted from [51].

a passive elastic layer, the flexoelectric setup appears to be easier to fabricate, compatible with the semiconductor silicon technology, and reasonably efficient if compared with some piezoelectricity-based devices.

It is also worth mentioning that flexoelectric energy harvesters are also gaining attention since their potentially high performance in small-scale devices. Currently, properly designed flexoelectric harvesters can reach up to 6% of conversion efficiency [46, 47]. Flexoelectricity-based devices in energy harvesting applications at small scales are more performant than the piezoelectric ones. Wang et al. [48] proposed an analytical approach to quantify the efficiency of a flexoelectric energy harvester. The predicted power output reached up to 12 times the classical piezoelectric model for thickness around 50nm.

Another application of flexoelectricity is related with ferroelectric materials and their spontaneous polarization which can be reversed by an external electric field. Different groups [49–51] proved that the spontaneous polarization in nano-scale ferroelectric thin films can also be switched by mechanical gradients induced by the tip of an atomic force microscope, Fig. 1.12. Polarization switching can be used in ultra-high storage density memory applications where bits are mechanically written and electrically read.

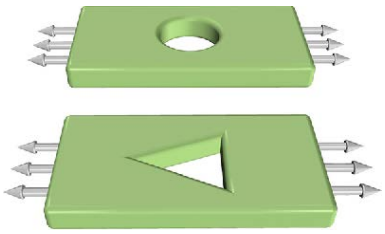

FIGURE 1.13: The figure shows two nonpiezoelectric 2D sheets with circular and triangular inclusions, respectively. When homogeneous stress is applied local strain gradients are produced within the vicinity of the holes on both sheets, thus producing a local non-zero polarization due to flexoelectricity. However, the overall polarization is non-zero only for the triangular inclusion where local responses do not annihilate themselves unlike it happens for the circular hole. A sheet with asymmetric inclusions exhibits effective piezoelectricity even though its material itself is not piezoelectric. The figure was taken from [52] and previously adapted from [53].

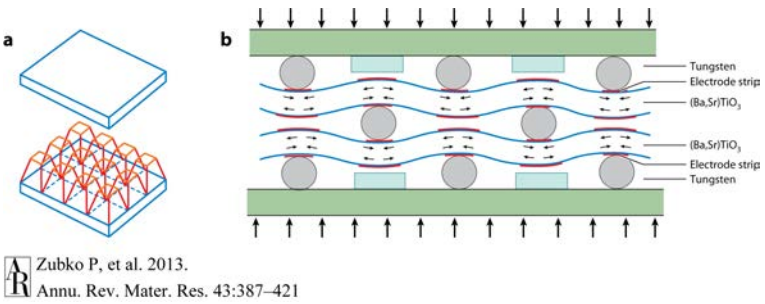

FIGURE 1.14: (a) Matrix of truncated pyramids with high flexoelectricity sandwiched beetween two rigid panels. An uniaxial load produces strain gradients in the constituents and results in a overall piezoelectric response [35]. (b) Piezoelectric composite based on flexure mode capable of mobilizing transverse stress and thus transverse flexoelectrity [58]. The figure has been taken from [27] and was previously adapted by [35] and [58].

We conclude by mentioning a particularly relevant application for this work, consisting in the ability of flexoelectric composites or metamaterials to endow any dielectric with effective piezoelectricity. Under an applied homogeneous deformation local gradients are generated at the microstructure level in the non-piezoelectric constituents, triggering the flexoelectric coupling. If proper designed, internal cancellations are avoided and the flexoelectric effect can be upscaled at the macro level as an apparent piezoelectric response [53]. A number of material architectures have been proposed including multimaterial stacks [54], geometrically polarized cavities in the material [53, 55] (Fig. 1.13), or the juxtaposition on a plane of polar elements such as micro-pyramids [35, 41, 56, 57] or flexural thin films [58], as shown in Fig. 1.14 taken from [27] and previously adapted by [35] and [58].

1.2.4 Coexistence and competition between flexoelectricity and piezoelectricity

In the last decades, most of the widely used materials for electromechanical transducers were piezoelectrics and remain so today despite the many achievements in this field. Progress in nano-technologies has progressively permitted to diminishing the size for these devices, now reaching thicknesses of few micrometers [4, 28, 29] where gradients are anything but insignificant, and still, flexoelectricity is yet commonly neglected. In a non-centrosymmetric crystal, both piezoelectricity and flexoelectricity compete in the generation of the total electric polarization

$$P_i = e_{ijk}\varepsilon_{jk} + \mu_{ijkl}\varepsilon_{jk,l}, \tag{1.6}$$

where e is the third-order piezoelectric tensor. Evidence has shown that the interplay between flexoelectricity and piezoelectricity at a small length scale is certainly not trivial. Due to their different fundamental symmetries, the two effects may both act in synergy or compete and thus undermine the electromechanical coupling. Abdollahi et al. [30] extensively studied these phenomena in bending piezoelectric transducers consisting of two bonded layers poled in opposite direction, where the polarization reversal can be controlled. Figure 1.15 shows these results, the pure piezoelectric response is compared with the combination of both electromechanical couplings. It appears that ignoring flexoelectricity at small scales may lead to significant errors in the expected device response. As they account for flexoelectricity the actuation response depends on the poling direction and thus, the coupling

effect may result strongly under or overestimated. At intermediate sizes where piezoelectricity and flexoelectricity are comparable (green dashed line in Fig. 1.15b), the interplay between them may, precisely, be constructive if they act in the same direction (Fig. 1.15b, insets a-c), or destructive otherwise (Fig. 1.15b, insets d-e) since the piezoelectric and flexoelectric moments act in opposite direction. As shown in Fig. 1.15 whereas piezoelectricity is independent of the sample size, as the sample size is further decreased the electromechanical coupling is dominated by the flexoelectric effect. Therefore, ignoring flexoelectricity at sub-micron scales can lead to dramatically degraded performance. On the other hand, the electromechanical transduction functionalities may be significantly enhanced by properly including flexoelectricity and hence designing flexoelectric-aware devices able to entirely exploit this effect.

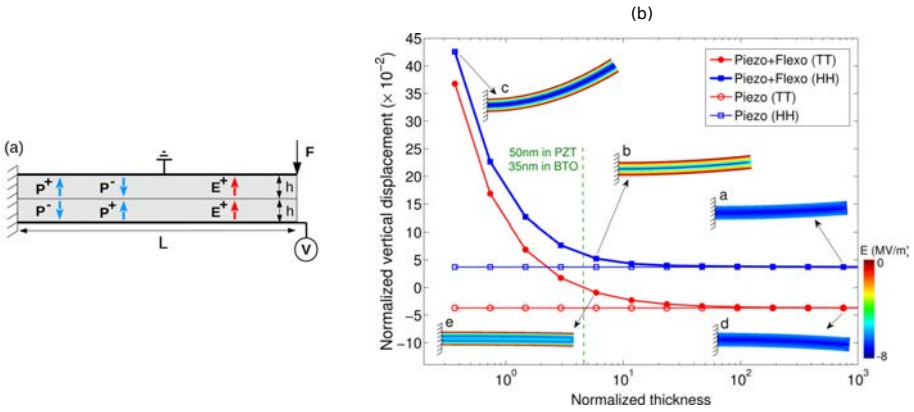

FIGURE 1.15: (a) Sketch of a series piezoelectric bimorphs configuration with piezoelectric layers poled in opposite direction, either Head-to-Head (HH) or Tail-to-Tail (TT) which corresponds in a polarization reversal (i.e. a change in sign). (b) Interplay between flexoelectricity and piezoelectricity for different piezoelectric bimorph cantilever beams. As flexoelectricity is accounted the actuation response is sensitive to the poling direction. Depending on the sign, it enhances (HH configuration) or destroys (TT configuration) the piezoelectric coupling. The figure has been adapted from Abdollahi [30]

.

1.3 Objectives of the thesis

The main goal of this thesis is to explore theoretically and computationally the engineering concepts for the rational design of piezoelectric metamaterials and devices exploiting the flexoelectric effect.

Two avenues are envisioned. On one hand, through the suitable geometry of a repeating unit, a metamaterial can exhibit a property not present in the base material. Here, the goal is to identify the engineering concepts that allow us to mobilize the flexoelectric response at the microscale, and upscale it to the macro-scale through material architecture, avoiding internal cancellation of the effect. Such a metamaterial behaves as a piezoelectric material at the macroscale, i.e. it responds electrically to applied homogeneous deformations, even when built from non-piezoelectric base materials. Conversely, it deforms under a uniform electric bias (Fig. 1.16). The present work relies on the premise that the material polarity required for an effective piezoelectric response, can be imprinted in the metamaterial through material architecture at the microscale, thus eliminating the need for a non-centrosymmetric atomic and molecular structure of the base-material. On the other hand, besides imprinting polarity

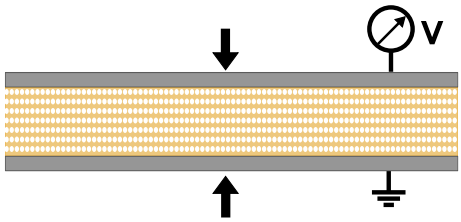

FIGURE 1.16: A properly designed flexoelectric metamaterial behaves as a piezoelectric material at the macroscale. An electrical output is generated when a homogeneous deformation is applied, or conversely it deforms under a uniform electrical bias.

geometrically in a lattice metamaterial, the overall symmetry of the system can be broken through multimaterial arrangements and boundary conditions.

Despite its unquestionable potential, the use of flexoelectricity in technology poses many challenges, theoretical, experimental and computational. The experimental characterization of flexoelectricity involves difficult experiments at sub-micron scales. Experimental setups have been proposed and used in some materials to quantify two of the three flexoelectric coefficients in cubic systems, longitudinal and transverse, while shear remains elusive. However, experimental observations of flexoelectricity are difficult to interpret and there is still a large discrepancy between experimental flexoelectric coefficient values and theoretical predictions [27]. This is partially related to the fact that flexoelectricity is a high-order theory involving field gradients, which restricts analytical solutions to very simple systems and requires advanced numerical techniques to solve boundary value problems in general geometries, and material and electrode configurations. The design of flexoelectric metamaterials and devices necessarily involves field-gradient engineering, for which engineering intuition is limited. Finally, flexoelectricity has been studied in bending and inhomogeneous compression, but other possible sources of field gradients have not yet been explored.

The specific objectives of this thesis are:

- using a hierarchical B-spline immersed method [59] to explore the flexoelectric response of beams under bending and establish the sensitivity of the solution to the model parameters, especially those which are not well characterize. This includes extensive testing and validation of the code.

- Explore the effective piezoelectric response of dielectric periodic lattices to establish the engineering concepts to achieve effective accumulation of the flexoelectric response from micro- to macroscopic scales.

- Propose, characterize, quantify and optimize piezoelectric metamaterials that effectively behave as piezoelectrics under uniform mechanical fields but are built from non-piezoelectric base materials.

- using a maximum entropy meshless method, explore and quantify the flexoelectric response of rods under torsion and establish the conditions under which it is possible, as well as their possible use as building-blocks in 3D piezoelectric metamaterials.

- explore, design and quantify flexoelectric composites and devices that achieve accumulation of the flexoelectric effect by multimaterial arrangements of through inhomogeneous macroscopic input.

1.4 Chapter overview

The manuscript is divided into two main parts, respectively regarding the identification of two-dimensional and three-dimensional suitable setups for constructively accumulating the flexoelectric effect in non-piezoelectric dielectrics. In Chapter 2 we summarize the theoretical and numerical tools that have been used to perform the work object of this thesis. In Chapter 3 we propose a new class of 2D flexoelectric-based metamaterials enabling piezoelectricity in non-piezoelectric dielectrics. Chapter 4 concerns a computational homogenization technique to perform a comprehensive study of the proposed architected materials, whereas in Chapter 5 we perform a shape optimization study of the aforementioned metamaterials. In Chapter 6, we propose guidelines for understanding the torsion problem in 3D flexoelectric rods and we present a novel approach for the quantification of the shear flexoelectric coefficient. Chapter 7 summarizes and concludes the manuscript.

1.5 List of publications

1.5.1 Publications derived from this thesis

- ***A.Mocci**, J.Barceló-Mercader, D.Codony and I.Arias. Geometrically polarized architected dielectrics with effective piezoelectricity.* (Submitted.) [60].

  We propose a class of metamaterials with piezoelectric-like behavior, which can be made out in principle of any dielectric material. To achieve significant piezoelectricity, we show that it is sufficient to suitably design the geometry of the material micro-architecture so that it contains thin elements subjected to bending and lacks mirror symmetry. We thus identify simple rules to turn a micro-architected metamaterial into a piezoelectric. The reader can find correspondence in Ch. 3, sec. 3.3.

- ***A.Mocci**, P.Gupta and I.Arias. Shape optimization of architected dielectrics with effective piezoelectricity using computational homogenization.* (In preparation.) [61].

  This paper develops a computational homogenization technique for flexoelectric-based architected dielectrics lacking piezoelectricity. We compute and characterize the overall behavior of micro-architected metamaterials proposed in [60]. We define the preferred operation mode and propose a systematic shape optimization for each of the aforementioned lattices. The work reported in this publication is addressed in Ch. 4 and Ch. 5 of this manuscript.

- ***A.Mocci**, A.Abdollahi and I.Arias. Flexoelectricity in dielectrics under torsion.* (Submitted.) [62].

  In this paper, we show that mechanical torsion of conical rods generically induces polarization domains and that these domains critically depend on flexoelectric anisotropy in materials with cubic symmetry. We further identify how the polarization domains depend on rod geometry and we establish conditions under which flexoelectricity manifests itself during torsion of thin rods, a canonical method to generate strain gradients. This work is reported in Ch. 6, sec. 6.2.

- ***A.Mocci**, A.Abdollahi and I.Arias. Flexoelectric bars under torsion: chasing the elusive shear flexoelectricity.* (To be submitted.) [63].

Flexoelectricity (the coupling between strain gradient and polarization and conversely strain and polarization gradients) is particularly strong in ferroelectrics. However, there is not yet a universal agreement on the magnitude and even sign of the flexoelectric coefficients in these materials. This situation is even more dramatic in the case of the shear flexoelectric coefficient since generating a measurable polarization induced by shear strain gradient is nontrivial. Based on torsion mechanics and using three-dimensional self-consistent simulations of flexoelectricity, we propose here a novel approach to quantify shear flexoelectricity in ferroelectrics. This approach also provides a validation benchmark for computational models of flexoelectricity. The reader is referred to Ch. 6, 6.3 for details about this work.

1.5.2 Other related publications

- *D.Codony, **A.Mocci**, O.Marco and I.Arias. Wheel-shaped and helical torsional flexoelectric devices.* (In preparation.) [64].

  With regards to the scalable flexoelectric device discussed in sec. 3.2, here we present torsional actuation able to induce bending in the internal component of a wheel-shaped device [13]. Extending this concept to three-dimensional scalable devices the flexoelectric effect is upscaled and a much larger net electric voltage is obtained.

- *J.Barceló-Mercader, **A.Mocci**, D.Codony and I.Arias. Generalized periodicity conditions for computational modeling of flexoelectric metamaterials.* (To be submitted.) [65].

  In this paper, we develop a method to enforce generalized periodic conditions. Thanks to this method the computational domain of an architected materials with periodic microstructure can be reduced to a single unit cell and thus the bulk response is efficiently evaluated without the need of considering a sufficiently large part of the whole domain.

1.6 Patents

- *I.Arias, A.Abdollahi, **A.Mocci** and D.Codony. Lattice structure with piezoelectric behavior, a force or movement sensor and an actuator containing said lattice structure.* European patent office. (2020).

  This patent, currently in PCT phase, contains the architected flexoelectric-based materials proposed in Ch. 3.

1.7 Conference proceedings

During the Ph.D., the work object of this thesis has been presented in several national and international conferences.

- ***A.Mocci**, A.Abdollahi and I.Arias. Quantification of shear flexoelectricity in ferroelectrics.* 16th European Mechanics of Materials Conference (EMMC16), Nantes, France (2018).

- ***A.Mocci**, A.Abdollahi and I.Arias. Quantification of shear flexoelectricity in ferroelectrics.* 10th European Solid Mechanics Conference (ESMC2018), Bologna, Italy (2018).

- ***A.Mocci**, D.Codony, A.Abdollahi and I.Arias. Flexoelectricity-based electromechanical metamaterials.* Symposium on Architectured material mechanics (IUTAM2018AMS), Chicago, IL(USA) (2018).
- ***A.Mocci**, A.Abdollahi and I.Arias. Flexoelectricity-based electromechanical metamaterials.* 55th Technical Meeting of the Society of Engineering Science (SES2018), Madrid, Spain (2018).

Chapter 2

Continuum model and two computational approaches for flexoelectricity

This chapter provides an overview of the two theoretical and computational frameworks that have been used to analyze and quantify the electromechanical response of flexoelectric metamaterials and devices. It is not intended to be exhaustive and the reader will be referred to the author's contributions.

The details about the derivations have been partially extracted from Abdollahi et al.[40] and Dr.David Codony's Ph. D dissertation [13] and recent publication [59].

2.1 Continuum model

Theoretical models of flexoelectricity are essential to fully understand and exploit this effect. The first phenomenological model was proposed by Kogan in 1964 [15] and later extended by Mindlin in 1968 [66]. However, we must leap almost twenty years before flexoelectricity was seen as a separated electromechanical effect in crystalline dielectrics, distinct from piezoelectricity. Only then, an exhaustive theoretical model was proposed [67, 68]. Nowadays, there are different phenomenological models that describe the flexoelectric phenomenon (the reader is referred to recent reviews on flexoelectricity for an exhaustive overview on the subject [27, 69, 70]).

To define a non-piezoelectric dielectric material within the continuum framework, one can write different models based on the choice of the state variables describing the flexoelectric effect. This results in different energy forms:

- Internal energy $\mathcal{U}(\varepsilon, \nabla\varepsilon, \mathbf{D}, \nabla\mathbf{D})$,
- Gibbs function $\Phi(\sigma, \nabla\sigma, \mathbf{E}, \nabla\mathbf{E})$,
- Electric enthalpy $\mathcal{H}(\varepsilon, \nabla\varepsilon, \mathbf{E}, \nabla\mathbf{E})$,
- Elastic Gibbs function $\mathcal{G}_1(\sigma, \nabla\sigma, \mathbf{D}, \nabla\mathbf{D})$,

where $\mathbf{D}$ and $\mathbf{E}$ represent the electric displacement and electric field, respectively.

Among all the energy forms, the electric enthalpy $\mathcal{H}$ is often considered more convenient since its dependence on the electric field instead of the electric displacement. The Maxwell-Faraday's law ($\nabla \times \mathbf{E} = 0$), indeed presumes that an electric potential ϕ exists such that

$$E = -\nabla\phi.$$

Thus, by selecting the electric potential ϕ as the electrical unknown the Maxwell-Faraday's law is automatically satisfied and does not require any extra constraint.

Several flexoelectric enthalpy forms can be written, mainly depending on the considered flexoelectric coupling. In the next sections and chapters we will refer to two different enthalpy forms, namely the *Direct* $\mathcal{H}^{\langle Dir\rangle}$ and the *Lifshitz-invariant* $\mathcal{H}^{\langle Lif\rangle}$ form, which have both been used for this work.

2.2 Variational models

Although different enthalpy forms lead to the same Euler-Lagrange equations, different boundary value problems must be derived since they give rise to different boundary condition definitions.

Considering the generic free enthalpy form $\mathcal{H}$, defined to mathematically describe the flexoelectric coupling, and $\mathcal{W}^{ext}$ the work done by the external sources, the variational formulation associated to the problem is written as [40]

$$\Pi[\mathbf{u}, \mathbf{E}] = \int_\Omega \mathcal{H}(\mathbf{u}, \mathbf{E}) d\Omega - \mathcal{W}^{ext}. \tag{2.1}$$

The following related variational principle corresponds to an unconstrained optimization problem

$$(\mathbf{u}^*, \phi^*) = \arg \min_{\mathbf{u}} \max_{\phi} \Pi[\mathbf{u}, -\nabla\phi]. \tag{2.2}$$

2.2.1 Direct flexoelectric form

The *Direct* enthalpy form $\mathcal{H}^{\langle Dir\rangle}$ is written as

$$\mathcal{H}^{\langle Dir\rangle}(\boldsymbol{\varepsilon}, \nabla\boldsymbol{\varepsilon}, \mathbf{E}) := \frac{1}{2}\varepsilon_{ij}\mathbf{C}_{ijkl}\varepsilon_{kl} + \frac{1}{2}\varepsilon_{ij,k}h_{ijklmn}\varepsilon_{lm,n} - \frac{1}{2}E_l\kappa_{lm}E_m - E_l\mu_{lijk}\varepsilon_{ij,k}, \tag{2.3}$$

where the mechanical displacement field $\mathbf{u}$ and the electric potential ϕ (s. t. , $E = -\nabla\phi$), are the unknown independent variables. The pure mechanical terms are represented by the forth-order elasticity tensor $\mathbf{C}$, with $\boldsymbol{\varepsilon} = 1/2(\nabla\mathbf{u} + \nabla\mathbf{u}^{\mathrm{T}})$ being the strain gradient tensor, $\mathbf{h}$ the sixth-order strain gradient elasticity tensor, whereas $\boldsymbol{\kappa}$ is the second-order dielectricity tensor. The electromechanical coupling is represented by the fourth-order direct flexoelectric tensor $\boldsymbol{\mu}$. From a dimensional argument, $\mathbf{h}$ and $\mathbf{C}$ induce and elastic length-scale ℓ_{mech}, while $\mathbf{C}, \boldsymbol{\kappa}, \boldsymbol{\mu}$ induce a flexoelectric length scale ℓ_{flexo} that controls the size-dependence of the effect. The reader can refer to the App. A and C for further details about the tensors [40] and their implementation.

Having defined the physical domain Ω, its boundary $\partial\Omega$ and its edges C, the admissible sources of external work are

$$\mathcal{W}^{\Omega}(\mathbf{u},\phi) := -\bar{b}_i u_i + \bar{q}\phi, \tag{2.4a}$$
$$\mathcal{W}^{\partial\Omega}(\mathbf{u},\phi) := -t_i u_i - r_i \partial^n u_i + \omega\phi \tag{2.4b}$$
$$\mathcal{W}^{C}(\mathbf{u},\phi) := -j_i u_i, \tag{2.4c}$$

where $\bar{\boldsymbol{b}}$ and $\bar{q}$ are body forces and free electric charges (i.e. forces per unit volume), $\mathbf{t}$ and $\mathbf{r}$ the tractions and double tractions (i.e. force and moment per unit area), ω the surface charge density (i.e. electric charge per unit area) and $\mathbf{j}$ the surface tension (i.e. force per unit length).

The boundary $\partial\Omega$ is split into $\partial\Omega = \partial\Omega_u \cup \partial\Omega_t = \partial\Omega_v \cup \partial\Omega_r = \partial\Omega_\phi \cup \partial\Omega_\omega$, being $\partial\Omega_u, \partial\Omega_v$ and $\partial\Omega_\phi$ the Dirichlet boundaries, where displacement field $\bar{\boldsymbol{u}}$, its normal derivative $\bar{v}$ and electric potential $\bar{\phi}$ are prescribed, and $\partial\Omega_t, \partial\Omega_r$ and $\partial\Omega_\omega$ the Neumann boundaries, where values for traction $\bar{\boldsymbol{t}}$, double traction $\bar{\boldsymbol{r}}$ and surface charge density $\bar{\omega}$ are applied. The edges C are also split into Dirichlet C_u and Neumann C_j edges, corresponding to prescribed displacement or surface tension $\bar{\boldsymbol{j}}$, respectively.

The corresponding boundary and edge conditions are written as:

$$\mathbf{u} - \bar{\boldsymbol{u}} = \mathbf{0} \quad \text{on} \quad \partial\Omega_u, \qquad \mathbf{t}(\mathbf{u},\phi) - \bar{\boldsymbol{t}} = \mathbf{0} \quad \text{on} \quad \partial\Omega_t, \tag{2.5a}$$
$$\partial^n(\mathbf{u}) - \bar{v} = \mathbf{0} \quad \text{on} \quad \partial\Omega_v, \qquad \mathbf{r}(\mathbf{u},\phi) - \bar{\boldsymbol{r}} = \mathbf{0} \quad \text{on} \quad \partial\Omega_r, \tag{2.5b}$$
$$\phi - \bar{\phi} = 0 \quad \text{on} \quad \partial\Omega_\phi, \qquad \omega(\mathbf{u},\phi) - \bar{\omega} = 0 \quad \text{on} \quad \partial\Omega_\omega, \tag{2.5c}$$
$$\mathbf{u} - \bar{\boldsymbol{u}} = \mathbf{0} \quad \text{on} \quad C_u, \qquad \mathbf{j}(\mathbf{u},\phi) - \bar{\boldsymbol{j}} = \mathbf{0} \quad \text{on} \quad C_j. \tag{2.5d}$$

It is worth highlighting that despite finite elements or meshless frameworks, where boundary conditions on $\partial\Omega_u$ are enforced strongly, automatically fulfilling the edge conditions, in a context where boundary conditions are weakly imposed, neglecting the edge condition on C_u would be analogous to erroneously considering homogeneous Neumann conditions on Dirichlet edges.

Following the standard approach in computational mechanics, Dirichlet boundary conditions are not included explicitly into the weak form since they are already fulfilled by a proper choice of the functional spaces. An alternative Nitsche's method for weak imposition of the boundary conditions was recently derived, we refer to Codony et al.[59] for the full derivation. The enthalpy functional in Eq. (2.1) is written as

$$\begin{aligned}\Pi_D^{\langle Dir\rangle}[\mathbf{u},\phi] = &\int_\Omega \Big(\mathcal{H}^{\langle Dir\rangle}(\boldsymbol{\varepsilon}(\mathbf{u}), \nabla\boldsymbol{\varepsilon}(\mathbf{u}), \mathbf{E}(\phi) - \bar{b}_i u_i + \bar{q}\phi\Big) d\Omega \\ &+ \int_{\partial\Omega_t} -\bar{t}_i u_i d\Gamma + \int_{\partial\Omega_r} -\bar{r}_i \partial^n u_i d\Gamma + \int_{\partial\Omega_\omega} \bar{\omega}\phi d\Gamma + \int_{C_j} -\bar{j}_i u_i ds.\end{aligned} \tag{2.6}$$

The equilibrium states $(\mathbf{u}^*, \phi^*)$ corresponds to the saddle point of the enthalpy potential, fulfilling the variational principle

$$(\mathbf{u}^*, \phi^*) = \arg \min_{\mathbf{u}\in\mathcal{V}_D} \max_{\phi\in\mathcal{P}_D} \Pi_D^{\langle Dir\rangle}[\mathbf{u},\phi], \tag{2.7}$$

with the functional space $\mathcal{V}_D$ and $\mathcal{P}_D$ having sufficient regularity and fulfilling the Dirichlet boundary conditions in Eq. (2.5), that is:

$$\mathcal{V}_D := \{\mathbf{u} \in [H^2(\Omega)]^3 \mid \mathbf{u} - \bar{\boldsymbol{u}} = \mathbf{0} \text{ on } \partial\Omega_u \text{ and on } C_u, \text{ and } \partial^n \mathbf{u} - \bar{\boldsymbol{v}} = \mathbf{0} \text{ on } \partial\Omega_v\}, \tag{2.8a}$$

$$\mathcal{P}_D := \{\phi \in H^1(\Omega) \mid \phi - \bar{\phi} = 0 \text{ on } \partial\Omega_\phi\}. \tag{2.8b}$$

The weak form of the problem is found by enforcing $\delta\Pi_D^{\langle Dir\rangle} = 0$ for all admissible variations $\delta\mathbf{u} \in \mathcal{V}_0$ and $\delta\phi \in \mathcal{P}_0$, with

$$\mathcal{V}_0 := \{\delta\mathbf{u} \in [H^2(\Omega)]^3 \mid \delta\mathbf{u} = \mathbf{0} \text{ on } \partial\Omega_u \text{ and on } C_u, \text{ and } \partial^n \delta\mathbf{u} = \mathbf{0} \text{ on } \partial\Omega_v\}, \tag{2.9a}$$

$$\mathcal{P}_0 := \{\delta\phi \in H^1(\Omega) \mid \delta\phi = 0 \text{ on } \partial\Omega_\phi\}. \tag{2.9b}$$

The weak form reads: *Find* $(\mathbf{u}, \phi) \in \mathcal{V}_D \otimes \mathcal{P}_D$ *such that,* $\forall(\delta\mathbf{u}, \delta\phi) \in \mathcal{V}_0 \otimes \mathcal{P}_0$,

$$\begin{aligned}\delta\Pi_D^{\langle Dir\rangle} &\equiv \delta_{\mathbf{u}}\Pi_D^{\langle Dir\rangle} + \delta_\phi\Pi_D^{\langle Dir\rangle} \\ &\equiv \int_\Omega (\hat{\sigma}_{ij}\delta\varepsilon_{ij} + \tilde{\sigma}_{ijk}\delta\varepsilon_{ij,k} - \hat{D}_l\delta E_l - \bar{b}_i\delta u_i + \bar{q}\delta\phi)d\Omega \\ &+ \int_{\partial\Omega_t} -\bar{t}_i\delta u_i d\Gamma + \int_{\partial\Omega_r} -\bar{r}_i\partial^n\delta u_i d\Gamma + \int_{\partial\Omega_\omega} \bar{\omega}\delta\phi d\Gamma + \int_{C_j} -\bar{j}_i\delta u_i ds = 0,\end{aligned} \tag{2.10}$$

having defined

$$\delta\boldsymbol{\varepsilon} := \boldsymbol{\varepsilon}(\delta\mathbf{u}), \quad \delta\nabla\boldsymbol{\varepsilon} := \nabla\boldsymbol{\varepsilon}(\delta\mathbf{u}), \quad \delta\mathbf{E} := \mathbf{E}(\delta\phi).$$

Integrating by parts and making use of the divergence and surface divergence theorems [59], the Euler-Lagrange equations are obtained

$$\begin{cases}(\hat{\sigma}_{ij} - \tilde{\sigma}_{ijk,k}), j + \bar{b}_i = 0 & \text{in } \Omega \\ \hat{D}_{l,l} - \bar{q} = 0 & \text{in } \Omega.\end{cases} \tag{2.11}$$

The Cauchy stress $\hat{\boldsymbol{\sigma}}$ and the hyper stress $\tilde{\boldsymbol{\sigma}}$ in Eqs. (2.10) and (2.11) represent the conjugate quantities to the strain $\boldsymbol{\varepsilon}$ and the strain gradient $\nabla\boldsymbol{\varepsilon}$, respectively, and can thus be derived from the electromechanical enthalpy as

$$\hat{\sigma}_{ij}(\boldsymbol{\varepsilon}, \nabla\boldsymbol{\varepsilon}, \mathbf{E}) := \frac{\partial\mathcal{H}^{\langle Dir\rangle}}{\partial\varepsilon_{ij}} = C_{ijkl}\varepsilon_{kl}, \tag{2.12a}$$

$$\tilde{\sigma}_{ijk}(\boldsymbol{\varepsilon}, \nabla\boldsymbol{\varepsilon}, \mathbf{E}) := \frac{\partial\mathcal{H}^{\langle Dir\rangle}}{\partial\varepsilon_{ij,k}} = h_{ijklmn}\varepsilon_{lm,n} - \mu_{lijk}E_l. \tag{2.12b}$$

Hence, the physical stress, from Eqs. (2.11), is defined as

$$\sigma_{ij}(\boldsymbol{\varepsilon}, \nabla\boldsymbol{\varepsilon}, \mathbf{E}) := \hat{\sigma}_{ij}(\boldsymbol{\varepsilon}, \nabla\boldsymbol{\varepsilon}, \mathbf{E}) - \tilde{\sigma}_{ijk}(\boldsymbol{\varepsilon}, \nabla\boldsymbol{\varepsilon}, \mathbf{E}) = C_{ijkl}\varepsilon_{kl} - h_{ijklmn}\varepsilon_{lm,n} + \mu_{lijk}E_l \tag{2.13}$$

Similarly, the conjugate quantity to the electric field $\mathbf{E}$ is the electric displacement $\hat{\mathbf{D}}$ in Eqs. (2.10) and (2.11), therefore

$$\hat{D}_l(\boldsymbol{\varepsilon}, \nabla\boldsymbol{\varepsilon}, \mathbf{E}) := \frac{\partial\mathcal{H}^{\langle Dir\rangle}}{\partial E_l} = -\kappa_{lm}E_m - \mu_{lijk}\varepsilon_{ij,k}. \tag{2.14}$$

The expressions for the traction $\boldsymbol{t}(\mathbf{u},\phi)$, the double traction $\boldsymbol{r}(\mathbf{u},\phi)$, the surface charge density $\boldsymbol{\omega}(\mathbf{u},\phi)$ and the surface tension $\boldsymbol{j}(\mathbf{u},\phi)$ in Eqs. (2.5) are derived as a result of the variational principle

$$t_i(\mathbf{u},\phi) = (\hat{\sigma}_{ij} - \tilde{\sigma}_{ijk,k} - \nabla^S_k \tilde{\sigma}_{ikj})n_j + \tilde{\sigma}_{ijk}\tilde{N}_{jk} \quad \text{on } \partial\Omega, \tag{2.15a}$$

$$r_i(\mathbf{u},\phi) = \tilde{\sigma}_{ijk} n_j n_k \quad \text{on } \partial\Omega, \tag{2.15b}$$

$$\omega(\mathbf{u},\phi) = -\hat{D}_l n_l \quad \text{on } \partial\Omega, \tag{2.15c}$$

$$j_i(\mathbf{u},\phi) = [\![\tilde{\sigma}_{ijk} m_j n_k]\!] \quad \text{on } C, \tag{2.15d}$$

where $\nabla^S\cdot$ is the surface divergence operator and $\tilde{N}$ is a measure of the curvature of the boundary, i.e. the second-order geometry operator.

2.2.2 Lifshitz-invariant flexoelectric form

The *Lifshitz-invariant* $\mathcal{H}^{\langle Lif\rangle}$ enthalpy form is defined as

$$\begin{aligned}\mathcal{H}^{\langle Lif\rangle}(\boldsymbol{\varepsilon}, \nabla\boldsymbol{\varepsilon}, \mathbf{E}, \nabla\mathbf{E}) :=& \frac{1}{2}\varepsilon_{ij}\mathbf{C}_{ijkl}\varepsilon_{kl} + \frac{1}{2}\varepsilon_{ij,k}h_{ijklmn}\varepsilon_{lm,n} - \frac{1}{2}E_l\kappa_{lm}E_m + \\ &- \frac{1}{2}E_{ij}b_{ijlk}E_{lk} - \frac{1}{2}\mu_{lijk}(\varepsilon_{ij,k}E_l - \varepsilon_{ij}E_{lk}).\end{aligned} \tag{2.16}$$

The extra high-order electric term $\mathbf{b}$ is the fourth-order electric gradient tensor. Analogously to the strain-gradient elasticity term, $\mathbf{b}$ and $\boldsymbol{\kappa}$ induce an electric length-scale ℓ_{elec}. Note that, in contrast to the direct form, the flexoelectric tensor $\boldsymbol{\mu}$ appears now both in the *direct* and *converse* flexoelectric effects.

Similarly to the direct flexoelectric form, the admissible external sources of work are

$$\mathcal{W}^{\Omega}(\mathbf{u},\phi) := -\bar{b}_i u_i + \bar{q}\phi, \tag{2.17a}$$

$$\mathcal{W}^{\partial\Omega}(\mathbf{u},\phi) := -t_i u_i - r_i \partial^n u_i + \omega\phi + \boldsymbol{\tau}\partial^n\phi \tag{2.17b}$$

$$\mathcal{W}^{C}(\mathbf{u},\phi) := -j_i u_i + \rho\phi, \tag{2.17c}$$

and the corresponding boundary conditions

$$\mathbf{u} - \bar{\boldsymbol{u}} = \mathbf{0} \quad \text{on} \quad \partial\Omega_u, \qquad \mathbf{t}(\mathbf{u},\phi) - \bar{t} = \mathbf{0} \quad \text{on} \quad \partial\Omega_t, \tag{2.18a}$$

$$\mathbf{u} - \bar{\boldsymbol{u}} = \mathbf{0} \quad \text{on} \quad C_u, \qquad \mathbf{j}(\mathbf{u},\phi) - \bar{\boldsymbol{j}} = \mathbf{0} \quad \text{on} \quad C_j \tag{2.18b}$$

$$\partial^n(\mathbf{u}) - \bar{v} = \mathbf{0} \quad \text{on} \quad \partial\Omega_v, \qquad \mathbf{r}(\mathbf{u},\phi) - \bar{\boldsymbol{r}} = \mathbf{0} \quad \text{on} \quad \partial\Omega_r, \tag{2.18c}$$

$$\phi - \bar{\phi} = 0 \quad \text{on} \quad \partial\Omega_\phi, \qquad \omega(\mathbf{u},\phi) - \bar{\omega} = 0 \quad \text{on} \quad \partial\Omega_\omega, \tag{2.18d}$$

$$\phi - \bar{\phi} = 0 \quad \text{on} \quad C_\phi, \qquad \rho(\mathbf{u},\phi) - \bar{\rho} = 0 \quad \text{on} \quad C_\rho, \tag{2.18e}$$

$$\partial^n(\phi) - \bar{\varphi} = \mathbf{0} \quad \text{on} \quad \partial\Omega_\varphi, \qquad \boldsymbol{\tau}(\mathbf{u},\phi) - \bar{\boldsymbol{\tau}} = \mathbf{0} \quad \text{on} \quad \partial\Omega_\tau, \tag{2.18f}$$

where $\bar{\varphi}$ is the prescribed normal derivative of the electric potential on the corresponding boundary $\partial\Omega_\varphi$, and $\bar{\boldsymbol{\tau}}$ is the double charge density prescribed on $\partial\Omega_\tau$. The edges C have also been split into C_ϕ and C_ρ where the charge density per unit length $\bar{\rho}$ is prescribed, in addition to the Dirichlet and Neumann partitions defined for the direct form of the enthalpy.

The enthalpy functional in Eq. (2.1) is written as

$$\Pi_D^{\langle Lif\rangle}[\mathbf{u},\phi] = \int_\Omega \Big(\mathcal{H}^{\langle Lif\rangle}(\boldsymbol{\varepsilon}(\mathbf{u}),\nabla\boldsymbol{\varepsilon}(\mathbf{u}),\mathbf{E}(\phi),\nabla\mathbf{E}(\phi)) - \bar{b}_i u_i + \bar{q}\phi\Big)d\Omega \tag{2.19}$$

$$+ \int_{\partial\Omega_t} -\bar{t}_i u_i d\Gamma + \int_{\partial\Omega_r} -\bar{r}_i \partial^n u_i d\Gamma + \int_{C_j} -\bar{j}_i u_i ds \tag{2.20}$$

$$+ \int_{\partial\Omega_\omega} \bar{\omega}\phi d\Gamma + \int_{\partial\Omega_\tau} \bar{\tau}\partial^n\phi d\Gamma + \int_{C_\rho} \bar{\rho}\phi ds. \tag{2.21}$$

The equilibrium states $(\mathbf{u}^*,\phi^*)$ corresponds to the saddle point of the enthalpy potential, fulfilling the variational principle

$$(\mathbf{u}^*,\phi^*) = \arg\min_{\mathbf{u}\in\mathcal{V}_D}\max_{\phi\in\mathcal{P}_D}\Pi_D^{\langle Lif\rangle}[\mathbf{u},\phi], \tag{2.22}$$

with the functional space $\mathcal{V}_D$ and $\mathcal{P}_D$ having sufficient regularity and fulfilling the Dirichlet boundary conditions in Eq. (2.18), that is:

$$\mathcal{V}_D := \{\mathbf{u}\in[H^2(\Omega)]^3 \mid \mathbf{u}-\bar{\boldsymbol{u}} = \mathbf{0} \text{ on } \partial\Omega_u \text{ and on } C_u, \text{ and } \partial^n\mathbf{u}-\bar{\boldsymbol{v}} = \mathbf{0} \text{ on } \partial\Omega_v\}, \tag{2.23a}$$

$$\mathcal{P}_D := \{\phi\in H^2(\Omega) \mid \phi-\bar{\phi} = 0 \text{ on } \partial\Omega_\phi \text{ and on } C_\phi, \text{and } \partial^n\phi-\bar{\varphi} = 0 \text{ on } \partial\Omega_\varphi\}. \tag{2.23b}$$

The weak form of the problem is found by enforcing $\delta\Pi_D^{\langle Lif\rangle} = 0$ for all admissible variations $\delta\mathbf{u}\in\mathcal{V}_0$ and $\delta\phi\in\mathcal{P}_0$, with

$$\mathcal{V}_0 := \{\delta\mathbf{u}\in[H^2(\Omega)]^3 \mid \delta\mathbf{u} = \mathbf{0} \text{ on } \partial\Omega_u \text{ and on } C_u, \text{ and } \partial^n\delta\mathbf{u} = \mathbf{0} \text{ on } \partial\Omega_v\}, \tag{2.24a}$$

$$\mathcal{P}_0 := \{\delta\phi\in H^2(\Omega) \mid \delta\phi = 0 \text{ on } \partial\Omega_\phi \text{ and on } C_\phi, \text{and } \partial^n\delta\phi = \mathbf{0} \text{ on } \partial\Omega_\varphi\}. \tag{2.24b}$$

The weak form reads: *Find* $(\mathbf{u},\phi)\in\mathcal{V}_D\otimes\mathcal{P}_D$ *such that,* $\forall(\delta\mathbf{u},\delta\phi)\in\mathcal{V}_0\otimes\mathcal{P}_0$,

$$\begin{aligned}\delta\Pi_D^{\langle Lif\rangle} &\equiv \delta_{\mathbf{u}}\Pi_D^{\langle Lif\rangle} + \delta_\phi\Pi_D^{\langle Lif\rangle}\\ &\equiv \int_\Omega\Big(\hat{\sigma}_{ij}\delta\varepsilon_{ij} + \tilde{\sigma}_{ijk}\delta\varepsilon_{ij,k} - \hat{D}_l\delta E_l - \tilde{D}_{lm}\delta E_{l,m} - \bar{b}_i\delta u_i + \bar{q}\delta\phi\Big)d\Omega\\ &+ \int_{\partial\Omega_t} -\bar{t}_i\delta u_i d\Gamma + \int_{\partial\Omega_r} -\bar{r}_i\partial^n\delta u_i d\Gamma + \int_{C_j} -\bar{j}_i\delta u_i ds\\ &+ \int_{\partial\Omega_\omega}\bar{\omega}\delta\phi d\Gamma + \int_{\partial\Omega_\tau}\bar{\tau}\partial^n\delta\phi d\Gamma + \int_{C_\rho}\bar{\rho}\delta\phi ds = 0,\end{aligned} \tag{2.25}$$

having defined

$$\delta\boldsymbol{\varepsilon} := \boldsymbol{\varepsilon}(\delta\mathbf{u}),\quad \delta\nabla\boldsymbol{\varepsilon} := \nabla\boldsymbol{\varepsilon}(\delta\mathbf{u}),\quad \delta\mathbf{E} := \mathbf{E}(\delta\phi),\quad \delta\nabla\mathbf{E} := \nabla\mathbf{E}(\delta\phi).$$

By integrating by parts and making use of the divergence and surface divergence theorems [59], the Euler-Lagrange equations are obtained

$$\begin{cases}(\hat{\sigma}_{ij} - \tilde{\sigma}_{ijk,k})_{,j} + \bar{b}_i = 0 & \text{in } \Omega,\\ (\hat{D}_{l,l} - \tilde{D}_{lk,k})_{,l} - \bar{q} = 0 & \text{in } \Omega.\end{cases} \tag{2.26}$$

The Cauchy stress $\hat{\boldsymbol{\sigma}}$ and the hyper stress $\tilde{\boldsymbol{\sigma}}$ in Eqs. (2.10) and (2.26) represent the conjugate quantities to the strain $\boldsymbol{\varepsilon}$ and the strain gradient $\nabla\boldsymbol{\varepsilon}$, respectively, and can thus be derived

from the electromechanical enthalpy as

$$\hat{\sigma}_{ij}(\boldsymbol{\varepsilon}, \nabla\boldsymbol{\varepsilon}, \mathbf{E}, \nabla\mathbf{E}) := \frac{\partial \mathcal{H}^{\langle Lif \rangle}}{\partial \varepsilon_{ij}} = C_{ijkl}\varepsilon_{kl} + \frac{1}{2}\mu_{lijk}E_{l,k} \tag{2.27a}$$

$$\tilde{\sigma}_{ijk}(\boldsymbol{\varepsilon}, \nabla\boldsymbol{\varepsilon}, \mathbf{E}, \nabla\mathbf{E}) := \frac{\partial \mathcal{H}^{\langle Lif \rangle}}{\partial \varepsilon_{ij,k}} = h_{ijklmn}\varepsilon_{lm,n} - \frac{1}{2}\mu_{lijk}E_l. \tag{2.27b}$$

Hence, the physical stress, from Eqs. (2.11), is defined as

$$\begin{aligned}\sigma_{ij}(\boldsymbol{\varepsilon}, \nabla\boldsymbol{\varepsilon}, \mathbf{E}, \nabla\mathbf{E}) :=& \hat{\sigma}_{ij}(\boldsymbol{\varepsilon}, \nabla\boldsymbol{\varepsilon}, \mathbf{E}, \nabla\mathbf{E}) - \tilde{\sigma}_{ijk}(\boldsymbol{\varepsilon}, \nabla\boldsymbol{\varepsilon}, \mathbf{E}, \nabla\mathbf{E}) \\ =& C_{ijkl}\varepsilon_{kl} - h_{ijklmn}\varepsilon_{lm,n} + \frac{1}{2}\mu_{lijk}(E_{l,k} - E_l)\end{aligned} \tag{2.28}$$

Similarly, the electric displacement $\hat{\mathbf{D}}$ and the double electric displacement $\tilde{\mathbf{D}}$ in Eqs. (2.10) are the conjugate quantity to the electric field $\mathbf{E}$ and the electric field gradient $\nabla\mathbf{E}$, respectively, and can be derived as

$$\hat{D}_l(\boldsymbol{\varepsilon}, \nabla\boldsymbol{\varepsilon}, \mathbf{E}, \nabla\mathbf{E}) := \frac{\partial \mathcal{H}^{\langle Lif \rangle}}{\partial E_l} = \kappa_{lm}E_m + \frac{1}{2}\mu_{lijk}\varepsilon_{ij,k} \tag{2.29a}$$

$$\tilde{D}_{lk}(\boldsymbol{\varepsilon}, \nabla\boldsymbol{\varepsilon}, \mathbf{E}, \nabla\mathbf{E}) := \frac{\partial \mathcal{H}^{\langle Lif \rangle}}{\partial E_{l,k}} = b_{ijlk}E_{i,j} - \frac{1}{2}\mu_{lijk}\varepsilon_{ij}. \tag{2.29b}$$

Therefore, it follows from Eq. (2.26) the definition of the physical electric displacement $\mathbf{D}$

$$\begin{aligned}D_l(\boldsymbol{\varepsilon}, \nabla\boldsymbol{\varepsilon}, \mathbf{E}, \nabla\mathbf{E}) :=& \hat{D}_l(\boldsymbol{\varepsilon}, \nabla\boldsymbol{\varepsilon}, \mathbf{E}, \nabla\mathbf{E}) - \tilde{D}_{lk}(\boldsymbol{\varepsilon}, \nabla\boldsymbol{\varepsilon}, \mathbf{E}, \nabla\mathbf{E}) \\ =& \kappa_{lm}E_m - b_{ijlk}E_{i,j} + \frac{1}{2}\mu_{lijk}(\varepsilon_{ij,k} - \varepsilon_{ij}).\end{aligned} \tag{2.30}$$

The expressions for the traction $\boldsymbol{t}(\mathbf{u}, \phi)$, the double traction $\boldsymbol{r}(\mathbf{u}, \phi)$, the surface charge density $\boldsymbol{\omega}(\mathbf{u}, \phi)$ the surface tension $\boldsymbol{j}(\mathbf{u}, \phi)$, the double charge density $\boldsymbol{\tau}(\mathbf{u}, \phi)$ and the charge density per unit length $\rho(\mathbf{u}, \phi)$ in Eqs. (2.5) are derived as a result of the variational principle

$$t_i(\mathbf{u}, \phi) = (\hat{\sigma}_{ij} - \tilde{\sigma}_{ijk,k} - \nabla^S_k\tilde{\sigma}_{ikj})n_j + \tilde{\sigma}_{ijk}\tilde{N}_{jk} \quad \text{on } \partial\Omega, \tag{2.31a}$$

$$r_i(\mathbf{u}, \phi) = \tilde{\sigma}_{ijk}n_jn_k \quad \text{on } \partial\Omega, \tag{2.31b}$$

$$\omega(\mathbf{u}, \phi) = -(\hat{D}_l - \tilde{D}_{lk,k} - \nabla^S_k\tilde{D}_{kl})n_l - \tilde{D}_{jk}\tilde{N}_{ij} \quad \text{on } \partial\Omega, \tag{2.31c}$$

$$\tau(\mathbf{u}, \phi) = -\tilde{D}_{jk}n_jn_k \quad \text{on } \partial\Omega, \tag{2.31d}$$

$$j_i(\mathbf{u}, \phi) = [\![\tilde{\sigma}_{ijk}m_jn_k]\!] \quad \text{on } C, \tag{2.31e}$$

$$\rho(\mathbf{u}, \phi) = -[\![\tilde{D}_{jk}m_jn_k]\!] \quad \text{on } C, \tag{2.31f}$$

where $\nabla^S\cdot$ is the surface divergence operator and $\tilde{N}$ is a measure of the curvature of the boundary, i.e. the second-order geometry operator.

2.3 Numerical methods

The flexoelectric formulation involves high-order partial differential equations (PDEs), which make the analytical approach nearly always challenging and feasible only for very simple models (e.g. cantilever beams under bending, truncated pyramid/cone under uniaxial compression [35, 71, 72]) and even then under heavily simplified assumptions. As a result, the

two-way flexoelectric coupling is often ignored and the strain gradient is commonly derived from elasticity alone [73]. The approximate solutions relying on restrictive assumptions are frequently not accurate and thus lead to under-or overestimate the electromechanical effect [34, 40, 74]. Moreover, significant strain gradients arise in complex geometries, for which analytical solutions may not be achieved.

In this context, self-consistent numerical simulations are essential for an accurate estimation of the two-way coupled problem in more complex setups, the reader can refer to Zhuang et al. [75] recent review for details on computational modeling for flexoelectricity. Numerically, the main difficulty is represented by the fourth-order nature of PDEs which describes the flexoelectric mechanism. Given the requirement of high-order continuity of the unknowns, at least C^1 continuous basis functions are needed, precluding the standard C^0 finite element methods. Several proposals can be found in the literature. Among those we cite mixed finite elements methods [76–78] or isogeometric analysis [79, 80]. The former, which was previously developed for strain gradient elasticity and later extended to flexoelectricity, introduces additional state variables to overcome the required continuity of the unknowns. The latter addresses the continuity requirement by using NURBS or B-splines functions. Based on the isogeometric paradigm, the basis functions defined for the approximation of the numerical solution are also used for the definition of the geometrical model. This discretization is particularly suitable in general industrial applications since the ability to exactly represent standard geometries (e.g. rectangular in 2D or cuboidal shapes in 3D). However, it becomes prohibitive for arbitrarily shaped domains.

In this work, two different recently-developed computational strategies have been used to solve flexoeletricity boundary value problems. In 2D, a B-spline-based immersed boundary approach has been used [59], while most 3D simulations have been obtained with a maximum entropy meshfree method [40]. In both cases, the basis functions provide the required continuity.

2.3.1 Immersed boundary hierarchical B-splines approach

The iHB-FEM (*Immersed boundary hierarchical B-splines framework for electromechanics*) approach, developed by Codony et al.[59] is the latest computational framework for flexoelectricity. The in-house code has been implemented in MatLab from scratch by Dr. David Codony in cooperation with Dr. Onofre Marco and Jordi Barceló Mercader and it belongs to Prof. Irene Arias. The author's manuscript has contributed to the implementation of some functionalities, in testing and documentation.

In the following, we will summarize the main features of the iHB-FEM approach, with particular focus on the functionality that tackles the issues debated in the section above.

Nitsche's method

As we will discuss in the following section, the immersed boundary method is based on a non-conforming (unfitted) Cartesian discretization of the domain. This feature makes it suitable for the discretization of arbitrary domain shapes with no geometrical limitations. However, when dealing with non-conforming discretization domain, the challenge is that essential boundary conditions must be enforced in weak form. To address this issue a Nitsche's method was proposed by Codony et al.[59].

Nitsche's method modifies the weak form and thus must be derived specifically for each formulation. The reader is referred to [59] and [13] for details about the derivation of the weak forms for the Nitsche's method.

The enthalpy functional in Eq. (2.6) is modified as

$$\Pi^{\langle Dir/Lif\rangle}[\mathbf{u},\phi] = \Pi_D^{\langle Dir/Lif\rangle}[\mathbf{u},\phi] + \Pi^{\langle Nitsche_{Dir}/Nitsche_{Lif}\rangle}[\mathbf{u},\phi], \tag{2.32}$$

with the $\Pi^{\langle Nitsche_{Dir}/Nitsche_{Lif}\rangle}$ acting on the Dirichlet boundaries. The variational principle associated to $\Pi^{\langle Dir/Lif\rangle}$ for the equilibrium states (u^*,ϕ^*) is

$$(\mathbf{u}^*,\phi^*) = \arg\min_{\mathbf{u}\in\mathcal{V}}\max_{\phi\in\mathcal{P}} \Pi^{\langle Dir/Lif\rangle}[\mathbf{u},\phi], \tag{2.33}$$

where $\mathcal{P} := H^1(\Omega)$, and $\mathcal{V}$ being the space of functions belonging to $[H^2(\Omega)]^3$ with L^2- integrable third derivatives on the boundary $\partial\Omega_u$, to account for the integrals involving $\boldsymbol{t}(\mathbf{u},\phi)$ in Eq. (2.15). The Euler-Lagrange equations resulting from making the enthalpy functional stationary as well as the definition of $\boldsymbol{t}(\mathbf{u},\phi)$,$\boldsymbol{r}(\mathbf{u},\phi)$, $\boldsymbol{\omega}(\mathbf{u},\phi)$ and $\boldsymbol{j}(\mathbf{u},\phi)$ are the same previously obtained in Eq. (2.11) and (2.15).

B-spline basis functions

As discussed in 2.3, the fourth-order nature of the PDE's which mathematically describe the flexoelectric problem requires high-order continuity of the unknowns, i.e. displacement field $\mathbf{u}$ and electric potential ϕ. C^1-continuity would already satisfy the request, however, Nitsche's weak form involves third-order derivatives in the boundary integrals, thus demanding at least C^2-continuity of the solution. B-spline functions are defined piecewise by polynomials of degree p, connected at fixed points defined as *knots* [81]. Polynomials of degree $p \geq 3$ provide high-order continuity C^{p-1} of the B-splines functions which makes them suitable for the purpose on hand, besides they can be efficiently evaluated and integrated with appropriate numerical quadrature.

Considering $\{\xi_i\} = [0,1,2,3,\ldots,n+p]$ as the uniform knot vector of a uniform B-spline basis of degree p and dimension n, the $i-$th basis function, is defined on the unidimensional parametric space $\xi \in [0, n+p]$ as:

$$\begin{aligned} B_i^0(\xi) &= \begin{cases} 1 & \xi_i \leq \xi < \xi_{i+1} \\ 0 & \text{otherwise} \end{cases}; \\ B_i^p(\xi) &= \frac{\xi-\xi_i}{\xi_{i+p}-\xi_i} B_i^{p-1}(\xi) + \frac{\xi_{i+p+1}-\xi}{\xi_{i+p+1}-\xi_{i+1}} B_{i+1}^{p-1}(\xi); \qquad i = 0,\ldots,n-1. \end{aligned} \tag{2.34}$$

It is worth to observe that the uniformity of the knot vector allows to define the i-th B-spline $B_i^p(\xi)$ function as a translation of the $B_i^0(\xi)$, i.e. $B_i^p(\xi) = B_0^p(\xi - i)$.

The $\boldsymbol{i}$-th B-spline function $B_{\boldsymbol{i}}^p(\boldsymbol{\xi})$ in a three dimensional space is defined as the tensor product of three B-spline functions as

$$\begin{aligned} B_{\boldsymbol{i}}^p(\boldsymbol{\xi}) = B_{[i_\xi,i_\eta,i_\tau]}^p([\xi,\eta,\tau]) &:= B_{i_\xi}^p(\xi) B_{i_\eta}^p(\eta) B_{i_\tau}^p(\tau); \\ \text{with} \quad i_\xi = 0,\ldots,n_\xi-1; \quad i_\eta &= 0,\ldots,n_\eta-1; \quad i_\tau = 0,\ldots,n_\tau-1, \end{aligned} \tag{2.35}$$

which is globally defined on the three-dimensional parametric space $\boldsymbol{\xi} \in \Theta := [0, n_\xi + p] \otimes [0, n_\eta + p] \otimes [0, n_\tau + p]$, in contrast with the elementwise defined standard FEM approximation.

As the flexoelectric unknowns $\mathbf{u}$ and ϕ are defined onto the physical space, a geometrical mapping $\boldsymbol{\varphi}(\boldsymbol{\xi})$ is required to map each physical coordinate $\mathbf{x} \in \Omega$ into a parametric one $\boldsymbol{\xi} \in \Theta$. The displacements $\mathbf{u}$ and electric potential ϕ can thus be approximated as

$$[\mathbf{u}(\boldsymbol{x})]_d \simeq \sum_i N_i(\boldsymbol{x}) a^u{}_{id} = \sum_i [N_i \circ \boldsymbol{\varphi}](\boldsymbol{\xi}) a^u{}_{id} = \sum_i B_i^p(\boldsymbol{\xi}) a^u{}_{id}, \qquad d = 1,2,3; \tag{2.36a}$$

$$\phi(\boldsymbol{x}) \simeq \sum_i N_i(\boldsymbol{x}) a^\phi{}_i = \sum_i [N_i \circ \boldsymbol{\varphi}](\boldsymbol{\xi}) a^\phi{}_i = \sum_i B_i^p(\boldsymbol{\xi}) a^\phi{}_i; \tag{2.36b}$$

where $\{\boldsymbol{a^u}, \boldsymbol{a^\phi}\}$ are the degrees of freedom of the numerical solution while $\boldsymbol{N} = [\boldsymbol{B}^p \circ \boldsymbol{\varphi}^{-1}]$ are the parametric basis functions mapped onto the physical space.

The map $\boldsymbol{\varphi}(\boldsymbol{\xi})$ is usually expressed as the interpolation of a discretization of the physical space, namely:

$$[\boldsymbol{\varphi}(\boldsymbol{\xi})]_d \simeq S_i(\boldsymbol{\xi}) \hat{x}_{id}, \qquad d = 1,2,3; \tag{2.37}$$

where $\boldsymbol{S}(\boldsymbol{\xi})$ are the basis functions used to interpolate the geometry, and $\hat{\boldsymbol{x}}$ are the so-called *control points* defining the map.

Due the C^{p-1}-continuity requirement for $\boldsymbol{N}(\boldsymbol{x})$, and as a consequence for $\boldsymbol{S}(\boldsymbol{\xi})$ as well, the most convenient option, but not the unique one, of $\boldsymbol{S}(\boldsymbol{\xi})$ is $\boldsymbol{S}(\boldsymbol{\xi}) := \boldsymbol{B}^p(\boldsymbol{\xi})$. It is worth noticing that upon this choice, the geometrical mapping $\boldsymbol{\varphi}(\boldsymbol{\xi})$, being globally defined, would require an underlying rigid Cartesian-like mesh to be mapped to the parametric space. This prevents a conforming discretization of the physical space thus, a different approach where the parametric space of the B-spline basis is mapped to a non-conforming discretization of Ω must be considered.

Immersed boundary method

The immersed boundary method, first proposed by [82, 83], allows for exact approximation of arbitrary domain shapes. Following this approach, we consider a larger non-conforming discretization domain $\Omega_E = \Omega \cup \Omega_{\text{fict}}$ which embeds the physical domain Ω. The physical domain Ω and its boundary $\partial\Omega$ intersect the cells of the embedding mesh arbitrarily since the discretization onto the physical space does not depend anymore on its geometrical configuration. The cells can thus be classified into three different sets depending on their intersection with the physical domain Ω. The set of *inner cells* $\mathcal{I}$, with no intersections with the boundary and all their vertices inside the domain; the set of *outer cells* $\mathcal{O}$, entirely outside the domain; the set of *cut cells* $\mathcal{C}$, intersected by the domain's boundary.

If on one side the immersed boundary approach tackles the issue due to arbitrarily defined shapes, on the other hand, two main challenges arise. On one side, since the definition of a nonconforming discretization domain, essential boundary conditions must be enforced in weak form using Nitsche's method, as previously discussed in sec. 2.3.1. On the other hand, we need to deal with arbitrarily cut cells which must be properly treated to ensure accurate integration and avoid ill-conditioning, produced by a small portion of the domain within the cut cell.

Regarding the numerical integration, bulk integrals are performed in the inner cells $\mathcal{I}$ and the physical part of the cut cells $\mathcal{C}$. Standard cubature rules [84] are used for the former, while the physical part of the cut cell is divided into conforming sub-domains that can be

easily integrated. The method used to sub-divide the physical part of each cut cell into several convenient sub-domains (e.g. triangles in 2D or tetrahedra in 3D) is the *marching cubes algorithm* [85, 86]. In general, an element-wise linear approximation is enough to capture the boundary of Ω. However, physical boundaries might be curved, and a non-exact approximation of the geometry might undermine the performance of the method. To circumvent this issue, we resort either to element-wise polynomial approximation of degree p or the NEFEM approach [87, 88] which ensures an exact approximation of the geometry [86].

Ill-conditioning arising from the cut cells has been overcome with the extended B-spline approach [89]. The critical basis functions are removed from the approximation space while the basis functions associated with neighboring inner cells are modified to extrapolate their behavior toward the cut cell.

The high-order B-Spline immersed boundary method is particularly attractive and suitable for nanoscale electromechanical devices with no geometrical limitations since its ability to capture the exact geometry. Material inclusions and interfaces can be easily handled. The computational domain of periodic microstructure can be reduced to a single unit cell, efficiently computed through generalized-periodic boundary conditions. Sensing electrode boundary conditions, required in some flexoelectric devices, can be applied.

2.3.2 Meshfree approximation scheme

Another suitable numerical approximation of partial differential equations is the meshfree method. In contrast to conventional mesh-based methods, the main advantage of the meshfree approximation schemes is the flexibility in the definition of the spatial discretization. Following these methods, we can define a set of basis functions $p^a(\mathbf{x})$ exhibiting C^∞ smoothness, built in a scattered distribution of nodes in the domain and with no fixed support. Here, we resort to *local maximum-entropy* (LME) approximation schemes, first proposed by Arroyo and Ortiz in 2005 [90, 91], and further detailed in [92]. The in-house code, written in C++, has been mainly developed by Dr. Christian Peco. The flexoelectric module was later implemented by Dr. Amir Abdollahi [40], providing the first self-consistent 3D approach to solve the flexoelectric problem.

With regards to the flexoelectric continuum model discussed in the previous section, the physical unknowns $\mathbf{u}$ and ϕ can thus be expanded as:

$$\mathbf{u}(\mathbf{x}) = \sum_{a=1}^{N} p^a(\mathbf{x})\mathbf{u}^a, \qquad \phi(\mathbf{x}) = \sum_{a=1}^{N} p^a(\mathbf{x})\phi^a. \tag{2.38}$$

Omitting the nodal values and the arguments of the basis functions, we can write

$$\partial_j u_i = \sum_{a=1}^{N} \partial_j p^a u_i^a, \qquad \partial_j\partial_k u_i = \sum_{a=1}^{N} \partial_j\partial_k p^a u_i^a, \qquad \partial_j\phi = \sum_{a=1}^{N} \partial_j p^a \phi^a, \tag{2.39}$$

involving the gradient and the Hessian of the basis function p^a. The algebraic function in terms of the nodal displacements $\mathbf{u}$ and electric potential ϕ, is obtained by entering the

discrete representation into the electromechanical enthalpy $\mathcal{H}_{dir}$ in Eq. (2.3).

$$\begin{aligned}\mathcal{H}(\mathbf{u},\phi) = &\frac{1}{2}\sum_{a,b}\mathbf{u}^{aT}\Big(\int_\Omega \mathbf{B}_\mathbf{u}(p^a)\mathbf{C}\mathbf{B}_\mathbf{u}^T(p^b)d\Omega\Big)\mathbf{u}^a + \sum_{a,b}\mathbf{u}^{aT}\Big(\int_\Omega \mathbf{B}_\mathbf{u}(p^a)\mathbf{e}\mathbf{B}_\phi^T(p^b)d\Omega\Big)\phi^b + \\ &+\sum_{a,b}\mathbf{u}^{aT}\Big(\int_\Omega \mathbf{H}_\mathbf{u}(p^a)\boldsymbol{\mu}^T\mathbf{B}_\phi^T(p^b)d\Omega\Big)\phi^b - \frac{1}{2}\sum_{a,b}\Big(\int_\Omega \mathbf{B}_\phi(p^a)\boldsymbol{\kappa}\mathbf{B}_\phi^T(p^b)d\Omega\Big)\phi^a\phi^b - \\ &-\sum_a\Big(\int_{\Gamma_t}\bar{\mathbf{t}}p^a dS\Big)\mathbf{u}^a + \sum_a\Big(\int_{\Gamma_D}\omega p^a dS\Big)\phi^a,\end{aligned} \tag{2.40}$$

where the material tensors, $\mathbf{C}$, $\boldsymbol{\kappa}$, $\mathbf{e}$ and $\boldsymbol{\mu}$, as well as the gradient $\mathbf{B}_\mathbf{u}$ and $\mathbf{B}_\phi$ and the Hessian $\mathbf{H}_\mathbf{u}$ operators, have all been written in Voigt notation. The reader is referred to App.C for details about the tensors implementation.

Although the strength of the meshfree approach, it is worth mentioning two main limitations of the method. Despite the capability of dealing with complex geometries, internal holes, interfaces, and multiple constituents can not be easily handled. An intermediate step to compute the basis functions is required, moreover, the non-polynomial nature of the basis functions generally requires rich integration quadrature, therefore dramatically increasing the computational cost.

Chapter 3

Flexoelectricity-based piezoelectric metamaterials and devices

3.1 Introduction

In 1968 Veselago theoretically proposed an engineered material with negative magnetic permeability and electric permittivity able to exhibit special macroscopic properties as negative refraction or backward wave propagation [93]. The name used to refer to this new class of material was *left-handed material* (LHM). Only later, in 1999, the definition of the term *metamaterial* was minted. Nowadays, a metamaterial can be defined as *"a macroscopic composite of periodic or non-periodic structure, whose function is due to both the cellular architecture and the chemical composition"*[94]. Therefore, metamaterials can be considered a class of material properly engineered to produce properties that do not occur naturally or to enhance intrinsic material properties. Mainly, due to progress in nano-technologies and experiments, in the last decades, many headways have been done in this promising field. Ranging from wave manipulation in electromagnetism [95–98], optics [99] and acoustic [100], to stiffness and lightness control in mechanics and structural applications [101–104], the spectrum of possibilities for new functionalities and extended material properties is in the thick of its outgrowth, especially for multiphysics coupling effects.

Many technologies involving sensing [2, 105], actuation [4] and energy harvesting [1, 3, 106, 107] rely on the ability of some materials to transduce electrical fields into mechanical deformation and vice-versa. This ability, as previously discussed, is generally physically supported by the piezoelectric effect [108]. The best-known piezoelectrics are ferroelectric ceramics, which are ubiquitous in current technologies despite their several downsides. The most efficient piezoelectrics, such as Lead-Zirconate-Titanate (PZT), consist of lead for around 60% of their entire composition. Substantial amounts of toxic substances are released during the manufacturing stage, moreover, the high percentage of hazardous substances renders the device not bio-compatible and certainly inapt for biomedical applications. In this regard, since 2003 the European Union has imposed restrictions and requested the replacement of hazardous substances from electric and electronic devices in favor of lead-free materials. The commitment of the scientific community in this field is synthesized in Fig. 3.1. Due to their own nature, piezoelectric materials also exhibit a very low elastic modulus (around 70GPa), which renders the materials extremely brittle with a toughness comparable with that of windows glass [6]. A further disadvantage is related to their restricted range of operating temperature limited by the Curie temperature (t_c), above which many of them become centrosymmetric, thus losing their piezoelectric properties altogether [6, 7, 9, 10, 109–111].

Thus, technologies based on electromechanical transduction ultimately depend on physics occurring at the scale of the atomic unit cell, where non-centrosymmetry and the resulting intrinsic polarity determine the piezoelectric effect [112, 113].

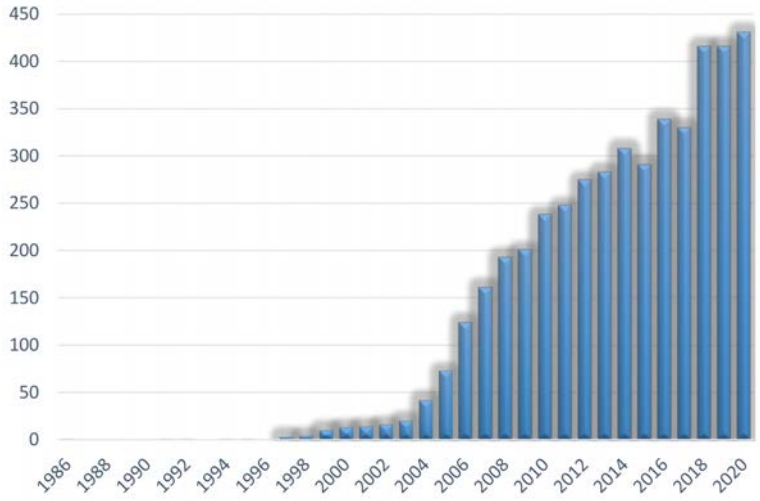

FIGURE 3.1: Since the request from the European union (https://eur-lex.europa.eu/legal-content/EN/TXT/?qid=1512061986553&uri=CELEX:32017L2102) to replace PZT with lead-free materials, the number of publications on *lead-free piezoceramics* has dramatically increased. The figure was elaborated by searching for "lead-free dielectric" in https://www.scopus.com/.

A piezoelectric devices is sketched in Fig. 3.2. A slab of active piezoelectric material is sandwiched between two metal electrodes, which can either collect the charge resulting from a mechanical stimulus or induce deformation due to an applied electric input [5, 114, 115].

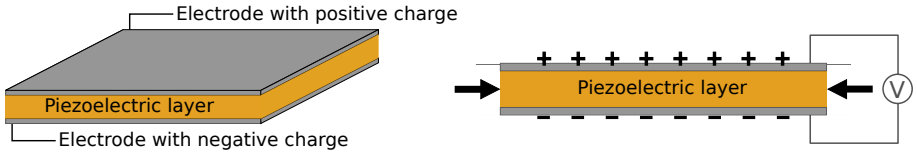

FIGURE 3.2: Piezoelectric sensor. A layer of piezoelectric material is sandwiched between two metal electrodes. An applied mechanical input generates a strain in the piezoelectric phase which is able to convert the mechanical energy into electrical.

Rather than having an electrical dipole hard-wired in the material at a molecular level, it is conceivable that, if we were able to induce a dipole into a nominally centrosymmetric material by other means, then electromechanical transduction could be achieved by a much broader class of materials.

In this regard, it has been suggested that the flexoelectric effect could enable a new class of effectively piezoelectric metamaterials made out of non-piezoelectric constituents [41, 53, 56–58, 116], as introduced in Section 1.2.3.

The analysis of these devices is much more complex than that of a conventional piezoelectric sandwich device and in fact the systematic examination of these ideas has been hindered by a lack of accurate theoretical and computational methods to predict the flexoelectric response in complex geometrical configurations.

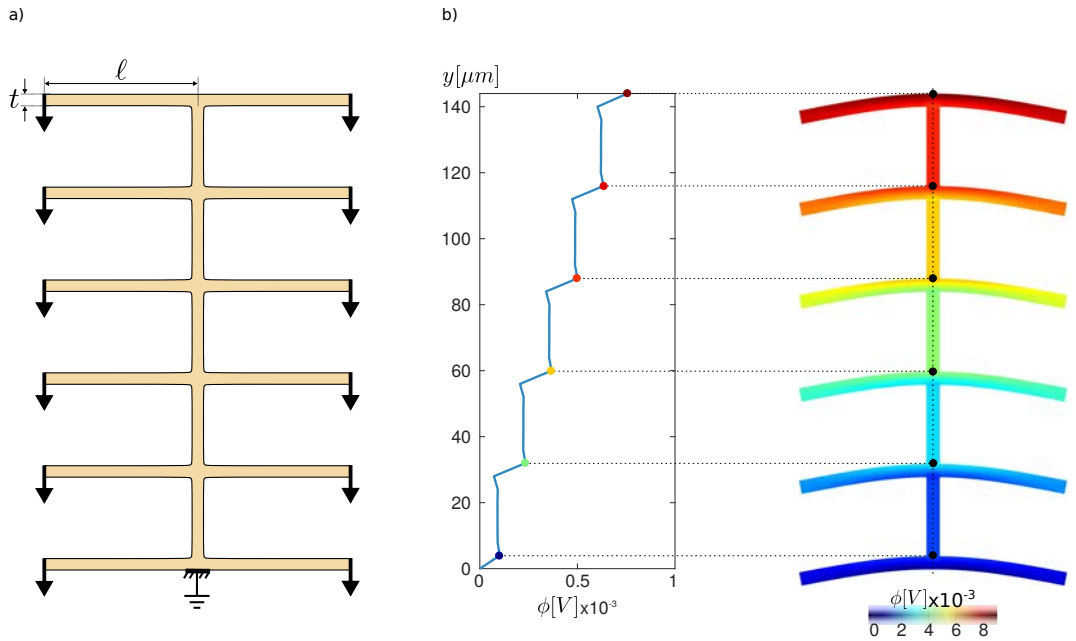

FIGURE 3.3: (a) Scalable effect in thin structural elements under bending.(b) Electric potential accumulation along the vertical direction.

3.2 Flexural scalable flexoelectric transducers

If the base material does not break centrosymmetry at an atomic scale, centrosymmetry could be broken through (1) boundary conditions or (2) multy-material arrangement.

Previous works have shown that, among all the possibilities, bending of thin structural elements is probably the most efficient way to mobilize flexoelectricity [34, 53]. It comes natural to think that if we were able to arrange a combination of flexural constituents able to act in synergy, the flexoelectric response would result amplified.

The probably most straightforward configuration for scaling a flexoelectric non-piezoelectric sample under bending is depicted in Fig. 3.3a. The key material parameters are reported in Table 3.1(Bulk). To computational evaluate the response of such a material we use the direct flexoelectric form of the enthalpy, previously introduced in sec. 2.2.1, within the immersed boundary framework where boundary conditions were imposed using Nitsche's method.

The geometry is composed of several beams $n_b = 6$ connected in parallel through a vertical beam. The beams are geometrically defined by their thickness $t = 40$nm and their length $\ell = 400$nm and the inter-space between them is $h = 280$nm . Each beam has been subjected to vertical mechanical loads F, while the whole structure has been clamped ($u_x = u_y = 0$) and electrically grounded ($\phi = 0$) at the bottom hand side of the vertical beam to avoid rigid body motions, as shown in Fig. 3.3a. The plot in Fig. 3.3b, shows the trend of the electric potential along the mid-point of the vertical beam. The electric potential distribution in Fig. 3.3b clearly shows the scalability of the response.

An even more efficient arrangement can be obtained by replicating several times the parallel beam-bending building block making use of serial connections. Figure 3.4a shows the geometrical model along with the enforced boundary conditions, through which the centrosymmetry of the system is broken and thus the flexoelectric effect mobilized. To create an efficient path and thus collect the electric potential through the serial connections, we introduced portions of insulator material ($\boldsymbol{\kappa} = \mathbf{0}$) between pairs of repeated structure. According

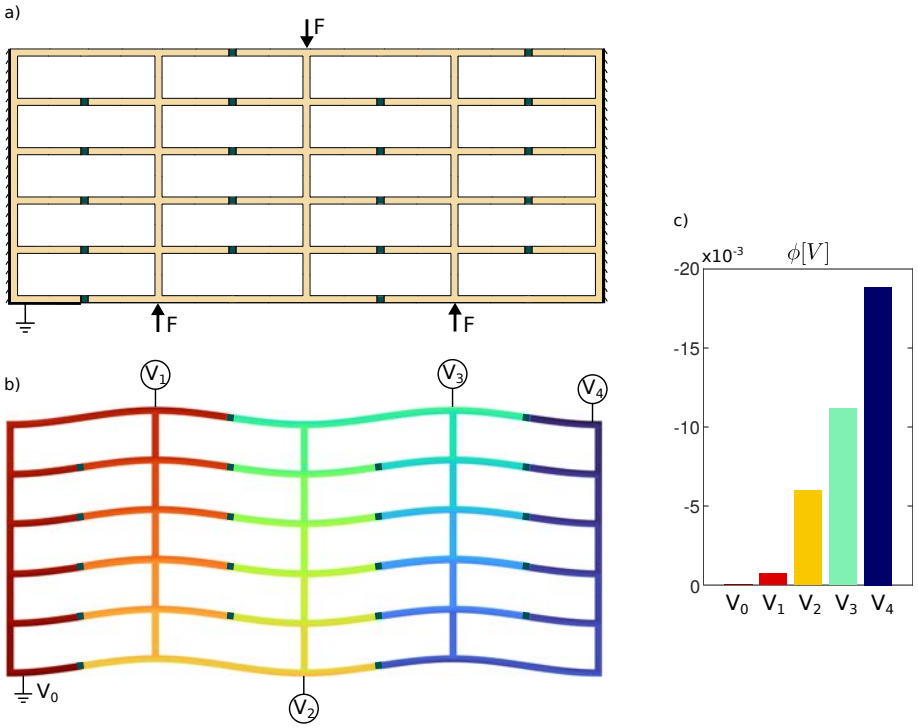

FIGURE 3.4: (a) Series connection of several parallel beam-bending building blocks and its boundary conditions. (b) The path for the electric potential distribution is induced by properly embedding insulator inclusions within the structure. (c) Scalability of the device.

to Barceló-Mercader et al. [117], we applied interface boundary conditions between adjacent faces. Figure 3.4b shows the electric potential accumulation evaluated at different points from the grounded (bottom-left) V_0 toward the placed electrode V_4. Figure3.4(b,c) shows the accumulated electric voltage and the scalability of the device.

TABLE 3.1: Material parameters

Material	E $[GPa]$	ν -	ℓ_{mech} $[n\text{m}]$	κ $[nC/V\text{m}]$	ℓ_{elec} $[n\text{m}]$	μ_ℓ $[\mu C/\text{m}]$	μ_t $[\mu C/\text{m}]$	μ_s $[\mu C/\text{m}]$
Bulk	152	0.33	1	141	0	150	110	110
Insulator	152	0.33	1	0	0	0	0	0

3.3 Geometrically polarized architected dielectrics with effective piezoelectricity

This section is adapted from [60][1].

The geometry of the material arrangement could also be responsible for breaking the centrosymmetry of the base material. The geometrical architecture of such materials should thus fulfill two requirements: (1) be geometrically polarized, and (2) amplify a uniformly applied macroscopic strain into large strain gradients in the microstructural elements.

[1] *A.Mocci, J.Barceló-Mercader, D.Codony and I.Arias. Geometrically polarized architected dielectrics with effective piezoelectricity.* (Submitted for publication.), 2021.

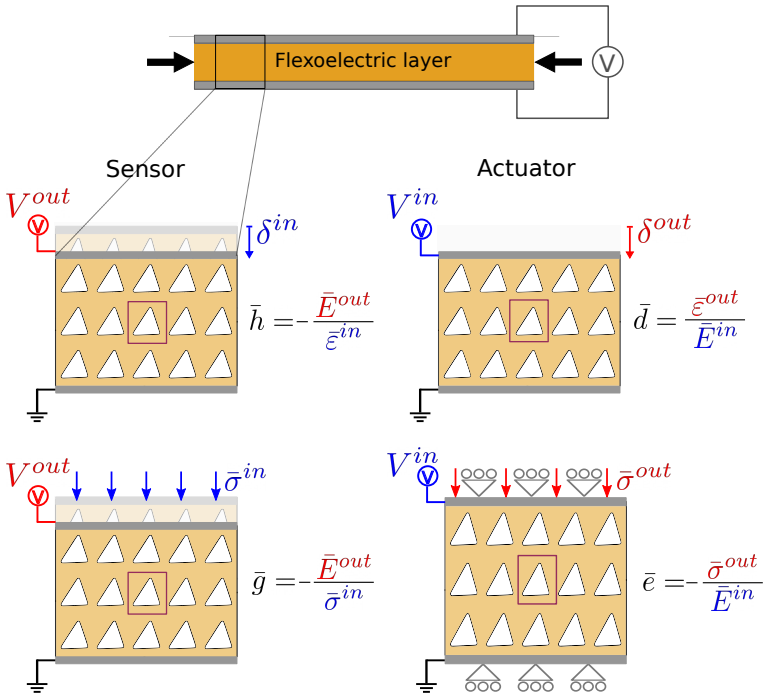

FIGURE 3.5: A layer of flexoelectric material is sandwiched between two electrodes. Schematic depiction of a periodic metamaterial in sensor or actuation mode. The effective electric field is defined as $\bar{E} = V/L_y$, the effective strain as $\bar{\varepsilon} = \delta/L_y$. The effective stress $\bar{\sigma} = F/L_x$ is work-conjugate to $\bar{\varepsilon}$, where F is the total vertical force on the device.

Following the canonical layout of a piezoelectric device, sketched in Fig. 3.2, we thus considered non-centrosymmetric geometrical arrangement of periodic architectures sandwiched between two electrodes, as sketched in Fig. 3.5, able to mimic piezoelectric electromechanical transducers.

3.3.1 Theoretical model and setup

As base material, we considered a non-piezoelectric dielectric, which nevertheless exhibited flexoelectricity. To mathematically model such material within the framework of continuum mechanics [34, 40, 74, 118], we make use of the symmetric Lifshitz-invariant form of the enthalpy, previously derived in sec. 2.2.2. To solve the Euler-Lagrange equations resulting from making the enthalpy functional stationary we adopted the recently developed immersed-boundary hierarchical B-Spline computational method [59], discussed in sec. 2.3.1.

To efficiently evaluate the performance of these materials, we considered a periodic unit cell and defined generalized periodic boundary conditions according to which the solution fields are periodic along the x direction and exhibit a constant jump along the y direction, which is either prescribed or solved for, Fig. 3.6. The internal free-surfaces of the device are assumed to be free of mechanical tractions and electric surface charges. If endowed with effective piezoelectricity, this device can function as a sensor if a macroscopic deformation $\bar{\varepsilon}^{\text{in}} = \delta^{\text{in}}/L_y$ (or alternatively a macroscopic stress $\bar{\sigma}^{\text{in}}$) is applied and a macroscopic electric field $\bar{E}^{\text{out}} = -V^{\text{out}}/L_y$ is recorded. Alternatively, it can function in actuator mode if $\bar{E}^{\text{in}}$ is applied and $\bar{\varepsilon}^{\text{out}}$ (or alternatively $\bar{\sigma}^{\text{out}}$) is recorded.

Following classical piezoelectricity [5], we derived four *effective* piezoelectric coupling coefficients (see App. B) of our metamaterials depending on the electromechanical ensemble,

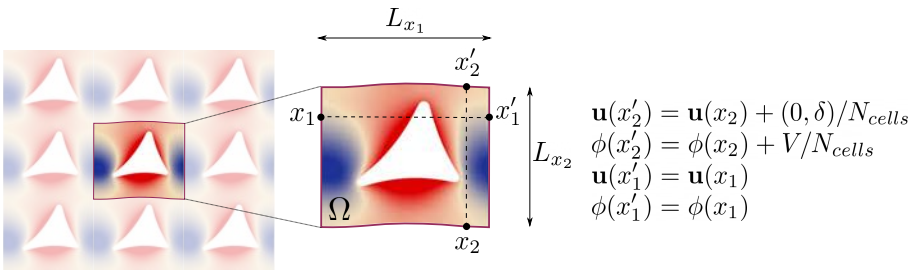

FIGURE 3.6: Illustration of the generalized-periodic boundary conditions on a unit cell of the periodic metamaterial.

Fig. 3.5

$$\bar{h} = -\left.\frac{\partial \bar{E}}{\partial \bar{\varepsilon}}\right|_{\bar{D}=0}; \quad \bar{g} = -\left.\frac{\partial \bar{E}}{\partial \bar{\sigma}}\right|_{\bar{D}=0}; \quad \bar{d} = \left.\frac{\partial \bar{\varepsilon}}{\partial \bar{E}}\right|_{\bar{\sigma}=0}; \quad \bar{e} = -\left.\frac{\partial \bar{\sigma}}{\partial \bar{E}}\right|_{\bar{\varepsilon}=0}, \tag{3.1}$$

where all the quantities involved have already been defined in Ch. 2. Although the third of these coefficients $\bar{d}$ is the most common figure of merit for piezoelectricity, each of them is pertinent to a distinct sensing or actuation scenario.

As base material, we considered a ferroelectric perovskite at its paraelectric (non-piezoelectric) phase, namely nanocrystalline Barium Strontium Titanate (BST), with composition $Ba_{0.60}Sr_{0.40}Ti_3$, which exhibits high dielectric constant and thus strong flexoelectricity [27]. Isotropic material properties (elastic, dielectric, and flexoelectric) were assumed since additive manufacturing techniques for nanoarchitected lattices produce amorphous or nanocrystalline microstructures [119].

Following [27, 67, 68, 70], the magnitude of the flexoelectric coefficients were chosen as $\mu = \chi_e \varepsilon_0 f$, being f the flexocoupling coefficient, ε_0 the vacuum permittivity and $\chi_e = 1000$ the dielectric susceptibility of BST at room temperature [120]. Here, we took $f = 125$ V. The resulting flexoelectric coefficients are comparable to theoretical values reported in [121] and smaller than that measured in [122]. The length-scale parameters ℓ_{mech} and ℓ_{elec} are required for stability of the formulation [59, 118]. The parameter ℓ_{mech}, which controls the breakdown of local elasticity at small scales and depends on the microstructure of the material, was chosen in the order given by [123]. On the other side, ℓ_{elec} parameter is not well characterized to our knowledge and thus was chosen such that our simulations remained stable and devoid of oscillations. All material parameters are reported in table 3.2.

TABLE 3.2: Material parameters

Material	E $[GPa]$	ν -	ℓ_{mech} $[nm]$	κ $[nC/V\text{m}]$	ℓ_{elec} $[nm]$	μ_ℓ $[\mu C/\text{m}]$	μ_t $[\mu C/\text{m}]$	μ_s $[\mu C/\text{m}]$
BST	152	0.33	50	8	300	1.21	1.10	0.055

As a proof of concept of our theoretical approach, we first considered an architected material lacking geometric polarization in sensor and actuator modes, Fig. 3.7a-b (centrosymmetric). We found that although the flexoelectrically-induced electric and strain fields exhibited significant local variations within the unit cell, there was no net accumulation of electric potential/displacement in sensor/actuator mode. We then considered a geometrically polarized architected material, suggested by [53], consisting of triangular voids. We confirmed that this design leads to a net accumulation of electric potential and displacement, Fig. 3.7a-b (geometrically-polarized), thereby exhibiting effective piezoelectricity despite the

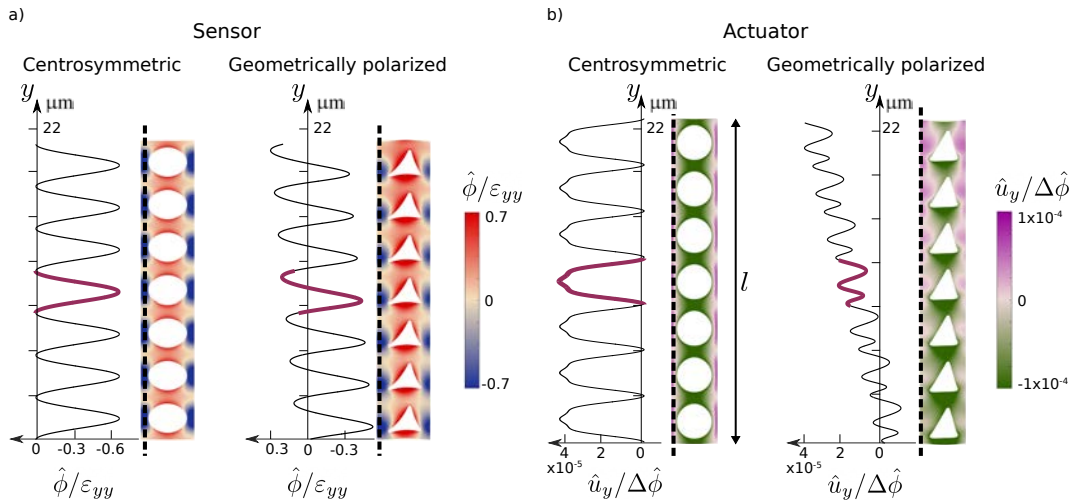

FIGURE 3.7: (a) Electric potential in two devices (left: centrosymmetric; right: non-centrosymmetric) under an applied deformation (sensor mode). The curves show the electric potential along the dashed line. In both cases, the flexoelectric effect generates internal electric fields. However, a net electric field $\bar{E}$ is only present in the non-centrosymmetric device. The thin line represents a calculation of the entire device whereas the thick line shows the calculation of a single unit cell with generalized periodic boundary conditions. The electric field has been normalized as $\hat{\phi} = \phi\kappa/\mu$. (b) Displacements in the same two devices under applied voltage (actuator mode), where again net strain $\bar{\varepsilon}$ is only achieved for the non-centrosymmetric device. The displacement field has been normalized as $\hat{u}_y = u_y/l$.

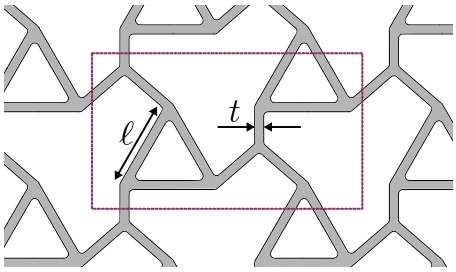

FIGURE 3.8: Geometrical parameters of the unit cell.

non-piezoelectric nature of the base material. Importantly, since flexoelectricity is a two-way electromechanical coupling [124], the metamaterial exhibited both direct and inverse piezoelectricity. Besides validating the fundamental premise of this study, these calculations also allowed us to validate the generalized-periodic boundary conditions by simulating a repetition of stacked unit cells and comparing with a single unit-cell calculation, Fig. 3.7a-b.

3.3.2 Bending-dominated non-centrosymmetric lattices

Following the work presented in sec. 3.2, we claim that bending of thin structural elements is an efficient way to mobilize flexoelectricity [34, 53]. We thus decided to examine bending-dominated low-volume-fraction lattice architectures. As expected, centrosymmetric (geometrically non-polarized) lattices such as the 2D-chiral lattice shown in Figs. 3.9a developed internal field variations but did not exhibit effective piezoelectricity, quantified in Fig. 3.9b.

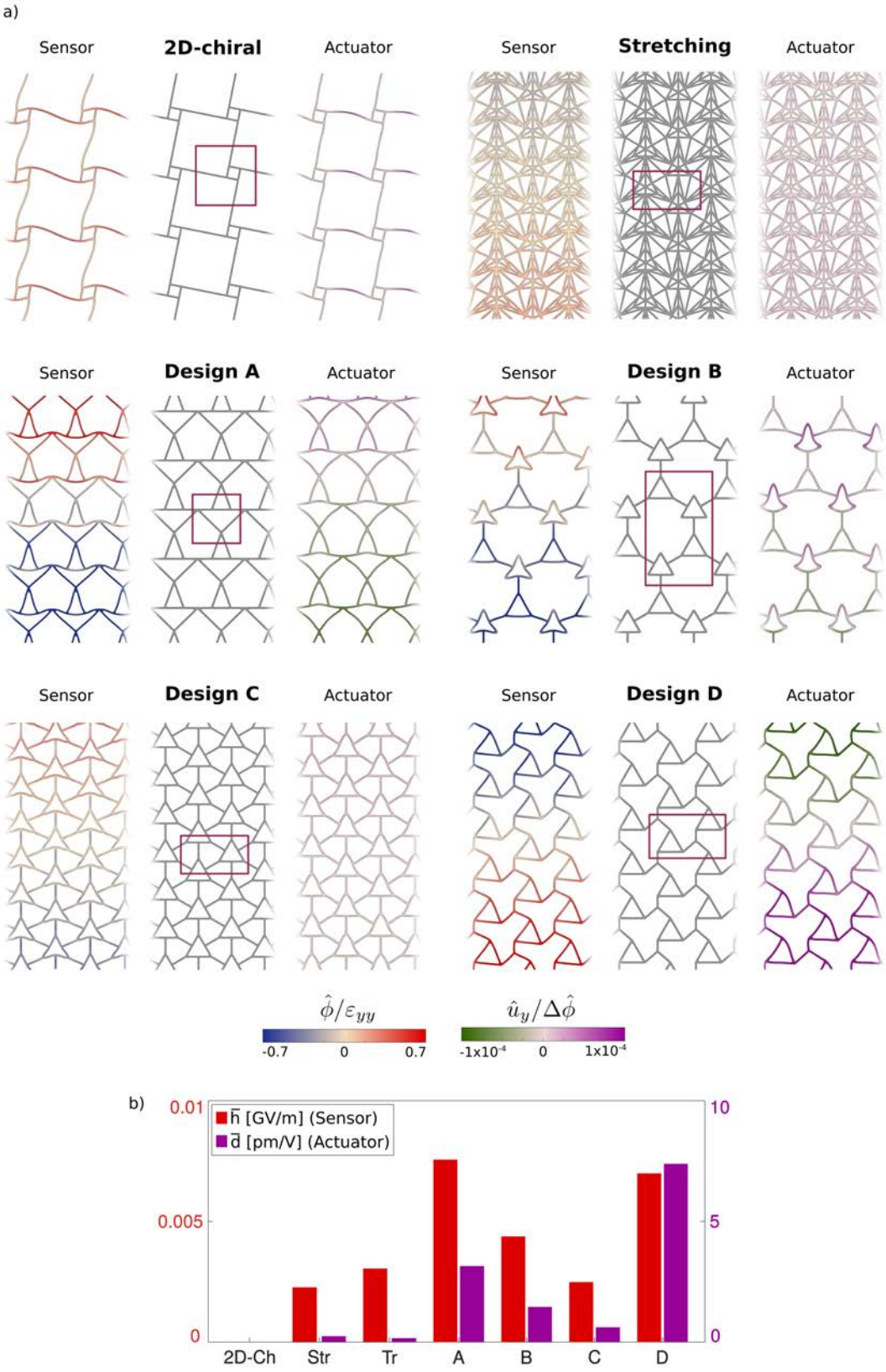

FIGURE 3.9: (a) Electric field and $y-$displacement plotted on the deformed configuration for various material designs in sensor and actuator mode. Electric and displacement fields have been normalized as in Fig. 3.7, displacements have been exaggerated and several copies of the unit cell have been represented for clarity. (b)Summary of effective piezoelectric coefficients for each design in sensor and actuator mode.

In contrast, we considered a number of geometrically polarized lattices, five of which are reported in Fig. 3.9a, all of which systematically exhibited effective direct and converse piezoelectricity. In all non-centrosymmetric designs, the typical beam length ℓ was comparable and the thickness t was the same, Fig. 3.8.

In structural applications requiring low-weight high-stiffness structures, stretching-dominated lattices are generally preferred [101, 102]. In the present context, however, we found that such structures did not efficiently exploit the flexoelectricity of the microstructural elements and lead to lower effective piezoelectric responses, see the design labeled as "Stretching" in Fig. 3.9a. To seek bending-dominated geometrically polarized lattices, we considered low-connectivity designs following [125], which resulted in effective piezoelectric coefficients of different magnitude. Interestingly, the most performant designs in sensor mode (A and D) exhibited nearly monotonic variations of the electric field, whereas those exhibiting large internal fluctuations of electric field (Stretching, B and C) did not perform that well. Likewise, design D was the best in actuator mode and exhibited a nearly monotonic displacement distribution.

Since field gradients scale inversely with size, the flexoelectric coupling, and hence the effective piezoelectric properties of our metamaterials should also be inversely proportional to size [40]. From a practical point of view, however, increasing performance by scaling downsize is bound by fabrication. In our calculations, the minimum thickness that we considered was 40nm, which may be attained using for instance Atomic Layer Deposition techniques [119] or well above those currently achievable with additive manufacturing [126].

3.3.3 Anisotropy and area fraction

To study more systematically the dependence of piezoelectric performance on lattice geometry, we reasoned that the response should be highly anisotropic. Take for instance design B in Fig. 3.9a. By its symmetry, it is not geometrically polarized along the horizontal direction, and hence it should not exhibit effective piezoelectricity when loaded horizontally. To quantify this effect, we considered the standard sandwich device and rotated the lattice microstructure relative to the device axis for designs A to D. We implemented this by appropriate rotation of the generalized periodic boundary conditions [65] (details will be discussed in later section 3.3.5). We represented the effective piezoelectric coefficients $\bar{h}$ and $\bar{d}$, suitably normalized, in polar plots where continuous/dashed lines refer to positive/negative values, Fig. 3.10. As anticipated, we found an extreme anisotropy of effective piezoelectric coefficients, moreover, since we consider isotropic material properties, the resulting anisotropy is attributable to the geometrical design.

In all cases, these coefficients reversed sign under 180° rotations, consistent with the odd-rank nature of the piezoelectric tensor. Furthermore, we found that the symmetry of the effective piezoelectric response agreed with that of the underlying geometry, with Design A exhibiting one planar mirror symmetry (pm), Designs B and C exhibiting symmetry with respect to 120° rotations and one planar mirror symmetry (p31m) [127], and Design D exhibiting no additional symmetries.

Besides changing the orientation of the lattice, we examined the effect of area fraction by fixing $\ell = 1.6\mu$m and varying t between 40 and 400nm. This effect is not obvious a priori since lower area fractions lead to more slender and bendable sub-units, which can efficiently mobilize flexoelectricity, but higher area fraction mobilizes more material that supports the flexoelectric effect. We represented the effective piezoelectric coefficients corresponding to

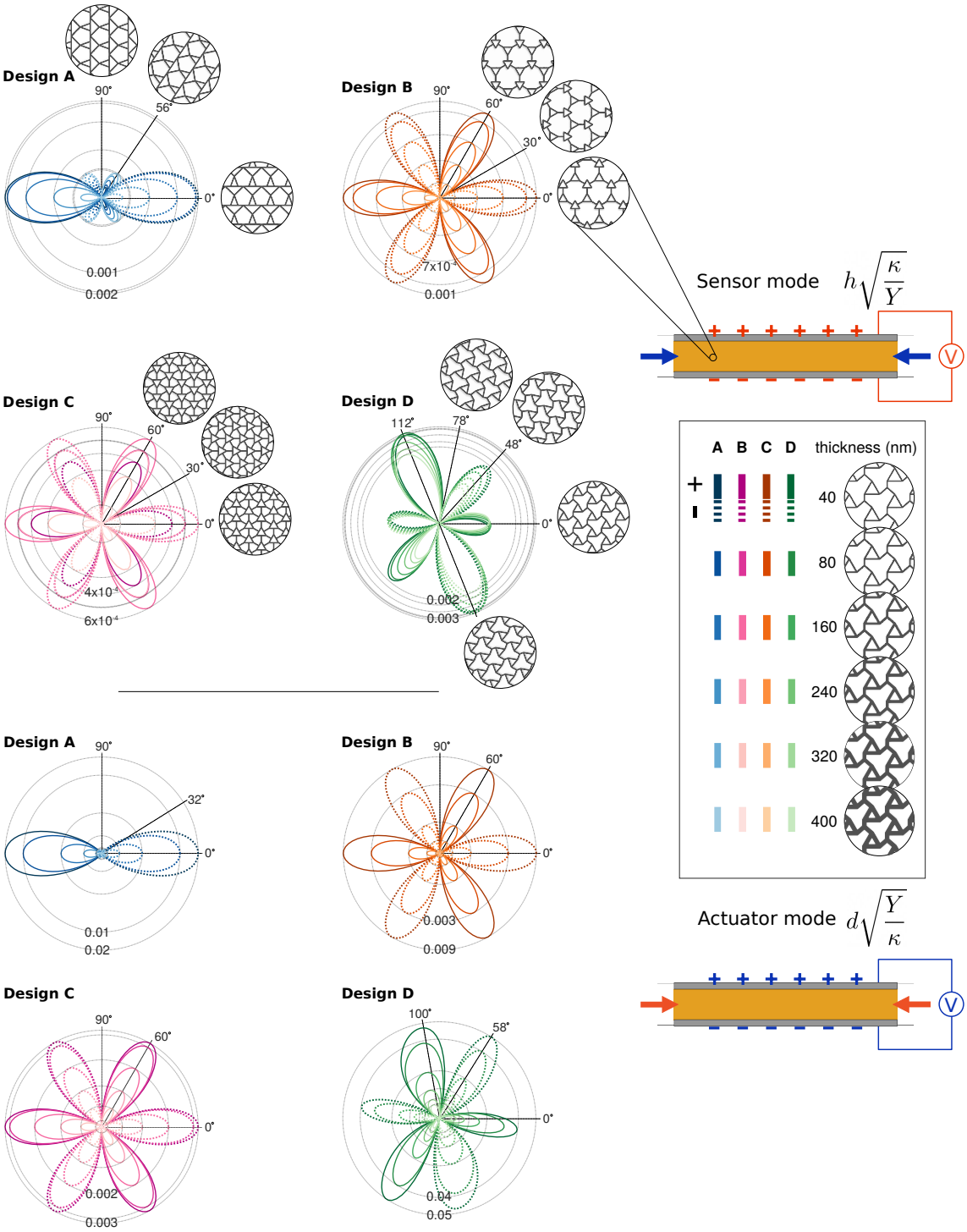

FIGURE 3.10: (a) Anisotropy of the effective piezoelectric coefficient $\bar{h}$ normalized as $\bar{h}\sqrt{\kappa/Y}$ in sensor mode for Designs A to D. In the polar plots, continuous lines denote positive values of $\bar{h}$ whereas dashed lines indicate negative values. Color intensity indicates the thickness of structural elements for a fixed $\ell = 1.6\mu$m, as shown in the legend. (b) Analogous results for coefficient $\bar{d}$ normalized as $\bar{d}\sqrt{Y/\kappa}$ in actuator mode.

different thicknesses by changing the color intensity, Fig. 3.10. As anticipated, the results were highly nontrivial. Whereas for designs B reducing area fraction essentially lead to increasing effective piezoelectricity in all directions, for design A and D it lead to increasing or decreasing piezoelectricity depending on orientation. For design C, the dependence on

area fraction is non-monotonic.

3.3.4 Effective piezoelectric performance

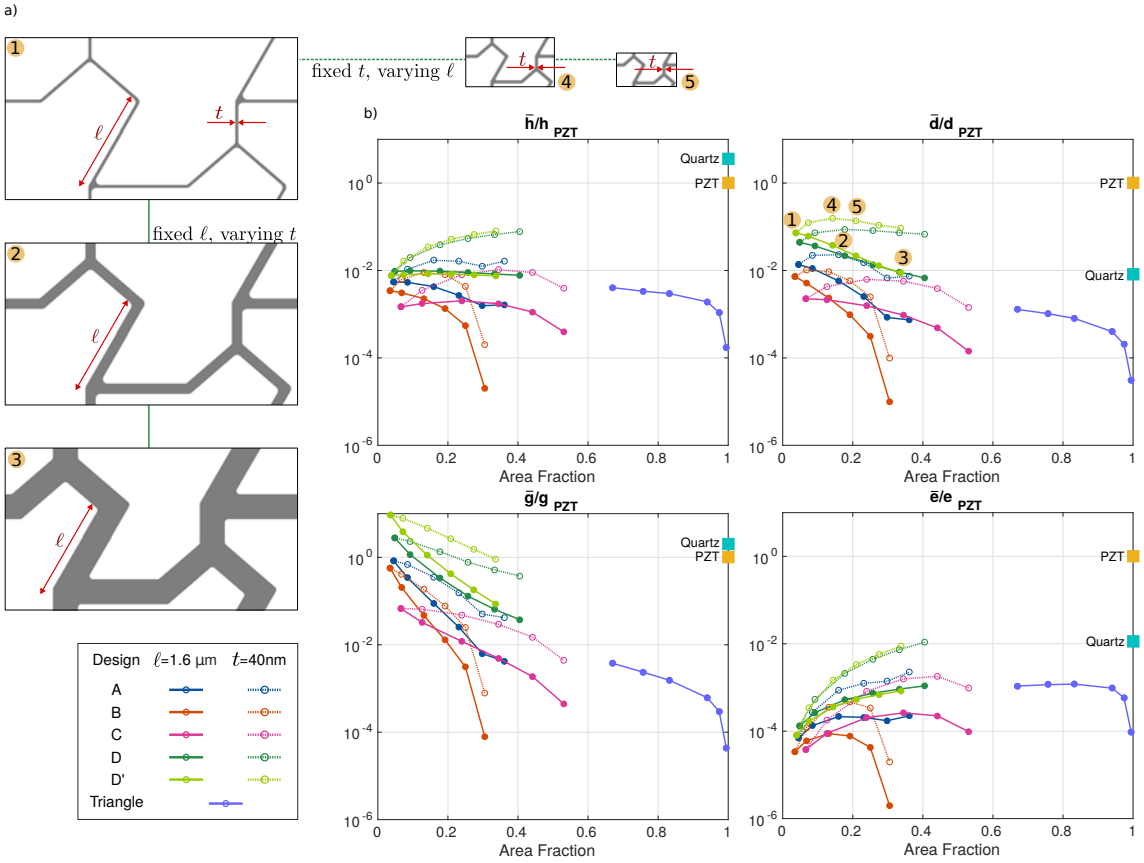

FIGURE 3.11: Systematic examination of effective piezoelectric response of the architected dielectrics, considering the optimal orientation and varying area fraction by either keeping ℓ constant or t constant (a). (b) Piezoelectric coefficients characterizing both sensor and actuator modes, Fig. 3.5 and Eq. (3.1), as a function of area fraction and material design normalized by the coefficients of PZT. We also provide the coefficients of Quartz and the results of the metamaterial with triangular inclusions, Fig. 3.7.

To summarize all these effects of the geometry of microarchitecture, we systematically compared the piezoelectric performance of our geometrically polarized lattices accounting for orientation and area fraction, as quantified by the four coefficients $\bar{g}$, $\bar{h}$, $\bar{d}$ and $\bar{e}$ defined in Fig. 3.5 and Eq. (3.1). For a given design, we considered the maximum of each of these coefficients amongst all directions. As shown in Fig. 3.11a, we chose to vary area fraction in two different ways, by either varying the beam thickness at a fixed beam length of $\ell = 1.6\mu$m with a minimum thickness of $t = 40$nm (solid lines), or by fixing the beam thickness to $t = 40$nm and modifying the beam length between $\ell = 0.16\mu$m and $\ell = 1.6\mu$m (dashed lines). We compared the piezoelectric response of our lattices with the reference values for PZT and quartz [128]. We also compared our low-area fraction designs with the periodic metamaterial based on triangular cavities shown in Fig. 3.7a,b with triangle size ℓ between $\ell = 0.4\mu$m and $\ell = 2.8\mu$m. All these results are summarized in Fig. 3.11b.

This figure shows that the nontrivial competition between slenderness and the amount of material to determine the effective properties manifests itself in different ways depending

on the property. While $\bar{g}$ shows a clear monotonic increase with decreasing area fraction, all other properties exhibit non-monotonic behaviors or little sensitivity to area fraction for some designs and ways to vary area fraction (dashed or solid lines).

Focusing on sensor mode, we find under applied strain ($\bar{h}$) our metamaterials produce significantly lower electric fields as compared to quartz or PZT (2 orders of magnitude smaller). This can be anticipated since our low-area-fraction structures are very compliant. For the same reason, we may expect that for stress or pressure sensor ($\bar{g}$) the compliant metamaterials may significantly deform and produce larger piezoelectric couplings. Indeed this is the case, with responses comparable to those of PZT or quartz for low area fractions, and much better responses than the triangular metamaterial.

A similar picture in actuator mode, where the ability of our metamaterials to develop stress under applied strain is not very performant ($\bar{e}$), but conversely their response when actuation displacements are the figure of merit ($\bar{d}$) is competitive, surpassing quartz and not too far from PZT.

We noticed that irrespective of the effective piezoelectric coefficient and the area fraction, Design D systematically performed better than other designs, without attempting a systematic optimization of the lattice geometry, we wondered whether we could rationally improve our designs by following the principle used at a molecular scale of reducing stiffness to enhance the piezoelectric response [129]. To accomplish this, we simply removed one of the beams forming the triangle in the unit cell of design D, Fig. 3.11a (Design D′). We found that, despite no significant effects were observed in $\bar{h}$ and $\bar{e}$, the new design significantly enhanced the performance of the displacement actuator $\bar{d}$ and the pressure sensor $\bar{g}$, with over 200% performance improvement, Fig. 3.11b.

3.3.5 Generalized-periodic boundary conditions, validation and convergence

Generalized-periodic boundary conditions

The numerical analysis of architected lattices may be challenging due to the need to simulate the response of a large enough portion of the lattice for an accurate representation of the overall response of the lattice bulk, devoid of free surface and boundary conditions effects. In the case of periodic lattices, one can efficiently obtain the bulk response from the study of a representative volume element (RVE) or unit cell exploiting the lattice periodicity, thereby achieving a significant reduction in computational cost. Here, the purpose is to obtain the lattice macroscopic electromechanical response under a macroscopic displacement or stress (sensor mode) and under a macroscopic electric field (actuation mode). For this, classical periodicity boundary conditions need to be generalized to account for non-periodic solution fields.

Consider a uniform prescribed macroscopic strain acting in the vertical direction on the lattice, $\bar{\varepsilon}_{22}$, while all other components are zero. The solution on a rectangular unit cell of dimensions ℓ_x and ℓ_y, Fig. 3.12, satisfies that the vertical jump of the vertical displacement between the top and bottom faces of the unit cell is

$$u_y(x,\ell_y) - u_y(x,0) = [\![u_y]\!]_y = \bar{\varepsilon}_{22}\ell_y, \quad \forall x \in (0,\ell_x), \tag{3.2}$$

while all other jumps are zero. Additionally, in the present high-order theory, the high-order condition

$$\nabla u_y(x, \ell_y) - \nabla u_y(x, 0) = 0, \quad \forall x \in (0, \ell_x). \tag{3.3}$$

is also necessary to ensure $\mathcal{C}^1$ continuity of the solution. Imposing additionally classic periodicity in the horizontal direction, i.e. setting the jumps of displacements and electric potential in the horizontal direction to zero, and assuming the top and bottom faces of the unit cell are free of surface charges,

$$D_2(x, 0) = D_2(x, \ell_y) = 0, \forall x \in (0, \ell_x), \tag{3.4}$$

the vertical jump of the electric potential $[\![\phi]\!]_y$ can be determined by solving the boundary value problem. The macroscopic vertical electric field then yields

$$\bar{E}_2 = -\frac{[\![\phi]\!]_y}{\ell_y}, \tag{3.5}$$

and the corresponding effective piezoelectric coefficient is

$$\bar{h} = -\frac{\bar{E}_2}{\bar{\varepsilon}_{22}}. \tag{3.6}$$

The other three effective piezoelectric coefficients $\bar{g}$, $\bar{d}$, and $\bar{e}$ are obtained by solving an analogous boundary value problem. In each case, either the vertical mechanical jump (resulting form an applied macroscopic strain or stress) or the vertical electric potential jump are prescribed and either the unknown electrical or mechanical macroscopic response is computed by setting their macroscopic work-conjugates to zero, and imposing conventional periodicity in the horizontal direction.

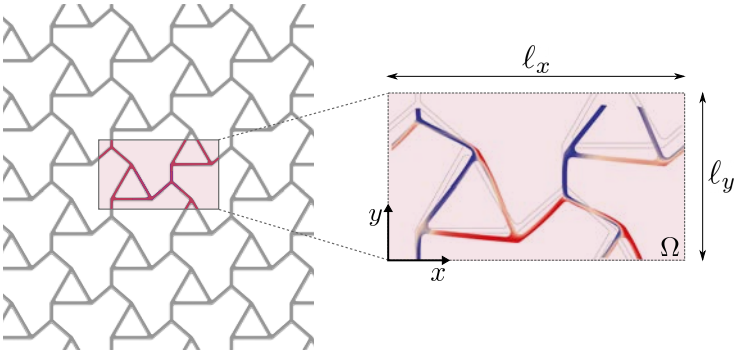

FIGURE 3.12: Representative volume element (RVE) or unit cell of lattice design D.

In order to study the anisotropy of our lattice designs as reported in the main text in Fig. (3), different orientations of the mechanical and electrical loading can be assumed by rotating the macroscopic strain, stress and electric field tensors $\bar{\boldsymbol{\varepsilon}}$, $\bar{\boldsymbol{\sigma}}$, and $\bar{\mathbf{E}}$ as

$$\bar{\boldsymbol{\varepsilon}}^{\alpha} = \mathbf{R}\bar{\boldsymbol{\varepsilon}}\mathbf{R}^T \tag{3.7a}$$

$$\bar{\boldsymbol{\sigma}}^{\alpha} = \mathbf{R}\bar{\boldsymbol{\sigma}}\mathbf{R}^T \tag{3.7b}$$

$$\bar{\mathbf{E}}^{\alpha} = \mathbf{R}\bar{\mathbf{E}} \tag{3.7c}$$

where $\mathbf{R}$ is the two-dimensional rotation matrix $\mathbf{R} = [\cos(\alpha), -\sin(\alpha); \sin(\alpha), \cos(\alpha)]$. This approach is very convenient since it is equivalent to a rotation of the lattice, avoiding however the need to redefine the periodic unit cell for each loading angle. It can be seen in Fig. 3.10, that the expected geometrical symmetries for all the lattices are recovered in the polar plots of the effective piezoelectric coefficients.

Validation

The implementation of the high-order generalized periodic boundary conditions are further validated by comparing the response of the periodic unit cell to that of a lattice strip with increasing number of unit cells with prescribed Dirichlet boundary conditions on the top and bottom faces corresponding to the prescribed macroscopic jumps in each of the four boundary value problems to determine the four effective piezoelectric coefficients. Fig. 3.13 reports the comparison of the computed electric potential jump between the top and bottom faces, for the case of lattice design C with a prescribed macroscopic displacement jump. Excellent agreement for strips of 8 unit cells or more is shown. As expected, the electric potential jump increases linearly with the number of stacked unit cells.

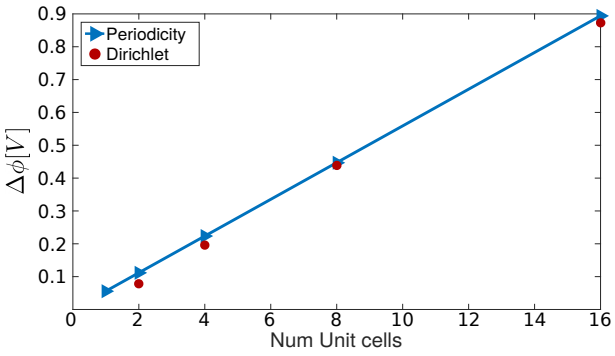

FIGURE 3.13: Electric potential jump as a function of the number of vertically stacked unit cells for lattice Design C in displacement sensor mode.

Convergence

All the simulations reported in this work are performed with a mesh size $h = t/10$, which we term M1, being t the thickness of the lattice structural elements. To test its accuracy and the tradeoff between computational cost and accuracy for finer meshes, we compared the solutions of increasingly fine meshes M1, M2 and M3 with an even finer mesh M4, which we used as a reference solution, Fig. 3.14. To assess accuracy, we plotted the relative error in two quantities of interest, namely the macroscopic electric field $\bar{E}_2$ in sensor mode and the macroscopic strain $\bar{\varepsilon}_{22}$ in actuator mode, as a function of the mesh size for lattice Design D with $t = 160$nm and $\ell = 1.6\mu$m, as defined in Fig. 2 in the main text. We noted that refining the mesh marginally increased accuracy with a much higher computational cost, and hence considered M1 to be converged. We note that the error of M3 relative to M4 does not significantly decrease, likely because discretization errors become comparable to the errors in the linear solver.

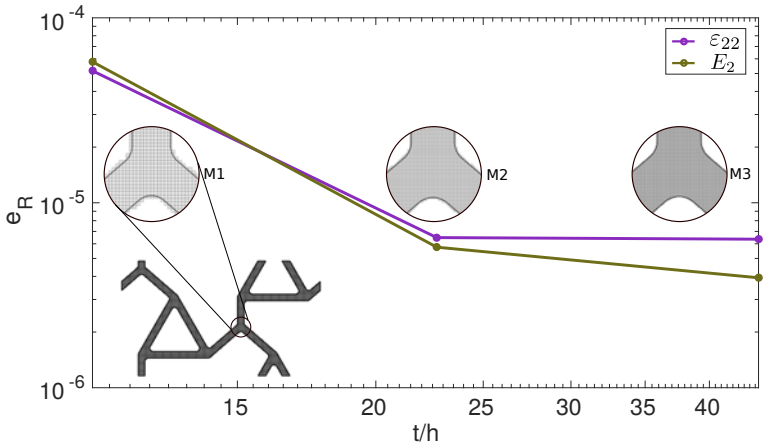

FIGURE 3.14: Relative error of two quantities of interest as a function of the element mesh size h. The inset shows three representative computational mesh details. All simulations in this work have been computed with mesh level M1.

3.4 Concluding remarks

Recent research has highlighted how material architecture can give rise to properties not present in the base material, as illustrated by a variety of electromagnetic/optical, acoustic, o mechanical metamaterials [130]. Piezoelectricity requires lack of centrosymmetry, which can be imprinted molecularly as in most piezoelectrics but in principle can also be imprinted by geometry in an architected material [53, 56]. By using accurate self-consistent calculations of continuum flexoelectricity on general geometries, we have quantified this possibility and proposed a class of effectively piezoelectric low area-fraction, bending dominated and geometrically-polarized metamaterials made of non-piezoelectric base material. These metamaterials exploit a universal small-scale electromechanical coupling, flexoelectricity, and make it available at a meso- or macro-scale in the form of effective piezoelectricity thanks to their non-centrosymmetric and multiscale organization, with small-scale features repeated over much longer length scales.

We have characterized the effective piezoelectric response of these metamaterials depending on geometry, area-fraction at fixed thickness, area-fraction at fixed beam length, and orientation. Since the metamaterials proposed here can be made out of any dielectric, our work provides the rules of geometric design to endow a metamaterial with piezoelectricity under rather general conditions, thus easily introducing material multi-functionality and potentially enabling non-toxic, environmentally friendly, and biocompatible piezoelectrics. If the base material has a significant flexoelectric coupling, we have found that these metamaterials can exhibit significant piezoelectric performance, comparable to the best piezoelectrics as stress sensors or as displacement actuators. Although here we have considered only bulk flexoelectricity as the small-scale electromechanical coupling mechanism, we note that surface piezoelectricity caused by surface relaxation of an otherwise centrosymmetric crystal can also result in a flexoelectric-like response [131]. Likewise, apparent flexoelectricity can be obtained by controlling the heterogeneity of piezoelectric properties [132]. Furthermore, it has been recently shown that fixed charges in a soft material can lead to the so-called flexoelectret effect [20, 133, 134], which enables a significant two-way flexoelectric-like response in millimeter-thick samples. All our results can be directly extrapolated to

these situations, hence broadening the scope of our geometrically-polarized architected dielectrics with effective piezoelectricity.

Our work provides a framework for rational material design to control the magnitude (Design D′) and anisotropy (Fig. 3.10) of effective piezoelectricity. The design of our metamaterials is amenable to systematic computational topology and shape optimization [135] and additive manufacturing [58, 102, 126, 136], and hence may provide an alternative route to conventional piezoelectric material design at a molecular scale [129]. Furthermore, piezoelectricity and flexoelectricity may act constructively if our geometrically polarized lattices are built from an already piezoelectric material, thereby enhancing their effective piezoelectricity[30, 42].

Chapter 4

Computational homogenization of flexoelectric metamaterials

4.1 Introduction

While dealing with composites or metamaterials, the internal microstructure is often made of different phases, also called inhomogeneities, that induce local variations in the field variables (e.g. strain, stress, electric field). In the case of bending-dominated low-area-fraction lattices designed to mimic the behavior of a piezoelectric material, the two phases are represented by (1) the active flexoelectric beams that shape the lattice and (2) the void inclusions. The local variations of the fields reflect in the mechanical strain gradients and/or electric field gradients.

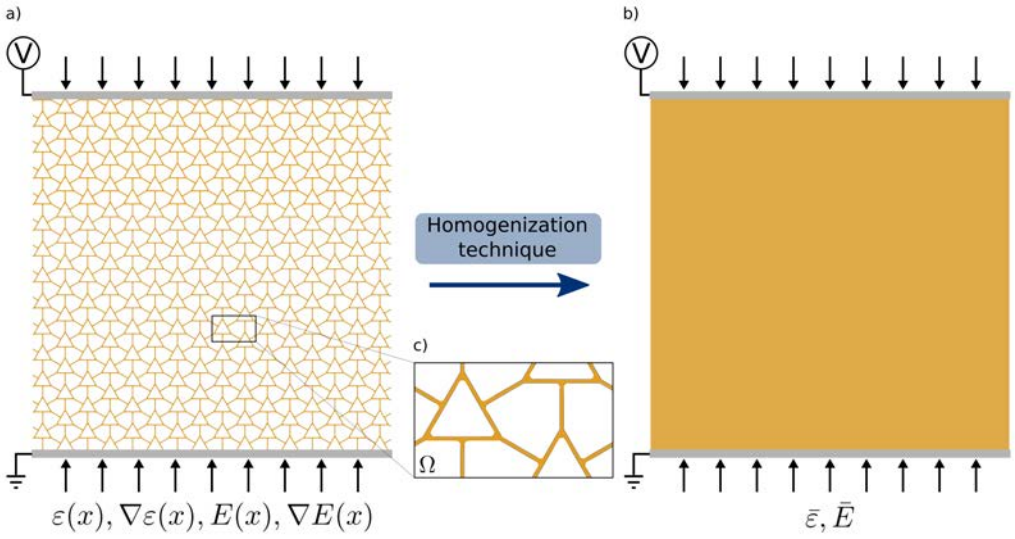

FIGURE 4.1: (a) Heterogeneous structure and (b) its equivalent homogeneous structure. Homogenization techniques convert local fields $(\varepsilon(\mathbf{x}), \nabla\varepsilon(\mathbf{x}), E(\mathbf{x}), \nabla E(\mathbf{x}))$, dependent on the internal structure $(\mathbf{x})$ of the material in the heterogeneous structure, into effective properties $(\bar{\varepsilon}, \bar{E})$ that apply in the equivalent homogeneous medium. (c) The RVE corresponds to the unit periodic cell.

Homogenization techniques are used to convert the local fields $(\varepsilon(\mathbf{x}), \nabla\varepsilon(\mathbf{x}), E(\mathbf{x}), \nabla E(\mathbf{x}))$, dependent on the internal structure $(\mathbf{x})$ of the material in the inhomogeneous structure, Fig. 4.1a, into overall homogenized properties $(\bar{\varepsilon}, \bar{E})$, that apply in the homogeneous medium, Fig. 4.1b, thus upscaling the material properties from the inhomogeneous microstructure

(i.e. where the flexoelectric constituents are described) to the macroscopic scale (i.e. the piezoelectric homogenized medium). The computational domain is identified by the Representative Volume Element (RVE), which for periodic structures subjected to periodic boundary conditions corresponds to the unit periodic cell, as described in Ch. 3 and depicted in Fig. 4.1c.

Several analytical and theoretical methods can be found in literature [137–139], however for complex geometries and physics closed-form solutions are far from trivial, and computational homogenization techniques are required.

In 1967, Adams [140] proposed a method to numerically characterize the macroscopic properties of a composite from its local variations at the microscale. Although this approach is considered to be the first computational homogenization methodology in literature, it still represents an extension of a simpler analytical approach. It is only in the late 1990s that more advanced computational homogenization methods are proposed to solve analytically unapproachable problems [141]. Nowadays, computational homogenization is used in a wide variety of fields ranging from nonlinear [142], to fracture problems [143], to multiphysics and electromechanical coupled problems [144, 145]. Sharma et al. [53] proposed a homogenization technique to solve an effective piezoelectric composite where nanoscale inhomogeneities were embedded within a flexoelectric matrix. The inhomogeneities, having different material properties with respect to the flexoelectric matrix, were treated as fictitious body forces and electric fields. In more recent work [132], a numerical homogenization method was proposed to study the effect of heterogeneous piezoelectric composites able to endow the matrix with a flexoelectric-like response even though the base material has no significant flexoelectricity.

Based on this [146], here we propose a computational homogenization technique for flexoelectric-based metamaterials.

In Ch. 3 we presented some geometrically polarized metamaterials able to exploit the flexoelectric effect and behave as piezoelectric materials [60]. Although at a first stage we focused on the characterization of the *longitudinal piezoelectric modulus*, i.e. the effective response along the loading direction with respect to the lattice orientation, the process of designing more conscious flexoelectric-based metamaterials passes through the awareness of a comprehensive understanding of their enriched properties, reflected in the full characterization of the effective macroscopic behavior and thus full evaluation of the homogenized tensors, which is the contribution of this chapter [61][1].

4.2 Energy equivalence

The periodic unit cell in Fig. 4.1c subjected to periodic boundary conditions is treated as a material point for the homogeneous medium while generates local variations of the fields $(\varepsilon(\mathbf{x}), \nabla\varepsilon(\mathbf{x}), E(\mathbf{x}), \nabla E(\mathbf{x}))$ in its constituents. The base material is chosen to fit the behavior of Barium Strontium Titanate (BST) above the Curie temperature in its paraelectric phase (non-piezoelectric), with composition $Ba_{0.60}Sr_{0.40}Ti_3$, which exhibits high dielectric constant and thus strong flexoelectricity [27]. To model such a material we define the quadratic form of the electric enthalpy $\mathcal{H}^{\langle Lif\rangle}$, introduced in sec. 2.2.2 and reported here to highlight the material coordinates $\mathbf{x}$ dependence of all the quantities involved, therefore implying that

[1] This chapter has been partially extrapolated from: *A.Mocci,P.Gupta, and I.Arias. Shape optimization of architected dielectrics with effective piezoelectricity using computational homogenization.* (In Preparation).

inhomogeneities and local variations are captured by the enthalpy form.

$$\begin{aligned}\mathcal{H}^{\langle Lif\rangle}(\mathbf{u},\phi) =& \frac{1}{2}\varepsilon_{ij}(\mathbf{x})C_{ijkl}(\mathbf{x})\varepsilon_{kl}(\mathbf{x}) + \frac{1}{2}\varepsilon_{ij,k}(\mathbf{x})h_{ijklmn}(\mathbf{x})\varepsilon_{lm,n}(\mathbf{x}) - \frac{1}{2}\phi_{,l}(\mathbf{x})\kappa_{lm}(\mathbf{x})\phi_{,m}(\mathbf{x}) \\ & - \frac{1}{2}\phi_{,mn}(\mathbf{x})b_{mnlk}(\mathbf{x})\phi_{,lk}(\mathbf{x}) + \frac{1}{2}\phi_{,l}(\mathbf{x})\mu_{lijk}(\mathbf{x})\varepsilon_{ij,k}(\mathbf{x}) - \frac{1}{2}\phi_{,lk}(\mathbf{x})\mu_{lijk}(\mathbf{x})\varepsilon_{ij}(\mathbf{x}).\end{aligned} \tag{4.1}$$

The Euler-Lagrange equations, derived from the enthalpy function in Eq. (2.26), are the fourth-order coupled partial differential equations reported here for convenience:

$$(\hat{\sigma}_{ij} - \tilde{\sigma}_{ijk,k})_{,j} = 0 \text{ in } \Omega, \tag{4.2a}$$

$$(\hat{D}_{l,l} - \tilde{D}_{lk,k})_{,l} = 0 \text{ in } \Omega. \tag{4.2b}$$

where we have set the body forces $\bar{\boldsymbol{b}} = \mathbf{0}$ as well as the free electric charges $\bar{q} = 0$.

Following the Hill-Mandel theorem [147, 148], we make a hypothesis that the average of the microscopic work done by the RVE must be equivalent to the macroscopic work done by the fictitious homogeneous material. In order to prescribe this, we write the electric enthalpy of the equivalent piezoelectric medium ($\overline{\mathcal{H}}$) as the average of the electric enthalpy of the flexoelectric RVE ($\mathcal{H}$).

$$\overline{\mathcal{H}} = \left\langle \mathcal{H} \right\rangle = \frac{1}{2}\bar{\varepsilon}_{ij}\overline{C}_{ijkl}\bar{\varepsilon}_{kl} - \overline{E}_l\bar{e}_{lij}\bar{\varepsilon}_{ij} - \frac{1}{2}\overline{E}_i\bar{\kappa}_{ij}\overline{E}_j, \tag{4.3}$$

where $\langle . \rangle = \dfrac{1}{V}\int(.)dV$, with V being the RVE domain volume. By writing the energy in the form of Eq. (4.3), the equilibrium equations turn out

$$\overline{\sigma}_{ij,j} = 0, \quad \overline{D}_{i,i} = 0. \tag{4.4}$$

Now, to prove our hypothesis in Eq. (4.3), we use Hill-Mandel theorem in which we firstly consider the mechanical work done by a flexoelectric metamaterial as

$$\frac{1}{V}\int_V \sigma_{ij}^{eq}\varepsilon_{ij} = \overline{\sigma}_{ik}\bar{\varepsilon}_{ik}, \tag{4.5}$$

where $\sigma_{ij}^{eq} = \widehat{\sigma}_{ij} - \widetilde{\sigma}_{ijk,k}$ is a statically admissible stress such that satisfies the equilibrium equation $\sigma_{ij,j}^{eq} = 0$ and $\varepsilon_{ij} = 1/2(\partial u_{i,j} + \partial u_{j,i})$ a kinematically admissible strain, while the bar quantities are the equivalent macroscopic stress and strain, respectively. Upon volume averaging the Eq. (4.2a) over the RVE domain by multiplying the variation in the displacement field as

$$\frac{1}{V}\int_V \sigma_{ij,j}^{eq}\delta u_i \,\mathrm{d}\Omega = \frac{1}{V}\int_V (\sigma_{ij}^{eq}\delta u_i)_{,j} \,\mathrm{d}\Omega - \frac{1}{V}\int_V \sigma_{ij}^{eq}\delta u_{i,j} \,\mathrm{d}\Omega = 0, \tag{4.6}$$

where Ω is the domain defining the RVE of our architected material. By applying divergence theorem, we write

$$\frac{1}{V}\int_\Gamma \sigma_{ij}^{eq}\delta u_i n_j \;\mathrm{d}\Gamma - \frac{1}{V}\int_V \sigma_{ij}^{eq}\left(\frac{1}{2}(\delta u_{i,j} + \delta u_{j,i}) + \frac{1}{2}(\delta u_{i,j} - \delta u_{j,i})\right) \mathrm{d}\Omega = 0. \tag{4.7}$$

Since, the double contraction of a symmetric tensor with an antisymmetric tensor is zero, therefore

$$\frac{1}{V}\int_{\Gamma}\sigma_{ij}^{eq}\,\delta u_i n_j\;\mathrm{d}\Gamma-\frac{1}{V}\int_{V}\sigma_{ij}^{eq}\delta\varepsilon_{ij}\;\mathrm{d}\Omega=0. \tag{4.8}$$

Now, if the Dirichlet boundary conditions applied to our RVE are such that

$$u_i=\overline{\varepsilon}_{ij}x_j, \tag{4.9}$$

hence using Eq. (4.9) on the boundary integral of Eq. (4.8) we obtain

$$\begin{aligned}\frac{1}{V}\int_{\Gamma}\sigma_{ij}^{eq}\,\delta u_i n_j\;\mathrm{d}\Gamma &= \frac{1}{V}\int_{\Gamma}\sigma_{ij}^{eq}\,\delta\overline{\varepsilon}_{ik}x_k n_j\;\mathrm{d}\Gamma=\frac{\delta\overline{\varepsilon}_{ik}}{V}\int_{\Gamma}\sigma_{ij}^{eq}x_k n_j\;\mathrm{d}\Gamma=\frac{\delta\overline{\varepsilon}_{ik}}{V}\int_{V}(\sigma_{ij}^{eq}x_k)_{,j}\;\mathrm{d}\Omega\\ &= \frac{\delta\overline{\varepsilon}_{ik}}{V}\int_{V}(\sigma_{ij,j}^{eq}x_k+\sigma_{ij}^{eq}\delta_{kj})\;\mathrm{d}\Omega=\overline{\sigma}_{ik}\delta\overline{\varepsilon}_{ik},\end{aligned} \tag{4.10}$$

Finally, using Eqs. (4.8) and (4.10)

$$\frac{1}{V}\int_{V}\sigma_{ij}^{eq}\delta\varepsilon_{ij}=\overline{\sigma}_{ik}\delta\overline{\varepsilon}_{ik}, \tag{4.11}$$

which can also be written in the tensor notation as

$$\langle\boldsymbol{\sigma}^{eq}:\delta\boldsymbol{\epsilon}\rangle=\overline{\boldsymbol{\sigma}}:\delta\overline{\boldsymbol{\epsilon}}. \tag{4.12}$$

This shows that the mechanical work done by the flexoelectric RVE is equivalent to the work done by the homogenized piezoelectric system.

Similarly, we also prove that the electrical work done by the microscopic and macroscopic system is the same.

$$\frac{1}{V}\int_{V}D_i^{eq}E_i\,\mathrm{d}\Omega=\overline{D}_k\overline{E}_k, \tag{4.13}$$

where D_i^{eq} defined as $D_i^{eq}=\widehat{D}_i-\widetilde{D}_{ij,j}$. For this, we volume average Eq. (4.2b) over the RVE domain by multiplying the variation in the electric potential as

$$\frac{1}{V}\int_{V}D_{i,i}^{eq}\,\delta\phi\,\mathrm{d}\Omega=\frac{1}{V}\int_{V}(D_i^{eq}\delta\phi)_{,i}\;\mathrm{d}\Omega-\frac{1}{V}\int_{V}D_i^{eq}\delta\phi_{,i}\,\mathrm{d}\Omega=0, \tag{4.14}$$

an again, by using the divergence theorem

$$\frac{1}{V}\int_{\Gamma}D_i^{eq}\delta\phi n_i\;\mathrm{d}\Gamma-\frac{1}{V}\int_{V}D_i^{eq}\delta\phi_{,i}\,\mathrm{d}\Omega=0. \tag{4.15}$$

Now, if the electrical boundary conditions applied to the RVE are such that

$$\phi=-\overline{E}_k x_k. \tag{4.16}$$

Therefore, by using Eq. (4.16) on the boundary integral of Eq. (4.15) we obtain

$$\begin{aligned}\frac{1}{V}\int_{\Gamma}D_i^{eq}\delta\phi n_i\;\mathrm{d}\Gamma &= -\frac{1}{V}\int_{\Gamma}D_i^{eq}\delta\overline{E}_k x_k n_i\;\mathrm{d}\Gamma=-\frac{\delta\overline{E}_k}{V}\int_{V}(D_i^{eq}x_k)_{,i}\;\mathrm{d}\Omega\\ &= -\frac{\delta\overline{E}_k}{V}\int_{V}(D_{i,i}^{eq}x_k+D_i^{eq}\delta_{ki})\;\mathrm{d}\Omega=-\overline{D}_k\delta\overline{E}_k,\end{aligned} \tag{4.17}$$

where $\overline{D}_k$ is the average electric displacement generated in the equivalent piezoelectric medium. Therefore, from Eqs. (4.15) and (4.17)

$$\frac{1}{V}\int_V D_i^{eq}\delta E_i \,\mathrm{d}\Omega = \overline{D}_k\delta\overline{E}_k, \tag{4.18}$$

or in tensor notation

$$\langle \boldsymbol{D}^{eq}\cdot\delta\boldsymbol{E}\rangle = \overline{\boldsymbol{D}}\cdot\delta\overline{\boldsymbol{E}}. \tag{4.19}$$

Upon superimposing Eqs. (4.12) and (4.19) lead to the conclusion that the work done by the microscopic flexoelectric system and the fictitious piezoelectric medium is the same, which validates our initial hypothesis in Eq. (4.3).

In the next section, we will discuss a methodology that will allow us to fully compute the homogenized material properties of a fictitious piezoelectric material equivalent to our flexoelectric microstructure.

4.3 Effective material tensors in the homogenized piezoelectric medium

Within the linear flexoelectric regime, the equilibrium equations (4.2) can be solved by superimposing macroscopic strains and electric fields as:

$$\begin{aligned}
\varepsilon_{ij}(\mathbf{x}) &= \mathcal{A}_{ijkl}(\mathbf{x})\overline{\varepsilon}_{kl} + \mathcal{B}_{ijk}(\mathbf{x})\overline{E}_k,\\
\varepsilon_{ijm}(\mathbf{x}) &= \mathcal{A}'_{ijmkl}(\mathbf{x})\overline{\varepsilon}_{kl} + \mathcal{B}'_{ijmk}(\mathbf{x})\overline{E}_k, \quad \mathcal{A}'_{ijmkl} = \mathcal{A}_{ijkl,m}, \quad \mathcal{B}'_{ijmk} = \mathcal{B}_{ijk,m},\\
E_i(\mathbf{x}) &= \mathcal{G}_{ijk}(\mathbf{x})\overline{\varepsilon}_{jk} + \mathcal{H}_{ij}(\mathbf{x})\overline{E}_j,\\
E_{im}(\mathbf{x}) &= \mathcal{G}'_{imjk}(\mathbf{x})\overline{\varepsilon}_{jk} + \mathcal{H}'_{imj}(\mathbf{x})\overline{E}_j, \quad \mathcal{G}'_{imjk} = \mathcal{G}_{ijk,m}, \quad \mathcal{H}'_{imj} = \mathcal{H}_{ij,m}.
\end{aligned} \tag{4.20}$$

The unknowns tensors $(\boldsymbol{\mathcal{A}}, \boldsymbol{\mathcal{B}}, \boldsymbol{\mathcal{G}}, \boldsymbol{\mathcal{H}})$, also referred as *concentration tensors*, relate microscopic strains (or electric fields) to macroscopic strains (or electric fields), while their derivatives $(\boldsymbol{\mathcal{A}}', \boldsymbol{\mathcal{B}}', \boldsymbol{\mathcal{G}}', \boldsymbol{\mathcal{H}}')$ relate microscopic strain gradients (or electric field gradients) to macroscopic strains (or electric fields). From here, by substituting Eqs. (4.20) into the enthalpy form in Eq. (4.1), the effective fourth-order stiffness tensor $\overline{\mathbf{C}}$, second-order dielectric tensor $\overline{\boldsymbol{\kappa}}$ and third-order piezoelectric tensor $\overline{\mathbf{e}}$ can be computed as:

$$\begin{aligned}
\overline{\mathbf{C}} = \Big\langle\ & \boldsymbol{\mathcal{A}}^T : \mathbf{C} : \boldsymbol{\mathcal{A}} + \boldsymbol{\mathcal{A}}'^T \vdots \mathbf{H} \vdots \boldsymbol{\mathcal{A}}' - \boldsymbol{\mathcal{G}}^T\cdot\boldsymbol{\mu}\vdots\boldsymbol{\mathcal{A}}' + \boldsymbol{\mathcal{G}}'^T : \boldsymbol{\mathcal{D}} : \boldsymbol{\mathcal{A}}\\
& - \boldsymbol{\mathcal{G}}^T\cdot\boldsymbol{\kappa}\cdot\boldsymbol{\mathcal{G}} - \boldsymbol{\mathcal{G}}'^T : \mathbf{G} : \boldsymbol{\mathcal{G}}'\Big\rangle, \quad \text{with} \quad \mathcal{A}'_{ijkab} = \mathcal{A}'^T_{abijk}.
\end{aligned} \tag{4.21}$$

$$\begin{aligned}
\overline{\boldsymbol{\kappa}} = \Big\langle\ & -\boldsymbol{\mathcal{B}}^T : \mathbf{C} : \boldsymbol{\mathcal{B}} - \boldsymbol{\mathcal{B}}'^t \vdots \mathbf{H} \vdots \boldsymbol{\mathcal{B}}' + \boldsymbol{\mathcal{H}}^T\cdot\boldsymbol{\mu}\vdots\boldsymbol{\mathcal{B}}' - \boldsymbol{\mathcal{H}}'^T : \boldsymbol{\mathcal{D}} : \boldsymbol{\mathcal{B}}\\
& + \boldsymbol{\mathcal{H}}^T\cdot\boldsymbol{\kappa}\cdot\boldsymbol{\mathcal{H}} + \boldsymbol{\mathcal{H}}'^T : \mathbf{G} : \boldsymbol{\mathcal{H}}'\Big\rangle, \quad \text{with} \quad \mathcal{B}'_{ijkc} = \mathcal{B}'^t_{cijk}.
\end{aligned} \tag{4.22}$$

$$\bar{\mathbf{e}} = \Big\langle -\boldsymbol{\mathcal{A}}^T : \mathbf{C} : \boldsymbol{\mathcal{B}} - \boldsymbol{\mathcal{A}}'^T : \mathbf{H} : \boldsymbol{\mathcal{B}}' + \boldsymbol{\mathcal{G}}^T \cdot \boldsymbol{\kappa} \cdot \boldsymbol{\mathcal{H}} + \boldsymbol{\mathcal{G}}'^T : \mathbf{G} : \boldsymbol{\mathcal{H}}' + \frac{1}{2}\Big[\boldsymbol{\mathcal{H}}^T \cdot \boldsymbol{\mu} \vdots \boldsymbol{\mathcal{A}}' + \boldsymbol{\mathcal{G}}^T \cdot \boldsymbol{\mu} \vdots \boldsymbol{\mathcal{B}}' - \boldsymbol{\mathcal{H}}'^T : \boldsymbol{\mathcal{D}} : \boldsymbol{\mathcal{A}} - \boldsymbol{\mathcal{G}}'^T : \boldsymbol{\mathcal{D}} : \boldsymbol{\mathcal{B}}\Big] \Big\rangle. \tag{4.23}$$

Here, $(\cdot)$ denotes contraction of the first index, $(:)$ denotes contraction of the first two indices and $(\vdots)$ denotes contraction of the first three indices.

4.3.1 Computational homogenization: numerical approach

The flexoelectric metamaterial proposed in Ch. 3 presents a periodic microstructure in both x and y direction, which allows us to easily identify the RVE and thus reduce the whole computation by merely imposing generalized periodicity condition to our computational domain. The reader is referred to Ch. 3 and App. A for further details about the imposition of the aforementioned boundary conditions. The boundary value problem is then solved by using the already presented immersed boundary B-Spline method [59].

To computationally determine the unknown concentration tensors and their derivatives, we perform a set of five numerical simulations by changing the applied boundary conditions, as reported in Table 4.1. The numerical solutions of local strains and electric fields are used to fill the unknown components of the concentration tensors.

The first three simulations allow to compute $\boldsymbol{\mathcal{A}}, \boldsymbol{\mathcal{G}}, \boldsymbol{\mathcal{A}}', \boldsymbol{\mathcal{G}}'$. For each simulation the applied macroscopic strain $(\bar{\boldsymbol{\varepsilon}})$ is varied as shown in Table 4.1 while the macroscopic electric field $(\overline{\mathbf{E}})$ remains constant to a first-order null tensor.

Unknown tensors	Varied	Constant
$\boldsymbol{\mathcal{A}}, \boldsymbol{\mathcal{G}}, \boldsymbol{\mathcal{A}}', \boldsymbol{\mathcal{G}}'$	**1.** $\bar{\boldsymbol{\varepsilon}} := \begin{bmatrix} 1 & 0 \\ 0 & 0 \end{bmatrix}$ **2.** $\bar{\boldsymbol{\varepsilon}} := \begin{bmatrix} 0 & 1/2 \\ 1/2 & 0 \end{bmatrix}$ **3.** $\bar{\boldsymbol{\varepsilon}} := \begin{bmatrix} 0 & 0 \\ 0 & 1 \end{bmatrix}$	$\overline{\mathbf{E}} := \begin{bmatrix} 0 \\ 0 \end{bmatrix}$
$\boldsymbol{\mathcal{B}}, \boldsymbol{\mathcal{H}}, \boldsymbol{\mathcal{B}}', \boldsymbol{\mathcal{H}}'$	**4.** $\overline{\mathbf{E}} := \begin{bmatrix} 1 \\ 0 \end{bmatrix}$ **5.** $\overline{\mathbf{E}} := \begin{bmatrix} 0 \\ 1 \end{bmatrix}$	$\bar{\boldsymbol{\varepsilon}} := \begin{bmatrix} 0 & 0 \\ 0 & 0 \end{bmatrix}$

TABLE 4.1: Numerical boundary conditions used to determine the unknown concentration tensors and their derivatives.

In regards to the last two numerical simulations, the macroscopic electric field tensor is varied as reported in Table 4.1, while the macroscopic strain tensor is set to a constant second-order null tensor. Thus, local solutions for the remaining concentration tensors $\boldsymbol{\mathcal{B}}, \boldsymbol{\mathcal{H}}, \boldsymbol{\mathcal{B}}', \boldsymbol{\mathcal{H}}'$ are obtained.

By replacing the obtained concentration tensors and their derivatives in Eqs. (4.21)-(4.23), we can compute the effective material parameters.

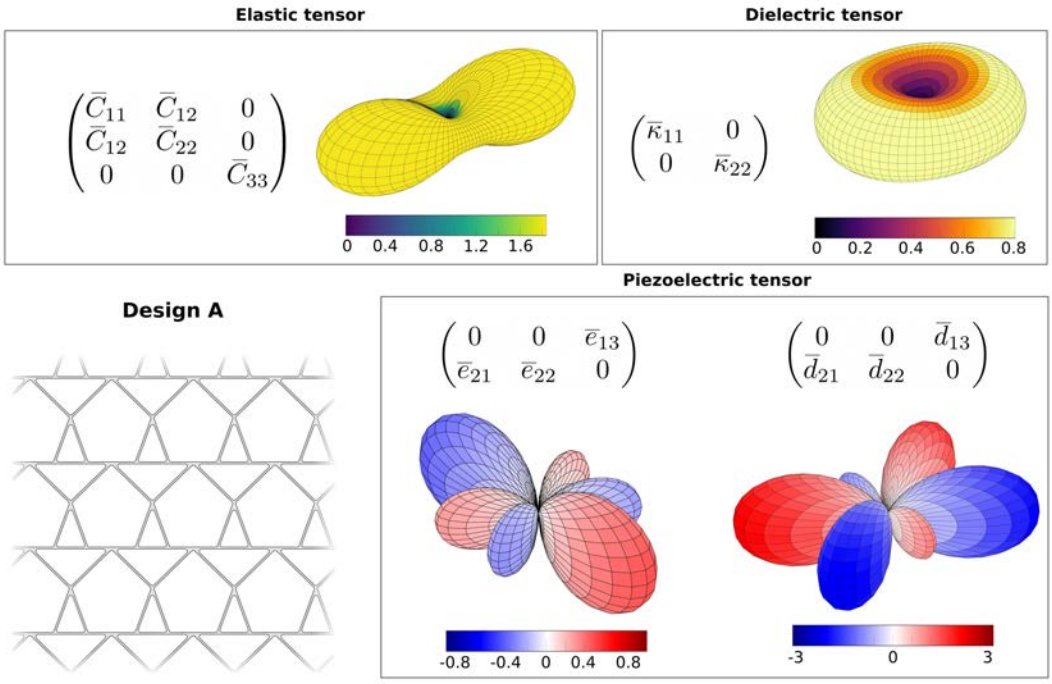

FIGURE 4.2: Effective elasticity, dielectricity and piezoelectricity tensors for Design A and their surface representation.

4.4 Results and Discussions

In this Section, we present the effective elastic tensor, dielectric tensor and piezoelectric tensors for the five two-dimensional lattices (A, B, C, D & D′), as discussed in Ch. 3. All these effective tensors are obtained using computational homogenization technique that we have proposed earlier.

4.4.1 Surface representation and symmetries

All the non-zero coefficients of the 2D effective tensors obtained from the computational homogenization technique are shown in Figs. 4.2-4.6. For each of them, we also graphically show the tensor spherical surface representation to highlight their symmetries. The reader is referred to App.B for further details about the aforementioned representation. At this stage, nominal material parameters have been kept constant, the key values are reported in Table 3.2. In each figure we show the effective elasticity $\bar{\mathbf{C}}$ and dielectricity $\bar{\boldsymbol{\kappa}}$ tensors, as well as the effective piezoelectricity, for which we choose to show only the most relevant of the four piezoelectric tensors introduced in Eq. (3.1), namely the $\bar{\mathbf{e}}$ and $\bar{\mathbf{d}}$ tensors. The former is directly derived from the enthalpy form, Eq. (4.23) (see App. B), while the latter is the most widely used piezoelectric coefficient. Table 4.2 lists the numerical values of all the non-zero coefficients of the effective tensors for the five designs. The piezoelectric $\bar{\mathbf{h}}$ tensor is also reported.

We first evaluated effective tensors for design A. With the help of computational homogenization we found that the effective elastic and dielectric tensor exhibit orthotropic symmetry [149–151]. However, effective piezoelectric tensor exhibits cubic symmetry (23 point group). The surface representation and the symmetries present within these effective tensors have been shown in Fig. 4.2. Interestingly, we found that $\bar{C}_{11}$ is much larger than

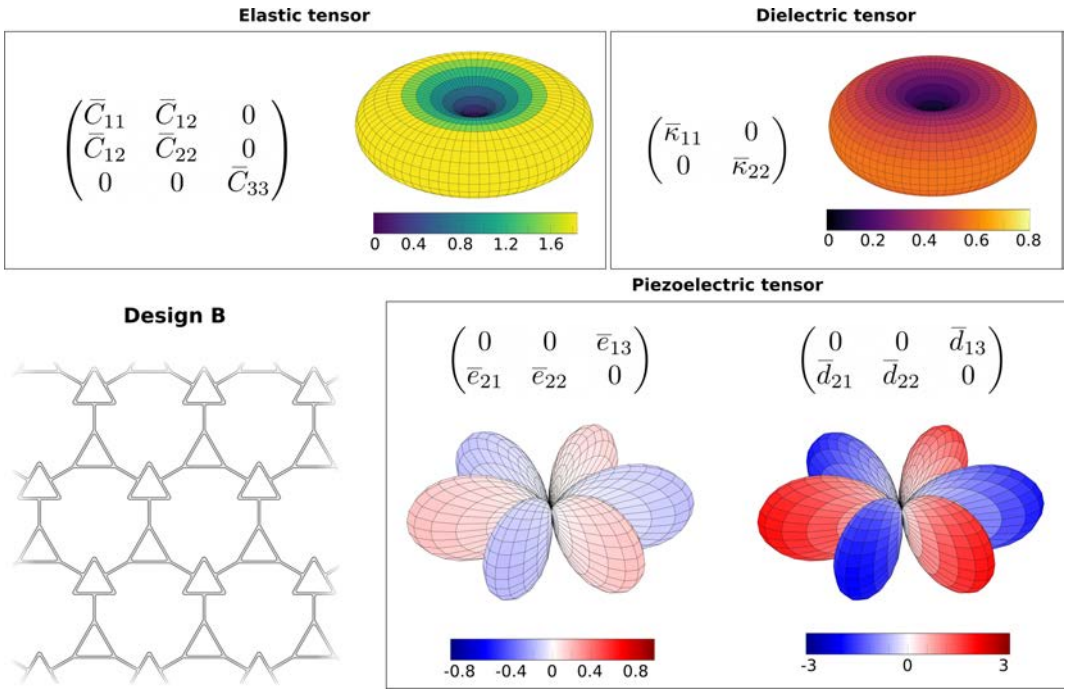

FIGURE 4.3: Effective elasticity, dielectricity and piezoelectricity tensors for Design B and their surface representation.

$\bar{C}_{22}$, cf. Table 4.2, which implies that the material provides more resistance to the deformation in y-direction. Similarly, we found that $\bar{\kappa}_{11}$ is greater than $\bar{\kappa}_{22}$. However, in the case of the effective piezoelectric stress-charge tensor $\bar{\mathbf{e}}$ [152], the transverse shear mode component ($\bar{e}_{13}$) is largest in magnitude when compared with longitudinal and transverse coefficients. A similar trend is observed in the effective piezoelectric strain-charge $\bar{\mathbf{d}}$ and $\bar{\mathbf{h}}$ tensors. This behavior, similar to that of strong piezoelectrics such as PZT, which also exhibits largest shear piezoelectricity, implies that our proposed design A generates large polarization when subjected to shear strain and thus can be effectively used as a shear-based energy harvester [153–155]. It is indeed well known that in energy harvesting, the operation mode strongly affects the quantification of the *electromechanical coupling coefficient*, evaluated as a measure of the capability of the device to convert the input mechanical energy into electrical energy. For design B and design C we found that the effective elastic tensor has square (tetragonal) symmetry. However, the effective dielectric tensor behaves isotropically while the effective piezoelectric tensors, which present three coefficients having the same magnitude, exhibit rectangular symmetry. Since our piezoelectric coefficients are same in all the directions, the device can be readily used for either transverse shear, transverse or longitudinal operation mode, indifferently. Based on the magnitudes we also found out that design B works better than design C in both actuator mode ($\bar{\mathbf{d}}$) as well as sensor mode ($\bar{\mathbf{h}}$) when displacements and electric potential are measured respectively. On the contrary, design C performs better in actuator mode ($\bar{\mathbf{e}}$) when stresses/forces are measured. Fig. 4.3 and 4.4 represent the surfaces for these effective tensors for design B and C respectively. Finally, we studied the most performant designs D and D′. As anticipated by the lack of symmetry in the geometries, we noticed that both design D and D′ are fully anisotropic. The designs and their surface representation can be seen from Fig. 4.5 and 4.6. In general, we noticed that both designs are significantly more compliant than the others, which partially explains the better perfomance. For design D, we further notice that the sensor performs better in transverse shear

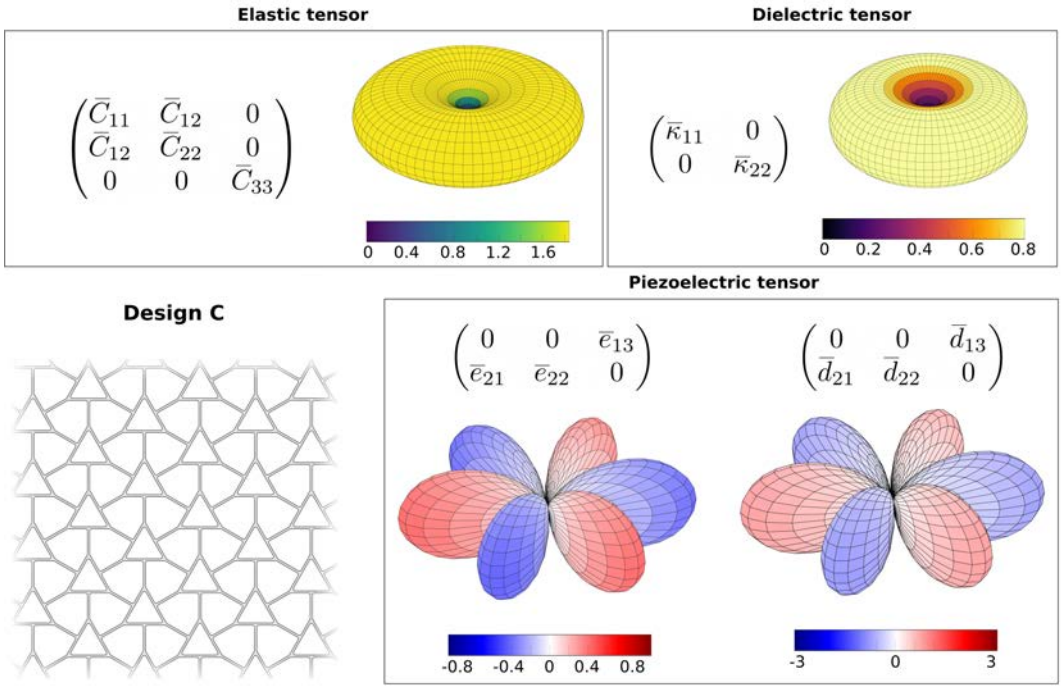

FIGURE 4.4: Effective elasticity, dielectricity and piezoelectricity tensors for Design C and their surface representation.

mode since $\bar{h}_{13}$ has the highest magnitude. A similar behavior was found for the stress-charge $\bar{\mathbf{e}}$. On the contrary, an increased efficiency can be obtained for actuator in transverse operation mode as quantified by the highest $\bar{d}_{21}$ coefficient. On the other side, design D′ was found to be suitable for transverse operation mode [156], regardless of the quantified piezoelectric tensor.

4.4.2 Effect of the nominal material properties

We have tested the effect of the nominal elastic and electric material properties, i.e. Young's modulus, and dielectric permittivity, on the homogenized material. All the other material parameters, including the flexoelectric coefficients have been kept to the values reported in Table 3.2. We first vary the nominal Young's modulus in a range between 120GPa and 250GPa (isotropic elasticity) while keeping the nominal dielectric permittivity to be constant with its value $\epsilon = 8$nC/Vm. The results of the homogenization method are reported in Fig. 4.7. In these plots we have normalized each measured quantity by the reference value $Y = 120$GPa. Self-evidently, within the linear theory, the 6 non-zero independent components of the effective stiffness tensor $\bar{\mathbf{C}}$ increase linearly as the Young's modulus increases for all the five designs. However, rest other effective tensors, i.e. dielectric and piezoelectric tensors are nonlinear in nature. The rate of variation is quite slow in the effective dielectric tensor for all the designs. This is due to the fact that the magnitude of the coupling stiffness tensor $\mathcal{B}$ in Eq. (4.22) is low as compared to $\mathcal{A}$. As the nominal Young's modulus is increased the magnitude of the charge-stress $\bar{\mathbf{d}}$ tensor decreases for all the designs since it is inversely proportional to the elasticity tensor. For $\bar{\mathbf{h}}$ nearly all components increases as the elastic stiffness is increased for all designs, however, the horizontal longitudinal performance $\bar{h}_{11}$ of design A and D′ decreases. A similar effect has been observed for the transverse $\bar{h}_{12}$ and longitudinal shear $\bar{h}_{23}$ components of design C and D respectively. Nevertheless, it is worth

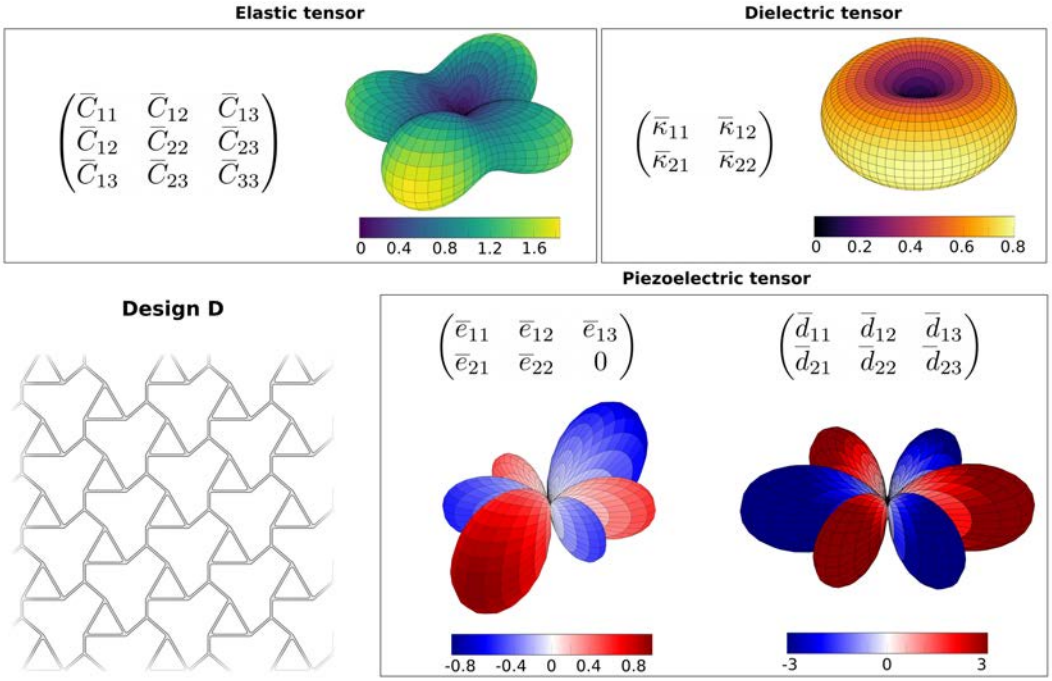

FIGURE 4.5: Effective elasticity, dielectricity and piezoelectricity tensors for Design D and their surface representation.

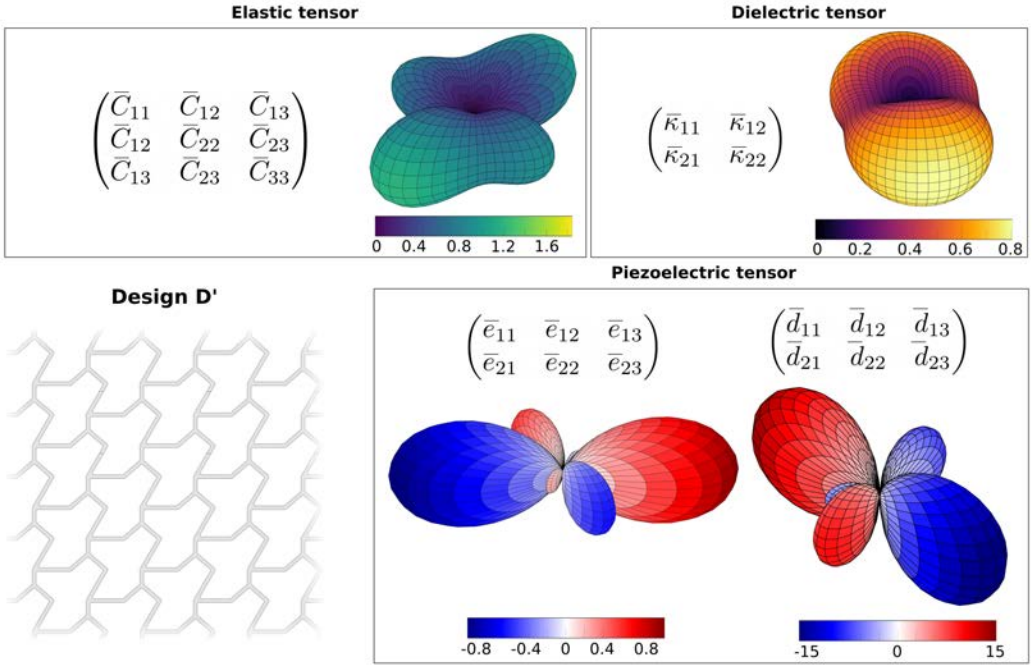

FIGURE 4.6: Effective elasticity, dielectricity and piezoelectricity tensors for Design D′ and their surface representation.

TABLE 4.2: Effective tensors coefficients

Coefficient	Design A	Design B	Design C	Design D	Design D′
C_{11} [GPa]	13.8	2.7	9.4	1.1	0.9
C_{22} [GPa]	4.6	2.7	9.4	1.2	0.8
$C_{12} = C_{21}$ [GPa]	3.5	1.8	4	-0.2	0.1
C_{33} [GPa]	1.1	0.45	2.7	1	0.2
C_{13} [GPa]	-	-	-	0.4	0.3
C_{23} [GPa]	-	-	-	-0.2	-0.003
κ_{11} [nC/Vm]	1.1	0.6	1.5	0.7	0.5
κ_{22} [nC/Vm]	0.9	0.6	1.5	0.7	0.7
$\kappa_{12} = \kappa_{21}$ [nC/Vm]	-	-	-	0.05	0.1
h_{11} [GV/m]$\times 10^{-4}$	-	-	-	-59	-1.5
h_{22} [GV/m]$\times 10^{-4}$	-50	-31.7	-28.3	69	108
h_{21} [GV/m]$\times 10^{-4}$	-36	31.7	28.3	-87	-146
h_{12} [GV/m]$\times 10^{-4}$	-	-	-	46	79
h_{13} [GV/m]$\times 10^{-4}$	58	31.7	28.3	-110	-18
h_{23} [GV/m]$\times 10^{-4}$	-	-	-	8	-30
e_{11} [mN/Vm]$\times 10^{-4}$	-	-	-	-48.1	-21.4
e_{22} [mN/Vm]$\times 10^{-4}$	-48.9	-17.8	-41.2	55.4	83.8
e_{21} [mN/Vm]$\times 10^{-4}$	-35.2	17.8	41.2	-69.7	-98.1
e_{12} [mN/Vm]$\times 10^{-4}$	-	-	-	37.9	53.2
e_{13} [mN/Vm]$\times 10^{-4}$	63.8	17.8	41.2	-80.9	-13.2
e_{23} [mN/Vm]$\times 10^{-4}$	-	-	-	0.06	-22.7
d_{11} [pm/V]	-	-	-	-1.5	3.4
d_{22} [pm/V]	-1.1	-2	-0.8	4.5	7.3
d_{21} [pm/V]	0.01	2	0.8	-6.9	-12.9
d_{12} [pm/V]	-	-	-	1.8	6.7
d_{13} [pm/V]	3	2	0.8	-3.5	-6.7
d_{23} [pm/V]	-	-	-	1.8	5.4

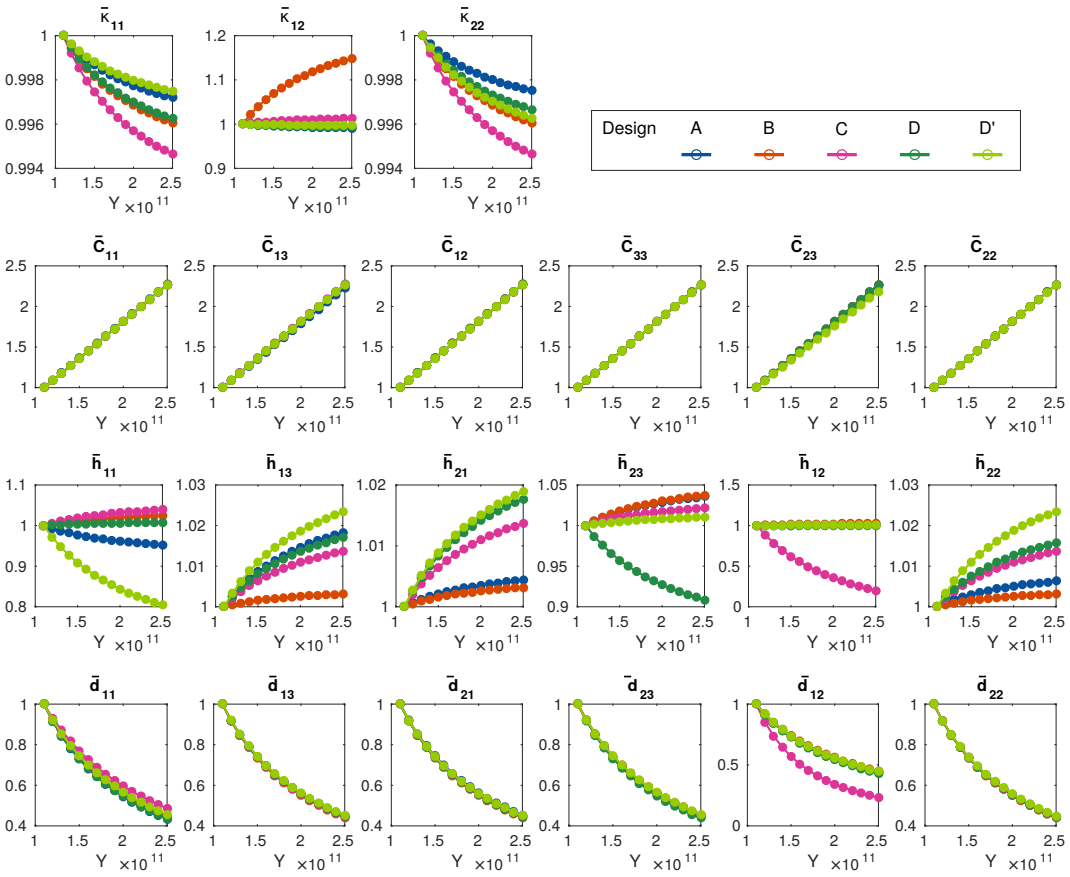

FIGURE 4.7: Non-zero independent components for the dielectricity, elasticity and piezoelectricity tensors as a function of the nominal Young's modulus.

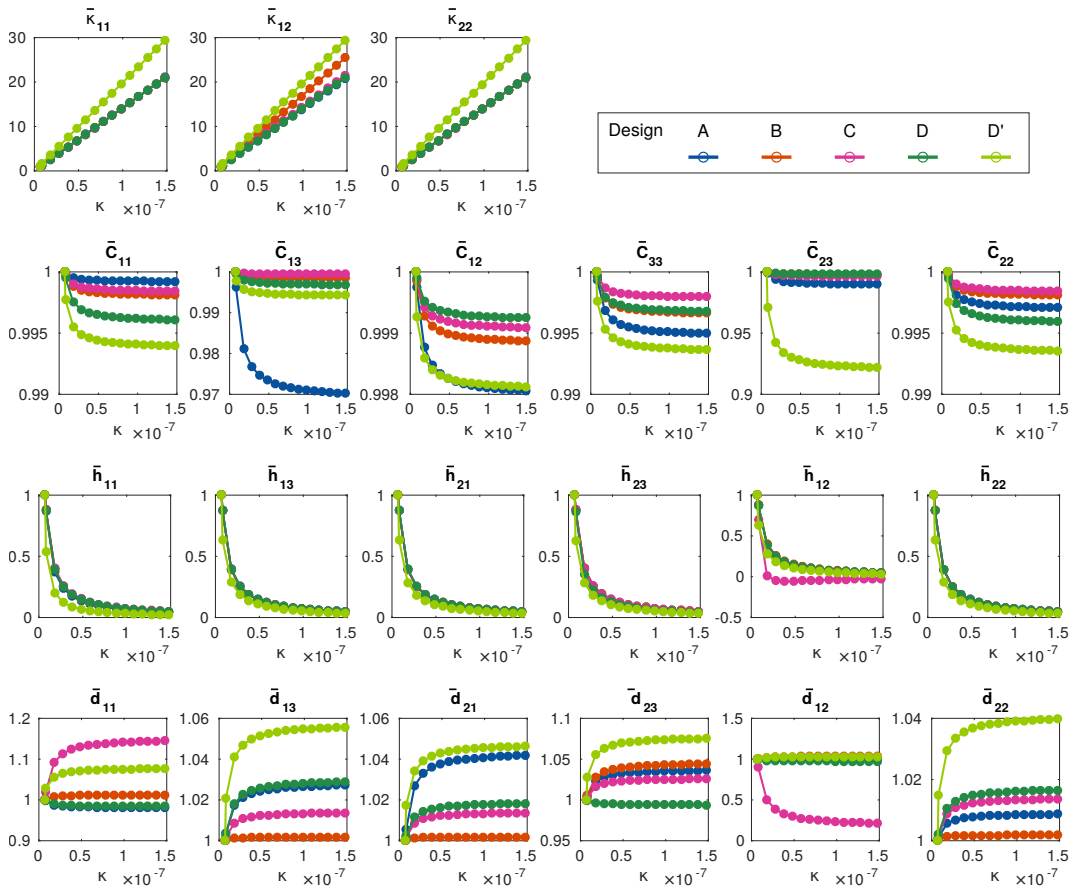

FIGURE 4.8: Non-zero independent components for the dielectricity, elasticity and piezoelectricity tensors as a function of the nominal Young's modulus.

mentioning that the rate of change of the effective $\bar{\mathbf{h}}$ tensor is much slow if compared with the stress-charge tensor $\bar{\mathbf{d}}$, implying that Young's modulus strongly affects the performance of our lattices in actuator mode while its effect is almost negligible for sensors.

A complementary picture is shown for the variation of the dielectric permittivity at fixed stiffness $Y = 152$GPa, Fig. 4.8. We ranged the dielectric permittivity between 8nC/Vm and 150nC/Vm. Analogously to the previous discussion, all the components of the effective dielectric tensor monotonically increase as the dielectric permittivity increases for all the designs. Furthermore, small changes were observed in the effective elastic tensor due to the varying κ. As regard the effective piezoelectricity, the $\bar{\mathbf{h}}$ tensor is inversely proportional to the dielectric permittivity, and hence its performance. For $\bar{\mathbf{d}}$ nearly all the coefficients increase with dielectricity, even though the influence of κ on actuator mode quantified by $\bar{\mathbf{d}}$ is almost negligible.

4.5 Concluding remark

We have proposed an efficient computational homogenization technique and provide the full elastic, dielectric and piezoelectric characterization of five of the lattices presented in Ch. 3 (A-D′). Although the proposed technique referred to 2D lattices with a homogeneous base material, it has been conceived in anticipation of 3D structures, multi-material [157] or hierarchical [136] designs. Even though our lattices have been conceived to perform as longitudinal devices, unexpectedly, the enriched analysis indicates that for some designs the

larger effective piezoelectric coefficient is not the longitudinal one, but instead the shear or the transverse, hence, suggesting the preferred operation mode of each of our lattices for the effective piezoelectric tensor of interest. According to our previous intuition designs B and C exhibit a larger longitudinal piezoelectric coefficient, and can thus be identified as suitable for longitudinal sensors or actuators. On the contrary, design A, D and D′ manifest a larger transverse shear and transverse coefficient with respect to the longitudinal evaluated along the loading direction.

Chapter 5

On-going work

In Chapter 3 we have introduced a class of 2D low-area fraction lattices, analyzed the effect of lattice geometry, orientation and area fraction and proved that even without attempting a methodical optimization of the geometries we were able to considerably improve the performance of our lattices. In Chapter 4 we have quantified the full piezoelectric tensor and gained insights on the overall behavior of our lattices. Design D′ has proven itself to be the most effective design, in different operation modes.

In this chapter we will present a preliminary systematic shape-parameters optimization study of the 2D bending-dominated lattices in order to seek the optimal shape for a given topological configuration. Finally, we will perform a more general optimization analysis including the effect of the nominal material properties on the performance of our lattice.

5.1 Optimization methods

The numerical optimization has been performed by merging the already existing MatLab optimization toolbox with our immersed boundary B-spline framework. We employed different optimization algorithms all of them apt for constrained and unconstrained problems. The methods can be classified in two main subcategories, namely *gradient-based* and *stochastic*. In the following, we will briefly discuss their leading features.

5.1.1 Gradient-based methods

All gradient-based algorithms for optimization have some common features. In general these methods, as suggested by their name, at each step evaluate gradients to identify the search direction for the next point. As a consequence, all the functions that define the problem (i.e. objective and restriction functions), as well as the design variables are assumed to be continuous within the feasible design space.

The optimization problem is mathematically stated as

$$\min_{x_{1,\dots,n}} f(x) \quad \text{such that} \begin{cases} Ax \leq b, & A = [A^1_{x_1}, ..., A^1_{x_n}; ...; A^N_{x_1}, ..., A^N_{x_n}], \\ & b = [b^1, ..., b^N]^T; \\ c(x) \leq 0, & \text{non-linear constraints;} \\ l_b \leq x \leq u_b, & \text{lower and upper bound for the solution.} \end{cases} \tag{5.1}$$

where $f(x)$ is the continuous and differentiable *objective function*, with $x = [x_1, ..., x_n]^T$ being a $n-$vector representing the minimizers, also called *design variables*, for the objective function under consideration. The general structure of all gradient-based methods is described in the

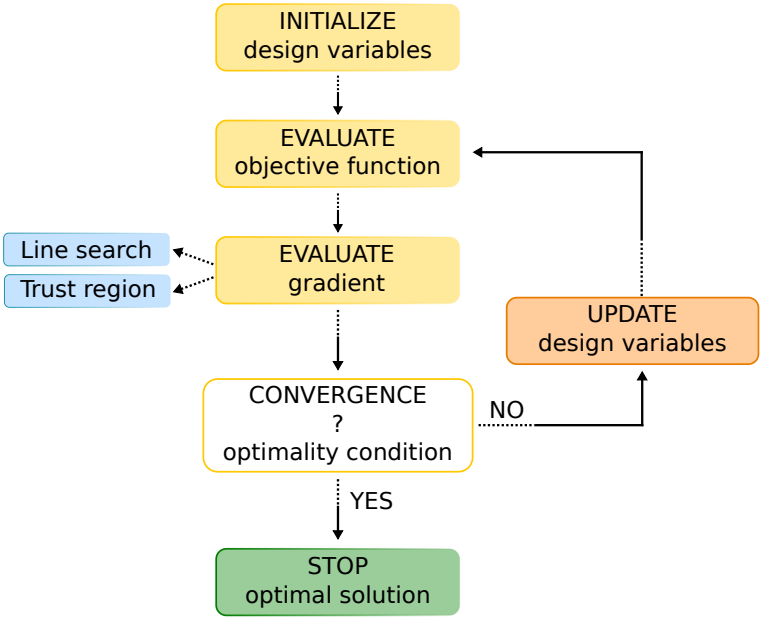

FIGURE 5.1: Gradient-based algorithm for optimization.

chart in Fig. 5.1 and can be outlined as follow:

1. Initialization of the design variables. The algorithm starts at iteration $k = 0$, at a starting point $x_0 = [x_{01}, ..., x_{0n}]$.
2. Evaluation of the objective function $f(x_0)$.
3. Evaluation of the gradient. At each step the algorithm generates a new vector x_k and computes a search direction d_k that represents the $n-$space direction in which to seek for the optimal solution.
4. Computes a step length that satisfies $f(x_{k+1}) < f(x_k)$ and updates the design variables for the following step x_{k+1}.
5. The algorithm stops when the optimality conditions are satisfied.

Notwithstanding the common features, different gradient-based methods differ from each other in the algorithm that computes the search direction d_k. These algorithms can be subdivided in two main subcategories:

- *Line search*. At each iteration k the algorithm compute a search direction d_k along with it will search for the optimal step length $\alpha_k > 0$ in order to minimize the objective function $f(x)$, such that $f(x_{k+1}) < f(x)$, being $x_{k+1} = x_k + \alpha_k d_k$.
- *Trust Region*. At iteration k these algorithms first compute the step length by identifying a trust region in the neighborhood B of the point x_k. The peculiarity of this region is that the function $f(x)$ can there be approximated by a simpler function $q(s)$, such that a subproblem can be stated as:

$$\min_s q(s) \quad \text{with} \quad s \in B, \tag{5.2}$$

if the minimizer s of the subproblem is such that $f(x + s) < f(x)$ the design variables are updated, otherwise the trust region is shrunk and the process is repeated. A scheme

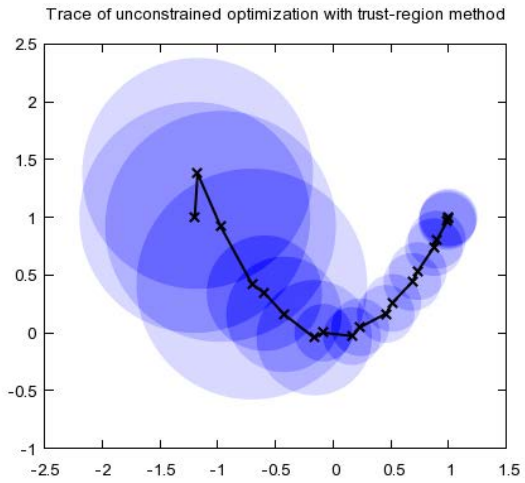

FIGURE 5.2: At each step the trust region is identified in order to better approximate the objective function $f(x_k)$. The picture has been taken from https://optimization.mccormick.northwestern.edu/index.php/Trust-region_methods.

of the trust region approach is reported in Fig. 5.2. The choice of the trust region B, of the approximant function and the accuracy of the solution of the subproblem represent the key issues for these methods.

Gradient-based methods are generally efficient, however, it is worth mentioning that besides the need for continuous and differentiable functions, these methods are strongly affected by the choice of the initial set of minimizers which can lead the algorithm to seek a local minimum.

5.1.2 Genetic, population-based methods

Genetic algorithms, suitable for problems where the function is non-differentiable or stochastic, are named by their ability to randomly mimic biological evolution and natural selection processes. Figure 5.3 schematically show a population-based algorithm for optimization, terminology is also reported.

1. The algorithm starts at iteration $k = 0$ by creating an initial population of individuals defined by a string of parameters allocated similarly to a biological structure. The set of parameters that defines each individual are the variables (*genes*), which in turn are part of the solution (*chromosome*), see Fig. 5.3. Therefore each individual represents a solution for the objective function and the population represents a set of solutions.

2. The evaluation of the so-called *fitness function* states the fitness level of the entire population by assigning at each individual a fitness score, which corresponds to the probability of being chosen for the generation of the next population.

3. The algorithm kills the unfit individuals. The remaining are selected as *parents* and will contribute to the generation of the next population by passing their genes to their *children*.

4. The genes between pair of parents are exchanged until the *crossover point*, generated by using random number generators for each pair of parents, is reached, the new individuals, called *offspring*, are part of the new population.

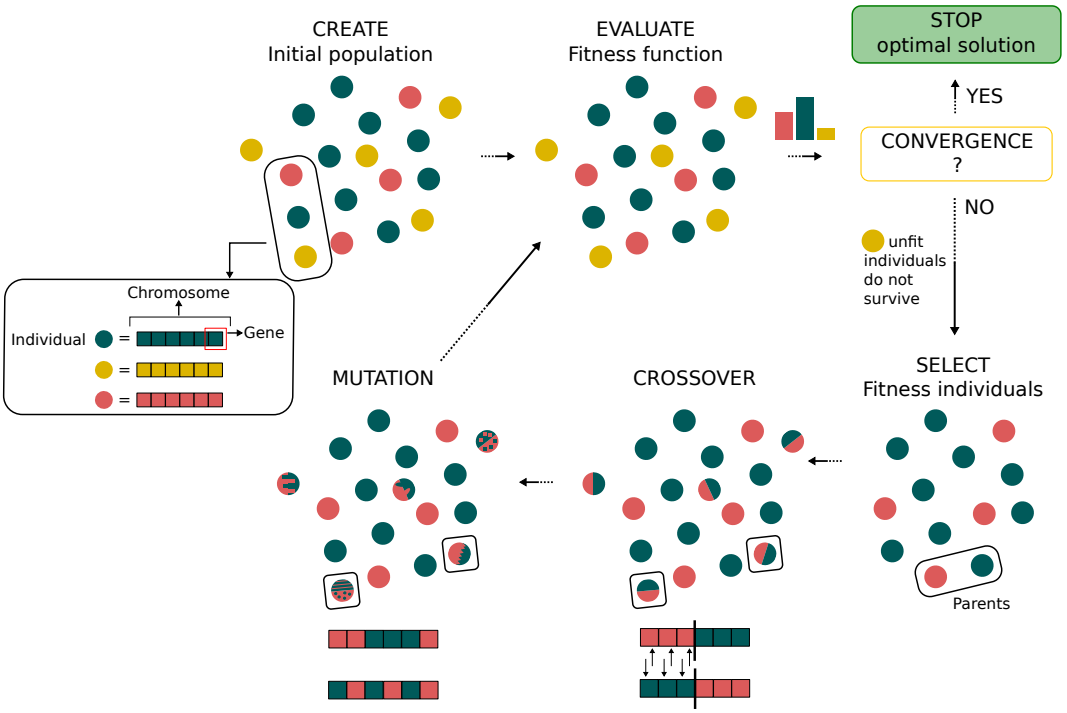

FIGURE 5.3: Population-based algorithm for optimization and terminology.

5. At this stage, the offspring (or just a few of them) might be subjected to a mutation, again by using random probability, to guarantee diversity in the population and avoid early convergence of the algorithm.

6. The optimal solution is reached when the current population at iteration k does not differ significantly from the previous population at iteration $k-1$. The converged population represents a set of the optimal solution for the problem.

The main advantages of the algorithm rely on the ability to seek a global optimum, solve multi-objective problems, and be suitable for parallelization. On the other hand, the main limitation of these methods is the usually much slower convergence with respect to the classical gradient-based methods.

Both these two main categories of optimization methods have been used to perform the study object of this chapter. In the following sections, we will give more details about them, however, for further details about the implemented algorithms, the reader is referred to the MatLab documentation about the gradient-based `https://www.mathworks.com/help/optim/ug/fmincon.html` and genetic algorithm `https://www.mathworks.com/help/gads/genetic-algorithm.html`.

5.2 Shape optimization of Design D′

The results reported in this chapter represent a modified version of the publication [61][1].

[1] *A.Mocci,P.Gupta, and I.Arias. Shape optimization of architected dielectrics with effective piezoelectricity using computational homogenization.* (In Preparation).

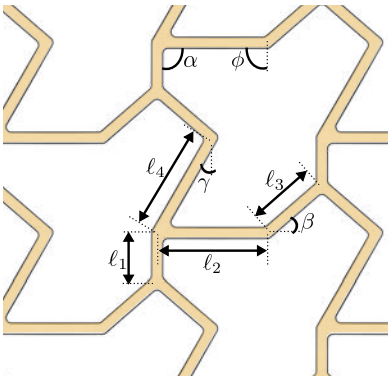

FIGURE 5.4: The geometrical configuration of the most performant lattice design D′ is defined by 8 parameters.

5.2.1 Longitudinal operation mode

In Ch. 3, we concluded that very compliant low-area-fraction lattices are very performant when a pressure is applied ($\bar{g}$) or a displacement is measured ($\bar{d}$), whereas they behave poorly for displacement-sensor ($\bar{h}$) and stress-actuator ($\bar{e}$) mode. In light of that, at a first stage, the fitness functions that we attempted to maximize is represented by the four different effective longitudinal piezoelectric coefficients ($\bar{h}_{22}, \bar{g}_{22}, \bar{d}_{22}, \bar{e}_{22}$), defined in Eq. (3.1) and derived in App. B. Design D′, depicted in Fig. 5.4, is defined by 8 independent geometrical parameters (4 side lengths ℓ_1, ℓ_2, ℓ_3 and ℓ_4 and 4 angles α, β, γ and ϕ) in addition to the thickness of the constituents here fixed to $t = 160$nm, whose effect was extensively discussed in Ch. 3.

Since the number of parameters involved we opted for a genetic-based algorithm, to avoid local minima and seek the global optimal solution. We fixed the population size $P = 48$ and the maximum number of generations $G = 45$, which represents the stopping criterion for our algorithm. The lower l_b and upper u_b bound for each variable (reported in Table 5.1) restrict the dimensional space in which the solution exists, while no further constraints between variables have been enforced.

Design variable	l_b	u_b
ℓ_1[µm]	0.4	4
ℓ_2[µm]	0.1	4
ℓ_3[µm]	0.4	4
ℓ_4[µm]	0.4	1.6
α	50°	90°
β	40°	80°
γ	10°	15°
ϕ	60°	90°

TABLE 5.1: Lower and upper bounds for the 8 design variables selected as minimizers for this problem.

Figure 5.5 shows the results for design D′ in longitudinal displacement $\bar{h}_{22}$ and pressure $\bar{g}_{22}$ sensor operation mode. For each generation we plot the best solution achieved in terms of effective longitudinal piezoelectricity normalized respect to the corresponding reference value for PZT, Fig. 5.5(a,d), while the best set of individuals is shown in Fig. 5.5(b,e). We also

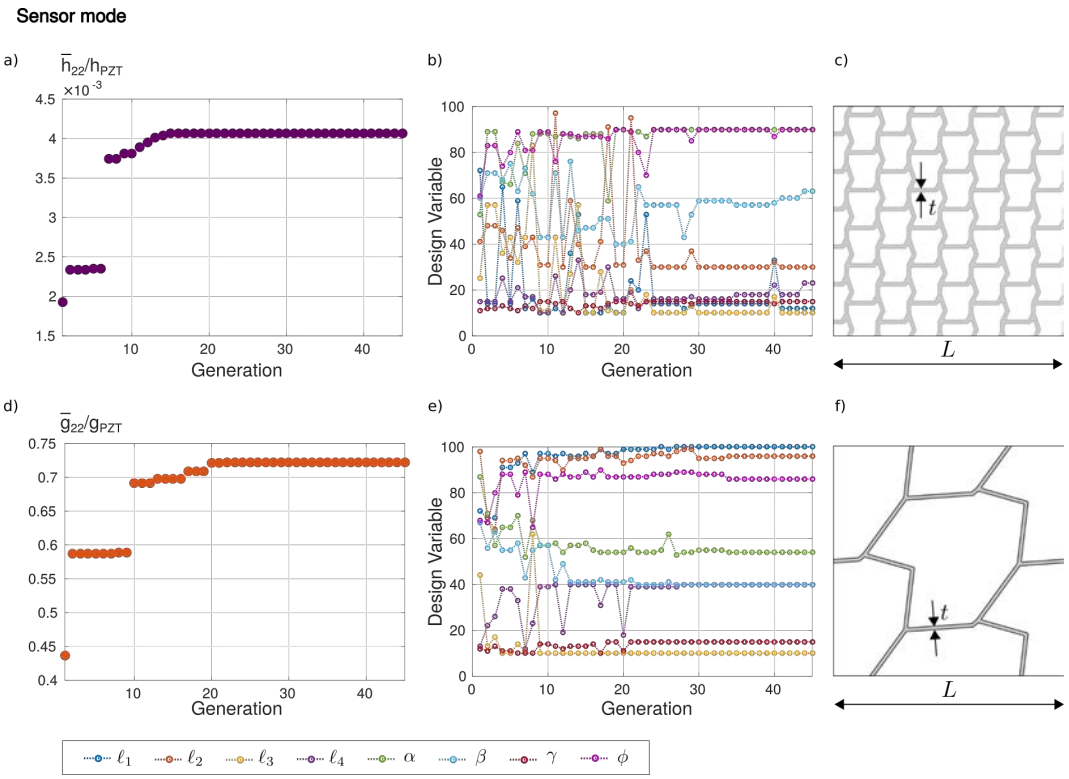

FIGURE 5.5: Shape optimization process for design D′ in longitudinal sensor h_{22} and g_{22} operation mode. A slab of the dimension of $L = 10 \times 10\mu$m have been extracted from our 2D lattice, therefore the resulting optimal shapes are in the same scale and have the same fixed thickness $t = 160$nm.

report the optimal shapes resulting from the optimization process. A slab of the dimension of $L = 10 \times 10\mu$m have been extracted from our 2D lattice, therefore the optimal geometries are in the same scale and have the same fixed thickness $t = 160$nm. As expected and anticipated, the preferred structure in pressure sensor mode is a more compliant lattice, with slender constituents. On the contrary, for $\bar{h}_{22}$ the process converges to a notably stiffer structure, with shorter micro-constituents. The optimization enhanced the performance of our geometries of over 200% on both effective piezoelectricity measurements ($\bar{h}_{22}$ and $\bar{g}_{22}$) in sensor mode.

Figure 5.6 depicts a similar picture. Displacement actuator, quantified by $\bar{d}_{22}$, requires an accommodating lattices, whereas the optimal shape for $\bar{e}_{22}$ is comparable to the displacements-sensor quantified by $\bar{h}_{22}$. For actuator mode, the response of our geometrically polarized structures was increased around 5 times due to the optimization process.

5.2.2 Effect of the nominal material properties on the geometrically polarized lattice

Design D′ besides proving to be the most efficacious lattice also manifests the most enriched behavior in terms of symmetries, Fig. 4.6. Therefore, we will now use it to understand the effect of the nominal material properties on the response of our device.

To untangle the effect of the flexoelectric tensor on our lattice from the other material properties and geometrical parameters we first attempted to maximize the flexoelectric coefficients for a fixed geometrical configuration. Considering a cubic ferroelectric $m3m$, the three flexoelectric coefficients μ_ℓ, μ_t and μ_s were ranged between 0.5 and 1.5μC/m. A gradient-based algorithm was used to perform the analysis. Specifically we make use of

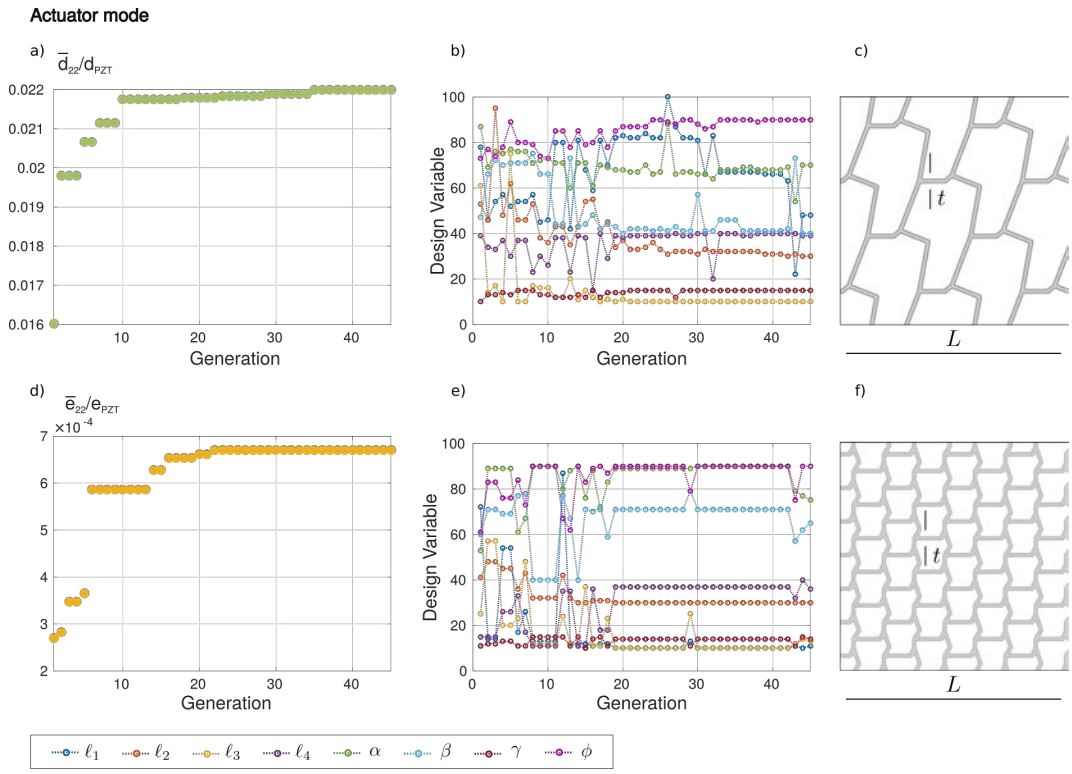

FIGURE 5.6: Shape optimization process for design D′ in longitudinal actuator d_{22} and e_{22} operation mode. A slab of the dimension of $L = 10 \times 10\mu$m have been extracted from our 2D lattice, therefore the resulting optimal shapes are in the same scale and have the same fixed thickness $t = 160$nm.

the sequential quadratic programming (SQP) iterative method [158], which for our unconstrained problem is reduced to the Newton-Raphson method. As stopping criterion we set a tolerance $t = 1e - 8$ for the first-order optimality measure. To ensure that no local minima were found we repeated the analysis considering different set of initial values. The results for the longitudinal strain-actuator quantified by $\bar{d}_{22}$ are shown in Fig. 5.7. The intuition suggests that in bending-dominated structures the transverse coefficient should be responsible for the vast majority of the mobilized flexoelectric effect. However, it is also interesting to notice that shear flexoelectricity is also mobilized in the micro-constituents. Finally, if we consider $\mu_a = \mu_\ell - \mu_t - 2\mu_s$ as a measure of flexoelectric anisotropy, we notice that the optimal effective piezoelectricity is obtained for the more anisotropic flexoelectric tensor.

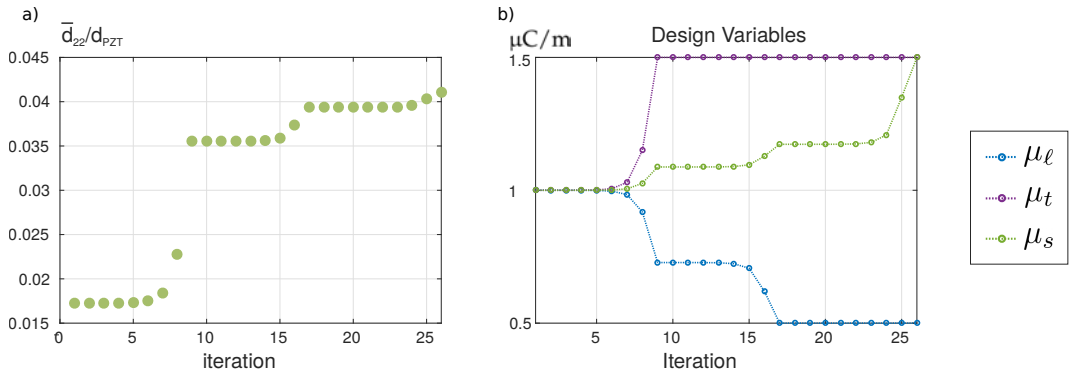

FIGURE 5.7: Cubic flexoelectric tensor

Design variable	l_b	u_b
ℓ_1[μm]	1.2	2.4
ℓ_2[μm]	1.2	2.4
ℓ_3[μm]	1.2	2.4
ℓ_4[μm]	1.2	2.4
α	60°	90°
β	20°	60°
ϕ	60°	90°

TABLE 5.2: Lower and upper bounds for the 7 design variables selected as minimizers for this problem.

Now, we extend our study in order to understand the effect of the nominal Young's modulus Y, varied in a range between 80 and 250GPa, and the dielectric permittivity ϵ ranged from 8 to 140nC/Vm besides the three flexoelectric coefficients μ_ℓ, μ_t and μ_s, ranged between 0.5 and 1.5μC/m. We considered isotropic elasticity and dielectricity whereas for this study we avoided the additional constraint on the symmetry of the flexoelectric tensor. In addition to the aforementioned 5 material properties, we selected 7 geometrical parameters listed in Table 5.2 along with their lower and upper bounds. Figure 5.8 shows the results of the analysis. Since the high number of parameters involved, we used the genetic algorithm, with a population size of $P = 48$ individuals and $G = 45$ as the maximum number of generations which also represents the stopping criterion.

In Fig. 5.8a we report the optimal values of the parameters considered in this problem. Not surprisingly, similarly to the results showed in Fig. 5.5 and Fig. 5.6, slender beams are required for stress-sensors ($\bar{g}_{22}$) and displacement-actuators ($\bar{d}_{22}$) devices for which the beam-length converges to the upper bound thus increasing the compliance of the lattice. On the contrary, our design in displacement-sensor ($\bar{h}_{22}$) and stress-actuator ($\bar{e}_{22}$) mode requires shorter beams, i.e. stiffer micro-structures. The optimal Young's modulus also confirms the same intuition, if on one hand the optimal $\bar{g}_{22}$ and $\bar{d}_{22}$ are satisfied by the lower bound, displacement-sensor almost tends to the upper limit. As regard dielectricity, the lower the dielectric permittivity the more performant the sensors whereas $\bar{e}_{22}$ is maximized for the higher value of ϵ. At last, we analyzed the effect of the longitudinal, transverse, and shear flexoelectric coefficient on the response of our lattice. Again, we noticed that the optimal effective piezoelectricity, irrespective of the quantified piezoelectric coefficient, is obtained for the more anisotropic flexoelectric tensor with the transverse and shear coefficients converging toward the upper limit while the longitudinal tends to the lower bound. Figure 5.8b shows the best solution at each generation for each of the four objective functions normalized respect to the corresponding reference value for PZT. Although a significant increment was observed for all the coefficients, our device demonstrates once more to behave optimally as a sensor under an applied stress reaching performances considerably higher than PZT. Referring to actuator mode, under an applied electric field a fairly good response can be obtained by measuring displacements. On the other hand we conclude that our proposed low-area fraction lattices are ultimately not appropriate for the displacement-based sensor and especially for the stress-actuator setup quantified by $\bar{\mathbf{e}}$, which still produces 3 order of magnitude lower response as compared with piezoelectrics.

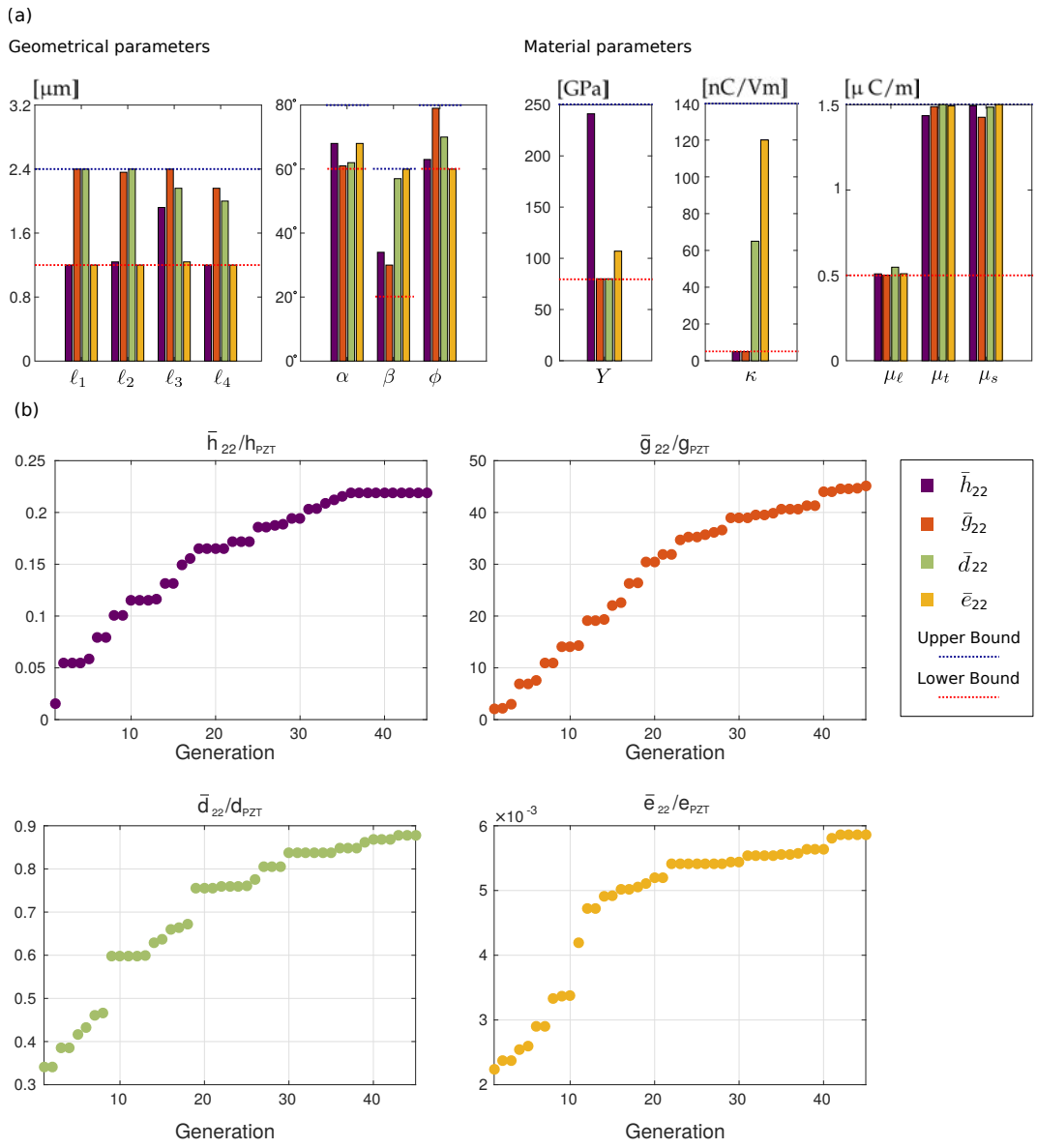

FIGURE 5.8

5.3 On-going work

5.3.1 Transverse and shear operation mode

We have highlighted in Ch. 4 that for some designs, i.e. A, D, and D', the effective longitudinal piezoelectric coefficient was not the most significant, hence motivating the investigation of different operation modes for those devices. Here, making use of the computational homogenization technique discussed in Ch. 4, we attempt to optimize the transverse $\bar{d}_{12}$ and the transverse shear $\bar{d}_{13}$ piezoelectric coefficients. We select 7 design variables as minimizers for the problem on hand, their lower and upper bounds are reported in Table 5.2.

In Fig. 5.9 we show some preliminary results of the optimization process. We limited the population size to $P = 15$ and the maximum number of generations to $G = 16$. Although the response in Fig. 5.9(a,d) might not be converged to the optimal solution, an increased performance can already been appreciated for both operation modes. Figures 5.9(b,c,e,f) show the optimal set of design variables at each generation and the optimal geometrical

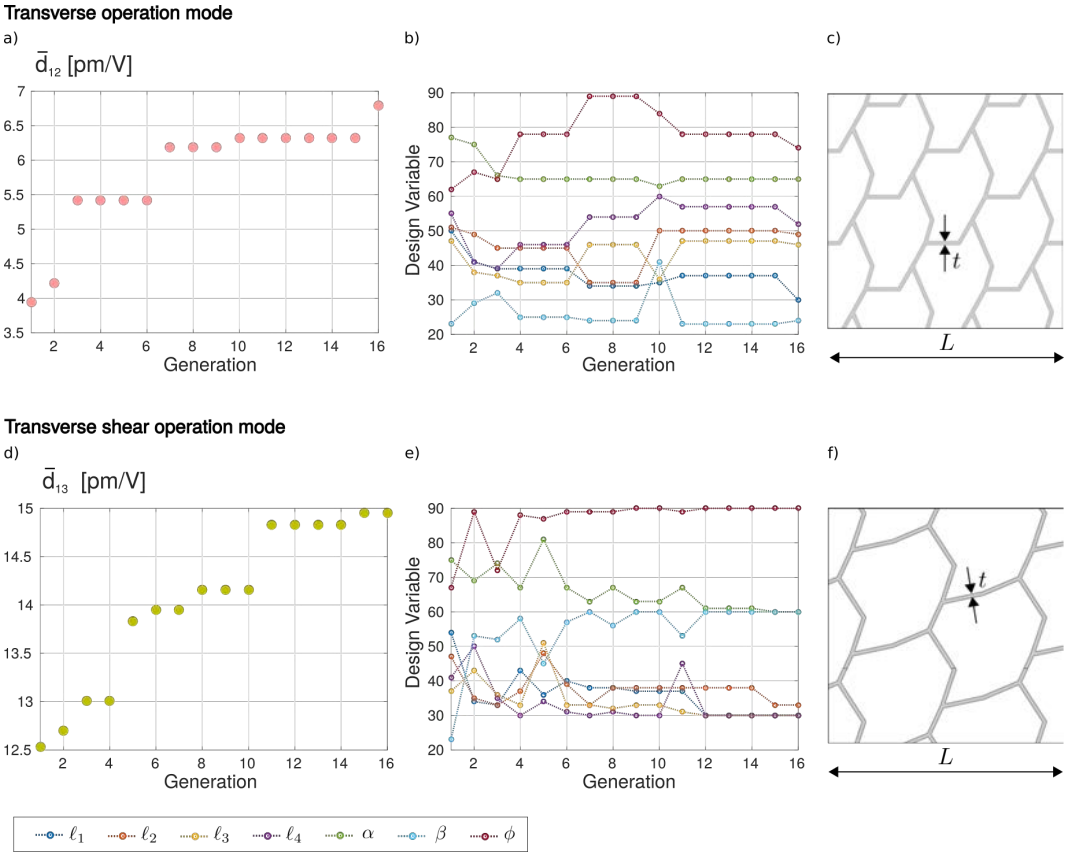

FIGURE 5.9: Shape optimization process for design D′ in transverse d_{122} and shear d_{121} operation mode. A slab of the dimension of $L = 10 \times 10\mu$m have been extracted from our 2D lattice, therefore the resulting optimal shapes are in the same scale and have the same fixed thickness $t = 160$nm.

configuration for transverse and transverse shear mode, respectively.

Chapter 6

Towards 3D flexoelectric metamaterials and devices: flexoelectricity under torsion

In the first part of this manuscript, we focused our attention on the identification of two-dimensional setups with the aim of identifying suitable building blocks for geometrically polarized metamaterials. At this stage, further investigations will be oriented toward the detection of 3D building blocks for metamaterials to enhance the performance of our lattices.

Three-dimensional setups also enable more complex ways of mobilizing gradients, besides bending and compression of non-uniform geometries, torsion is indeed another classical method to induce strong strain gradients [159–161]. Notwithstanding torsion of thin rods has been extensively used to characterize strain-gradient elasticity [162] and plasticity [159, 161] yet surprisingly flexoelectricity has been barely studied in this setting [163, 164] and in particular, to the best of our knowledge there are no studies on torsion of cubic perovskites, which are the strongest flexoelectrics among all dielectrics [27]. The challenging characterization of the flexoelectric tensor is also directly related to torsion. We have seen in Ch. 1 that cantilever beam under bending and truncated pyramid under compression are the most widely used setups to characterized the transverse and longitudinal flexoelectricity, respectively. However, no robust method has been proposed in the literature so far to quantify shear flexoelectricity independently. This is particularly important in non-isotropic cubic ferroelectrics, but also in isotropic systems having only two independent flexoelectric coefficients, since an independent quantification of the third flexoelectric coefficient would reduce the uncertainty of the measurements. Existing techniques use Brillouin scattering data [165], which may contain significant contributions from the dynamic flexoelectric effect [68], or converse flexoelectric measurement in trapezoid samples [166], which may lead to a significant overestimation of flexoelectricity due to the complexity of deformation and electric fields in a trapezoid configuration, particularly around its edges [34]. In most cases, the shear flexoelectric coefficient is either ignored or derived from the transversal and longitudinal ones in isotropic systems [32]. Recently, some efforts have also been made to measure shear flexoelectric coefficients in low-symmetry materials, such as polymers [167, 168] whose symmetry allows a straightforward derivation of the shear flexoelectric coefficients from torsion of cylindrical rods. Building on this, here we argue that quantification of direct shear flexoelectric coefficient in high-symmetry cubic ferroelectrics can be achieved by torsion mechanics but requires complex setups beyond the reach of analytical models.

Here, we propose a comprehensive study of the torsion problem in flexoelectric rods.

To mathematically model the base material within the framework of continuum mechanics [34, 40, 74, 118], we make use of the *direct* form of the enthalpy $\mathcal{H}^{\langle Dir \rangle}$, (Eq. (2.3), sec. 2.2.1), where the contribution of the strain gradient elasticity term **h** was found to be insignificant and hence neglected. To quantify flexoelectricity in cubic rods under torsion, we modeled linear flexoelectricity using the meshfree approach which represents a self-consistent formulation accounting for the two-way electromechanical coupling between polarization and strain gradient, and conversely between polarization gradient and strain.

Before turning to our self-consistent computations and discuss the merits of the problem, it is instructive to approximate the flexoelectric response to torsion considering only the one-way coupling from strain gradient to polarization and not the converse effect. In Sec. 6.1 we will resume the torsion problem for the linear elastic regime. In the following Sec. 6.3 we will also propose a novel setup to quantify the shear flexoelectric coefficient exploiting torsion mechanics.

6.1 Torsion of a conical shaft with general cross section

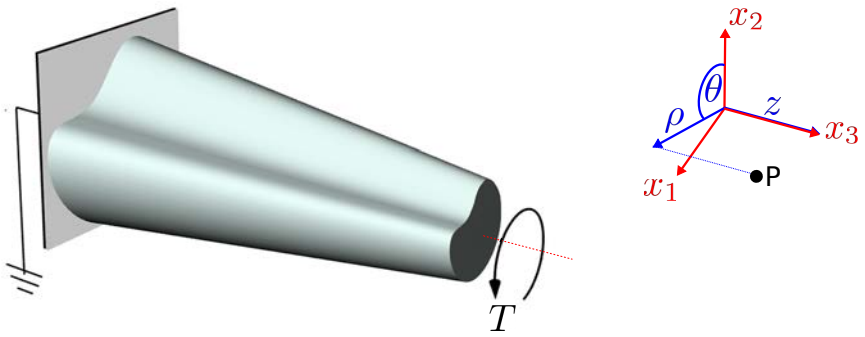

FIGURE 6.1: Prismatic shaft under an applied constant torque T. The Cartesian $(Ox_1x_2x_3)$ and the cylindrical $(O\rho\theta z)$ reference systems are also reported.

The polarization induced by the strain-gradients can be mathematically expressed as

$$P_i = \mu_{ijkl}\varepsilon_{jk,l}, \tag{6.1}$$

where **P** is the polarization, $\boldsymbol{\varepsilon}$ is the mechanical strain, $_{,l}$ denotes partial differentiation with respect to the $l-$th coordinate and $\boldsymbol{\mu}$ is the fourth-order flexoelectric tensor. Figure 6.1 sketched a prismatic shaft having a generic cross section varying along the longitudinal direction under an applied constant torque T, the Cartesian and cylindrical reference systems are also shown. The corresponding displacement field $\mathbf{u}(T)$ is stated from classical elasticity following the De Saint Venant torsion theory [169] in both Cartesian and cylindrical coordinates, as:

$$\begin{cases} u_1 = -\alpha(x_3)x_2x_3, \\ u_2 = \alpha(x_3)x_1x_3, \\ u_3 = \alpha(x_3)\psi(x_1,x_2), \end{cases} \qquad \begin{cases} u_\rho = 0, \\ u_\theta = \alpha(z)\rho z, \\ u_z = \alpha(z)\psi(\rho,\theta), \end{cases} \tag{6.2}$$

Cartesian coordinates Cylindrical coordinates

where ψ is an harmonic function $(\nabla^2\psi = 0)$ called *warping* characterizing the uniform deformation out of plane of the cross-section, which is zero for circular cross sections. The applied torque T twists the rod by an angle $\phi(z)$ whose rate-of-change along the z-axis is the *twist rate* $\alpha(z) = d\phi/dz = T/GJ(z)$, being G the shear modulus and $J(z)$ the polar moment of inertia of the cross-section about the torque axis [169, 170]. By deriving Eqs. (6.2), the non-vanishing strain gradient components in Cartesian coordinates are

$$\varepsilon_{33,1} = \alpha'(x_3)\frac{\partial\psi(x_1,x_2)}{\partial x_1}, \tag{6.3a}$$

$$\varepsilon_{33,2} = \alpha'(x_3)\frac{\partial\psi(x_1,x_2)}{\partial x_2}, \tag{6.3b}$$

$$\varepsilon_{33,3} = \alpha''(x_3)\psi(x_1,x_2), \tag{6.3c}$$

$$2\varepsilon_{13,1} = \alpha(x_3)\frac{\partial^2\psi(x_1,x_2)}{\partial x_1^2}, \tag{6.3d}$$

$$2\varepsilon_{13,2} = \alpha(x_3)\frac{\partial^2\psi(x_1,x_2)}{\partial x_1\partial x_2} - \alpha'(x_3)x_3 - \alpha(x_3), \tag{6.3e}$$

$$2\varepsilon_{13,3} = \alpha'(x_3)\frac{\partial\psi(x_1,x_2)}{\partial x_1} - 2\alpha'(x_3)x_2 - \alpha''(x_3)x_2x_3, \tag{6.3f}$$

$$2\varepsilon_{23,1} = \alpha(x_3)\frac{\partial^2\psi(x_1,x_2)}{\partial x_1\partial x_2} + \alpha'(x_3)x_3 + \alpha(x_3), \tag{6.3g}$$

$$2\varepsilon_{23,2} = \alpha(x_3)\frac{\partial^2\psi(x_1,x_2)}{\partial x_2^2}, \tag{6.3h}$$

$$2\varepsilon_{23,3} = \alpha'(x_3)\frac{\partial\psi(x_1,x_2)}{\partial x_2} + 2\alpha'(x_3)x_1 + \alpha''(x_3)x_1x_3, \tag{6.3i}$$

where

$$\alpha' = \frac{d\alpha(x_3)}{dx_3} \quad \text{and} \quad \alpha'' = \frac{d^2\alpha(x_3)}{dx_3^2}.$$

The derivation of the strain gradient components in cylindrical coordinates is reported in App. C. In the case of cubic flexoelectricity (C.4), aligned with the rod longitudinal axis x_3, the resulting polarization components can be written as

$$\begin{aligned}
P_1 =& \mu_\ell\varepsilon_{11,1} + \mu_t(\varepsilon_{22,1} + \varepsilon_{33,1}) + 2\mu_s\left(\varepsilon_{12,2} + \varepsilon_{13,3}\right) = (\mu_t + \mu_s)\alpha'\frac{\partial\psi}{\partial x_1} + \mu_s\left(-2\alpha' x_2 - \alpha'' x_2 x_3\right),\\
P_2 =& \mu_\ell\varepsilon_{22,2} + \mu_t(\varepsilon_{11,2} + \varepsilon_{33,2}) + 2\mu_s\left(\varepsilon_{21,1} + \varepsilon_{23,3}\right) = (\mu_t + \mu_s)\alpha'\frac{\partial\psi}{\partial x_2} + \mu_s\left(2\alpha' x_1 + \alpha'' x_1 x_3\right),\\
P_3 =& \mu_\ell\varepsilon_{33,3} + \mu_t(\varepsilon_{11,3} + \varepsilon_{22,3}) + 2\mu_s\left(\varepsilon_{13,1} + \varepsilon_{23,2}\right) = \mu_\ell\alpha''\psi.
\end{aligned} \tag{6.4}$$

Eqs. (6.4) suggest that in principal a certain non-zero polarization might be achieved in cubic flexoelectric rods under torsion. In the following sections, we will consider and analyze different geometrical setups under torsion and numerically support these claims.

6.2 Self consistent quantification of flexoelectric roads under torsion

The probably most ordinary geometry to be considered is a road having circular cross-section, like the one depicted in Fig. 6.2. Symmetry considerations imply that cross-sections do not warp, i.e. remaining planar after deformation, and the rate of twist α also remains

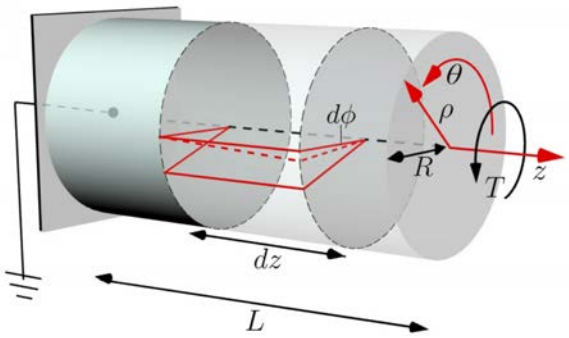

FIGURE 6.2: Twisting of a bar under an applied torque T around the z-axis. The infinitesimal angle $d\phi$ is the angle of torsion between a pair of cross-sections with the infinitesimal distance dz apart. Cylindrical (ρ, θ, z) coordinate system is depicted.

constant. Thus, being $\psi(\rho, \theta) = 0$ and $\alpha', \alpha'' = 0$, the simplified analysis in Eqs. (6.4) suggests that torsion of cylindrical rods of general cross-section should not result in flexoelectric polarization for materials with cubic symmetry.

To test these predictions coming from a simplified one-way coupled model, we assume that the symmetry of the flexoelectric tensor is aligned with the z-axis (bar axis), and pure torsion is applied, as depicted in Fig. 6.2. The central point of the left-end cross-section is electrically grounded, and all other boundaries are free of surface charges. The material constants were chosen to fit the behavior of a strongly flexoelectric material, Barium Strontium Titanate (BST) in its paraelectric phase, assuming isotropic elastic and electrical properties. Details about the key material parameters are reported in table 6.1. First, the flexoelectric coefficients were assumed to follow the relationship $\mu_t = \mu_\ell = \mu_s$, resulting in an anisotropic flexoelectric tensor. To avoid rigid body motions mechanical displacements ($u_i = 0$, for $i = 1, 2, 3$) and electric potential ($\phi = 0$) have been fixed at $z = 0$. The torque is prescribed by setting the displacement field as stated in Eqs.(6.2), where the twist rate was set as $\alpha = 0.05$. Our calculations, in agreement with the simplified theoretical prediction, confirmed that no flexoelectric polarization is induced by the torsion of a cylindrical rod, irrespective of whether the cross-section is circular or not, Fig. 6.3(a,b).

TABLE 6.1: Barium Strontium Titanate (BST). Material parameters.

E [GPa]	ν	κ [nC/Vm]	μ_ℓ, μ_t, μ_s [μ C/m]
152	0.33	141.6	121

The previous rationale suggested that in principle a flexoelectric polarization could be generated by creating a longitudinal gradient of the torsion strains. One way to achieve this is through a longitudinal variation of the geometry, we considered for instance a truncated conical rod under torsion, see Fig. 6.4, for which the flexoelectric polarization can be approximated (considering only the direct coupling) as

$$\begin{aligned} P_\rho &= 0, \\ P_\theta &= \mu_s \left(2\rho\alpha' + \rho z \alpha''\right), \\ P_z &= 0. \end{aligned} \tag{6.5}$$

Our self-consistent simulations indeed confirmed the generation of a non-uniform electric

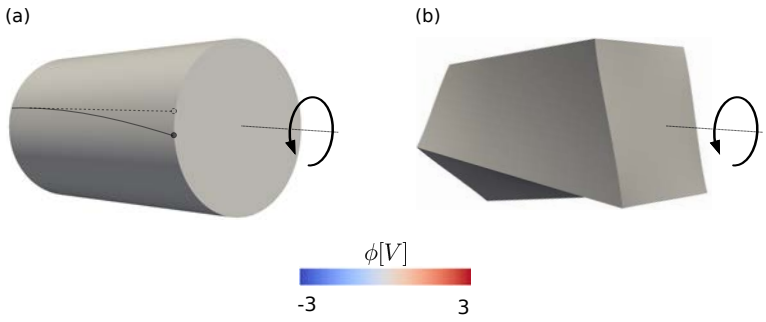

FIGURE 6.3: Electric potential distribution in (a) circular cross-section and (b) square cross-section. Electric potential is not generated in these setups.For visualization purposes, deformations are amplified by a factor of 30.

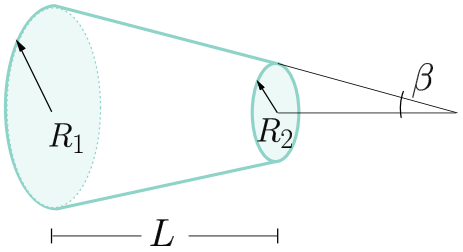

FIGURE 6.4: Cone geometrical parameters, R_1, R_2 and L.

potential ϕ in the cross-section. Remarkably, our simulations predicted the appearance of a characteristic pattern in the electric potential distribution, Fig. 6.5(a), exhibiting symmetry upon 90° rotations. This symmetry was also present in all contributions to the electric displacement $\mathbf{D} = \boldsymbol{\mu} : \nabla\boldsymbol{\varepsilon} - \kappa\nabla\phi$. In Fig. 6.6 we decomposed the angular $(\boldsymbol{\mu} : \nabla\boldsymbol{\varepsilon})_\theta = \boldsymbol{\mu} : \nabla\boldsymbol{\varepsilon} - \boldsymbol{\mu} : \nabla\boldsymbol{\varepsilon} \cdot \mathbf{n}$ and radial $(\boldsymbol{\mu} : \nabla\boldsymbol{\varepsilon})_\rho = \boldsymbol{\mu} : \nabla\boldsymbol{\varepsilon} \cdot \mathbf{n}$ components,with $\mathbf{n}$ being the outward unit normal to the circular cross-section.

To test whether the appearance of non-ferroelectric polarization domains was specific to torsion, we subjected the same conical rod to compression and bending, Fig. 6.7(a,b). As expected from previous works [16, 34, 35, 40, 73, 124], these two loading conditions led to the emergence of strain gradients and flexoelectric polarization but did not induce polarization domains.

Given the fact that in these simulations geometry, boundary conditions and isotropic

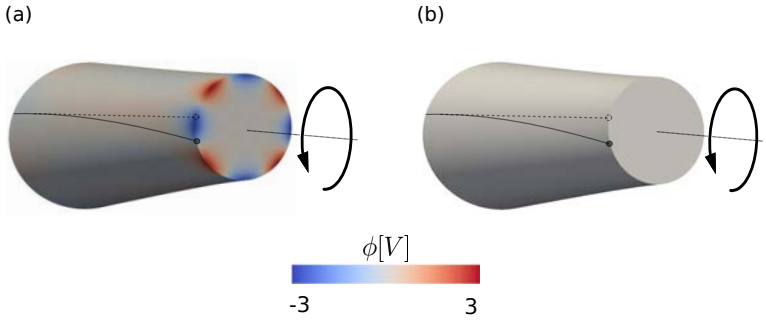

FIGURE 6.5: Distribution of electric potential for (a) anisotropic flexoelectricity and (b) isotropic flexoelectricity. A non-ferroelectric electric potential pattern is observed for the case of anisotropic flexoelectricity only. Isotropic elastic properties and circular cross-section are considered to isolate flexoelectric anisotropy from other sources of material or geometrical anisotropy.For visualization purposes, deformations are amplified by a factor of 30.

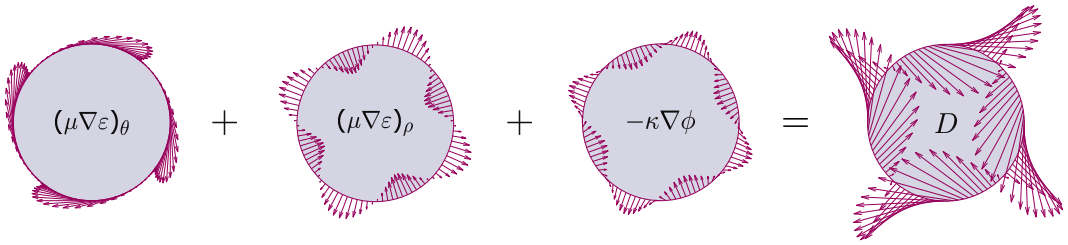

FIGURE 6.6: Vector plot of the electric displacement $\mathbf{D} = \boldsymbol{\mu}\nabla\boldsymbol{\varepsilon} - \kappa\nabla\phi$ along a circle on the cross-section not located on the lateral surface of the cone. Both individual contributions to $\mathbf{D}$ are shown, the first one is decomposed into the angular and radial components, $(\boldsymbol{\mu}\nabla\boldsymbol{\varepsilon})_\theta = \boldsymbol{\mu}\nabla\boldsymbol{\varepsilon} - \boldsymbol{\mu}\nabla\boldsymbol{\varepsilon}\cdot\mathbf{n}$ and $(\boldsymbol{\mu}\nabla\boldsymbol{\varepsilon})_\rho = \boldsymbol{\mu}\nabla\boldsymbol{\varepsilon}\cdot\mathbf{n}$, $\mathbf{n}$ being the outward unit normal to the circular cross-section.

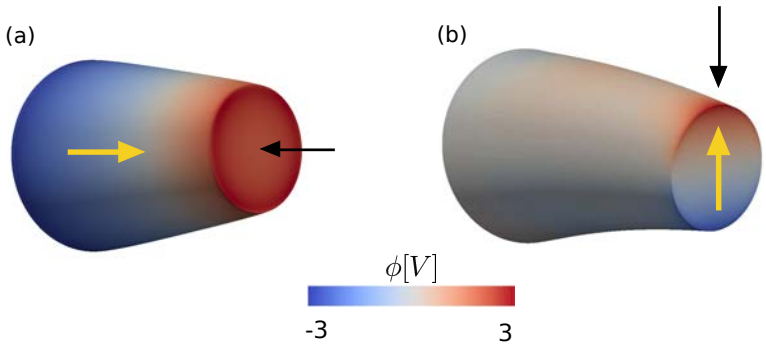

FIGURE 6.7: Distribution of electric potential in a truncated cone under (g) compression and (h) bending. The yellow arrows represent the polarization direction. The applied displacements are represented by the black arrows. For visualization purposes, deformations are amplified by a factor of 30.

elasticity are all axisymmetric with respect to the rod axis, we reasoned that flexoelectric anisotropy should be responsible for the observed polarization domain micro-structure. Consequently, no flexoelectrically induced polarization domains should be expected if the material were flexoelectrically isotropic. To test this hypothesis, we simulated the response of a truncated conical rod with the same geometry subjected to the same torsional load but we considered an isotropic flexoelectric material, i.e. $2\mu_s = \mu_\ell - \mu_t$ [31]. As shown in Fig. 6.5(b), no polarization patterns are observed in the isotropic case, confirming that flexoelectric anisotropy is the mechanism behind the generation of the non-ferroelectric polarization pattern.

To further pinpoint the origin of the observed flexoelectrically-induced radial polarization patterns, we studied the symmetries of the flexoelectric tensor. Consider a rotation of the flexoelectric tensor μ given by

$$\mu_{i'j'k'l'} = a_i^{i'} a_j^{j'} a_k^{k'} a_l^{l'} \mu_{ijkl}, \tag{6.6}$$

where $a_i^{i'}$ are the coefficients of the rotation matrix R. For a rotation of angle θ around the z axis we have

$$R(\theta) = \begin{bmatrix} m & -n & 0 \\ n & m & 0 \\ 0 & 0 & 1 \end{bmatrix},$$

where $m = \cos\theta$ and $n = \sin\theta$. In an isotropic flexoelectric medium, the rotated flexoelectric tensor μ' should not depend on the rotation angle θ, i.e. $\mu' = \mu$. In general, this condition will

only hold for specific angles characterizing the flexoelectric material symmetry. Enforcing this condition in Eq. (6.6) results in the following two equations:

$$2m^2n^2(\mu_\ell - \mu_t - 2\mu_s) = 0, \tag{6.7}$$

$$(mn^3 - m^3n)(\mu_\ell - \mu_t - 2\mu_s) = 0. \tag{6.8}$$

Eqs. (6.7) and (6.8) are satisfied for any value of θ if the following relation holds

$$\mu_s = \frac{\mu_\ell - \mu_t}{2}. \tag{6.9}$$

As shown in Fig. 6.5(b), in this case where geometry and all material parameters are axisymmetric, all fields are also axisymmetric and hence polarization domains are not possible.

In the case of anisotropic cubic flexoelectricity, i.e. if Eq. (6.9) does not hold, Eqs. (6.7) and (6.8) are satisfied only at certain angles $k\pi/2$ and $k\pi/4$, $k \in \mathbb{Z}$, respectively. Consequently, the solution of the flexoelectric problem, including electric potential, flexoelectric polarization, and electric displacement, should be symmetric under the action of the rotation group $G_1 = \{R(k\pi/2), k \in Z\}$ in agreement with our results, see Fig. 6.5(a) and Fig. 6.6. Furthermore, our simulations consistently showed that the electric potential ϕ, the dielectric polarization $-\kappa\nabla\phi$, and the radial component of the flexoelectric polarization $(\boldsymbol{\mu} \vdots \nabla\boldsymbol{\varepsilon})_\rho$ are antisymmetric under the action of $G_2 = \{R((2k+1)\pi/4), k \in Z\}$, i.e. rotations by multiples of $\pi/4$ that are not multiples of $\pi/2$. The fact that not all the contributions to the electric displacement were exhibiting this antisymmetry, suggested that this antisymmetry should not be present in the flexoelectric tensor μ. Indeed, we confirmed that $\mu' \neq -\mu$ under the action of G_2. However, we found that some of the components of the flexoelectric tensor changed sign under G_2. For a flexoelectric tensor $\boldsymbol{\mu}'$ rotated an angle θ with respect to the Cartesian coordinate axis, the matrix in Voigt notation (C.4) can be rewritten as

$$[\mu']^T = \begin{bmatrix}
\mu_1 + \frac{\mu_a \cos 4\theta}{4} & -\frac{\mu_a \sin 4\theta}{4} & 0 \\
-\frac{\mu_a \sin 4\theta}{4} & \mu_2 - \frac{\mu_a \cos 4\theta}{4} & 0 \\
0 & 0 & \mu_2 - \frac{\mu_a}{4} \\
\mu_2 - \frac{\mu_a \cos 4\theta}{4} & \frac{\mu_a \sin 4\theta}{4} & 0 \\
\frac{\mu_a \sin 4\theta}{4} & \mu_1 + \frac{\mu_a \cos 4\theta}{4} & 0 \\
0 & 0 & \mu_2 - \frac{\mu_a}{4} \\
\mu_2 - \frac{\mu_a}{4} & 0 & 0 \\
0 & \mu_2 - \frac{\mu_a}{4} & 0 \\
0 & 0 & \mu_1 + \frac{\mu_a}{4} \\
-\frac{\mu_a \sin 4\theta}{4} & \frac{2\mu_1 - 2\mu_2 - \mu_a \cos 4\theta}{4} & 0 \\
\frac{2\mu_1 - 2\mu_2 - \mu_a \cos 4\theta}{4} & \frac{\mu_a \sin 4\theta}{4} & 0 \\
0 & 0 & 0 \\
0 & 0 & \frac{2\mu_1 - 2\mu_2 - \mu_a}{4} \\
0 & 0 & 0 \\
\frac{2\mu_1 - 2\mu_2 - \mu_a}{4} & 0 & 0 \\
0 & 0 & 0 \\
0 & 0 & \frac{2\mu_1 - 2\mu_2 - \mu_a}{4} \\
0 & \frac{2\mu_1 - 2\mu_2 - \mu_a}{4} & 0
\end{bmatrix}, \tag{6.10}$$

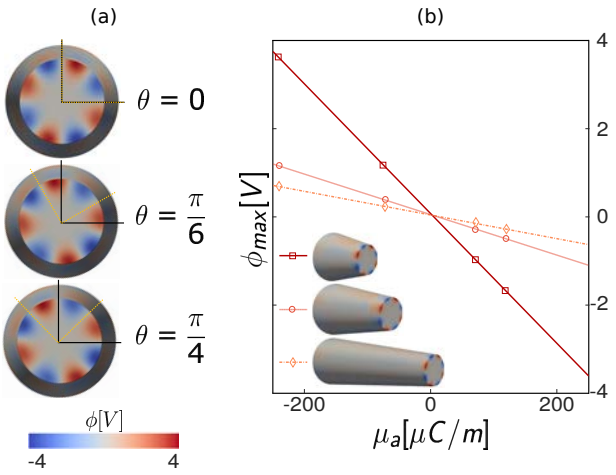

FIGURE 6.8: (a) Distribution of electric potential in three different simulations with flexoelectric tensors rotated different angles $\theta = 0, \pi/6$ and $\pi/4$, respectively. (b) Maximum magnitude of electric potential as a function of the flexoelectric anisotropy parameter for different geometrical configurations.

where the three independent components have been taken as

$$\mu_1 = \frac{3}{4}\mu_\ell + \frac{1}{4}\mu_t + \frac{1}{2}\mu_s \tag{6.11a}$$

$$\mu_2 = \frac{1}{4}\mu_\ell + \frac{3}{4}\mu_t - \frac{1}{2}\mu_s \tag{6.11b}$$

$$\mu_a = \mu_\ell - \mu_t - 2\mu_s. \tag{6.11c}$$

The new components ($\mu_{ijjj} = \mu_{iiij}$) arising upon rotation depend on the flexoelectric anisotropy parameter μ_a and exhibit the antisymmetry under the action of $G_2 = \{R((2k+1)\pi/4), k \in Z\}$ also observed in the electric potential and the radial flexoelectric polarization domain patterns. We defined the flexoelectric anisotropy parameter μ_a, which is the common factor in Eqs. (6.7) and (6.8). These sign changes thus explained the existence of patterns but did not explain the antisymmetry with respect to G_2, suggesting that the latter was the result of the flexoelectric boundary value problem as a whole. To further support these observations, we ran simulations with different rotated flexoelectric tensors μ' to verify the dependence of the pattern on the crystallographic orientation. The simulation results show that the domain patterns follow the rotation of the flexoelectric tensor, see Fig. 6.8(a).

To investigate the effect of the flexoelectric material parameters on the domain patterns, we performed a set of simulations with different combinations of the flexoelectric coefficients μ_ℓ, μ_t, and μ_s, for three different cone geometries. As we have seen, $\mu_a = 0$ corresponds to isotropic flexoelectricity, and hence μ_a is a measure of flexoelectric anisotropy. Our results showed that the maximum magnitude of the electric potential at the end surface of the rod ($z = L$) depends only on the flexoelectric anisotropy parameter μ_a and not on the specific values of μ_ℓ, μ_t, and μ_s. Furthermore, we found this dependence to be linear, with a linear coefficient depending on the cone geometry, Fig. 6.8(b).

To further examine the effect of geometry on the torsional response of truncated conical rods, we performed a set of simulations with different conical geometries. Three independent geometrical parameters are required to describe the conical rod, namely, the truncated cone length L, and the end cross-section radii, R_1 and R_2, as shown in Fig. 6.4. We kept the radius $R_1 = 24$ mm to fix the scale for all simulations, and studied the dependence of

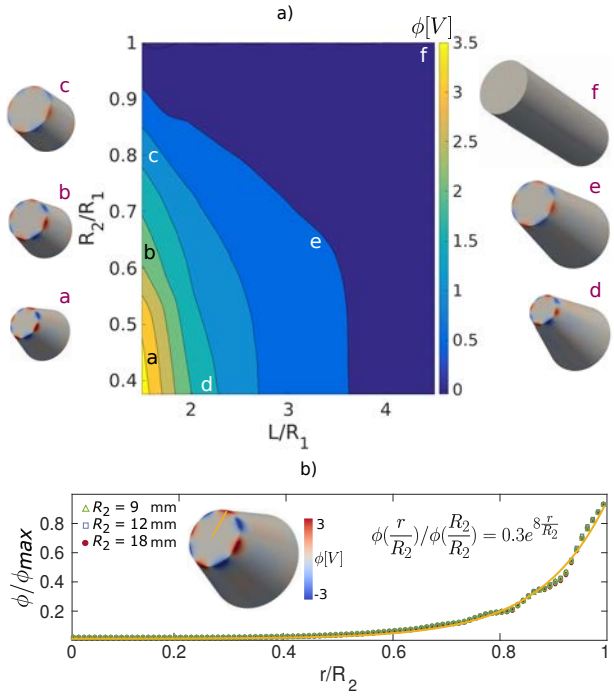

FIGURE 6.9: (a) Contour plots of maximum magnitude of electric potential on the surface at the end cross-section as a function of R_2/R_1 and L/R_1, with $R_1 = 24$ mm. (b) Electric potential profile on a cross-section along the radial direction for three different cones geometries (all with $R_1 = 24$ mm and $L = 48$ mm).

the maximum electric potential on the other two remaining parameters, R_2 and L. Figure 6.9(a) shows the maximum value of the electric potential for different geometrical configurations as a function of the length L and the smaller radius R_2, both normalized by R_1. For smaller R_2/R_1 and $L/R_1 \simeq 1$ we achieve the maximum electric potential on the lateral surface, whereas vanishing electric potential is obtained for geometries approaching the cylinder ($R_2/R_1 = 1$ or $L/R_1 >> 1$) as expected, Fig. 6.3. From this figure it becomes apparent that the sharper and shorter the cone, the larger the maximum electric potential. Figure 6.9(b) shows the electric potential profile on a cross-section along the radial direction for three different cone geometries, which we found to follow the exponential function $\phi(r/R_2)/\phi(R_2/R_2) = 0.3\, e^{8\frac{r}{R_2}}$ in all cases studied (only three are shown here).

The results presented in this section have been extrapolated and modified from [62][1].

6.3 Chasing the elusive shear flexoelectricity

If on one hand, we have shown that truncated conical rods can cause a net non-zero polarization, on the other side the observed patterns are still difficult to be handled in practical applications and particularly as a means for independent quantification of the shear flexoelectric coefficient.

According to the simplified derivation showed in the previous section, the flexoelectrically-induced polarization is related with the shear flexoelectric coefficient μ_s in cubic flexoelectrics,

[1] *A.Mocci, A.Abdollahi, and I.Arias. Flexoelectricity in dielectrics under torsion.* (To be submitted).

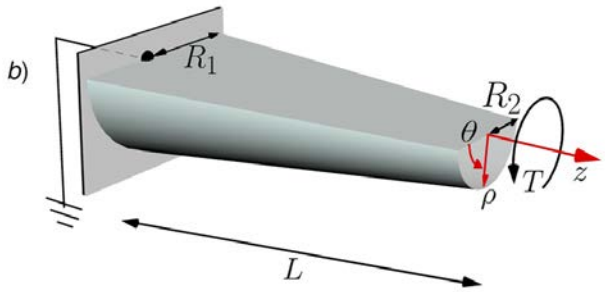

FIGURE 6.10: Truncated cone having radius R_1, R_2, respectively and length L. A ground electrode is placed on the clamped end of the shaft while a torque T is applied on the free-end.

cf. Eq. (6.5). Torsion of conical rods can thus be used as a means for independent quantification of this elusive coefficient. In order to do this, we need to establish a simple relationship between the flexoelectrically-induced polarization P_θ and the experimentally measured electric potential. However, in a flexoelectric material the polarization is related through the electric displacement as

$$D_i = -\kappa\phi_{,i} + \mu_{ijkl}\varepsilon_{jk,l}, \tag{6.12}$$

where κ is the dielectric constant. In a truncated conical rod, cf. Fig. 6.4, this relation cannot be easily established and thus it is not suitable for quantification purposes. The angular polarization P_θ cannot be easily computed from surface measurements of ϕ. Due to the rotational symmetry of the cross-section, D_θ is indeed free to take any value, complicating the quantification of P_θ from the electric potential.

On the contrary, on a half truncated cone, free of surface charges, cf. Fig. 6.11, the angular electric displacement D_θ vanishes on the surface, and thus the angular polarization can be estimated as

$$P_\theta(\rho, z) = \kappa\nabla_\theta\phi \approx \kappa\frac{\phi(\rho, 0, z) - \phi(\rho, \pi, z)}{\pi\rho}, \tag{6.13}$$

where the electric potential ϕ is obtained from the simulation results.

On the other hand, considering Eqs. (6.3), the resulting one-way coupled polarization is

$$P_\rho = (\mu_t + \mu_s)\,\alpha'\frac{\partial\psi}{\partial\rho}, \tag{6.14a}$$

$$P_\theta = (\mu_t + \mu_s)\,\alpha'\frac{1}{\rho}\frac{\partial\psi}{\partial\theta} + \mu_s\left(\alpha''z\rho + 2\alpha'\rho\right), \tag{6.14b}$$

$$P_z = \mu_\ell\alpha''\psi + \mu_s\alpha\nabla^2\psi, \tag{6.14c}$$

from which, an analytical approximation of the angular polarization P_θ can be obtained as

$$P_\theta^a(\rho, z) = \frac{4\mu_s T}{GJ_s(z)\,R(z)}\left(\frac{R_1 - R_2}{L}\right)\rho, \tag{6.15}$$

where R_1 and R_2 are the radii of the fixed- and free-end cross-sections of the bar, respectively, L represents the length of the beam, see Fig. 6.10, $J_s(z)$ is the polar moment of inertia of the semi-circular cross-section about the torque axis, and $R(z)$ is the cross-section radius, which we assume to vary linearly, i.e. $R(z) = (R_2 - R_1)z/L + R_1$. The analytical estimation of the angular polarization in Eq. (6.15) bring along with two main simplifying assumptions. First,

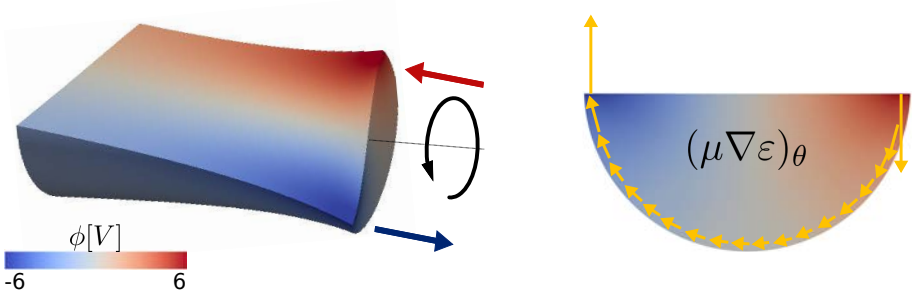

FIGURE 6.11: Distribution of the electric potential ϕ in a half truncated cone where a constant torque is applied on the right-end while the displacement and electric potential are fixed on the left end. A well-defined distribution of the electric potential is observed. An angular polarization (yellow arrow) can be obtained from the induced electric potential due to the disappearance of the angular dielectric displacement $\mathbf{D}_\theta$ over the flat surface. The distribution of the out-of-plane displacement u_z, due to the warping of the cross-section, in a deformed configuration of the half truncated cone, is also shown. The arrows represent the warping direction. The deformation is exaggerated by a factor of 20 for clarity.

strain gradients in Eqs. (6.3) are computed from mechanics alone and then used to compute the flexoelectric polarization in Eq. (6.5), thereby neglecting the two-way coupling and thus the converse effect. These fields are thus not a self-consistent solution of the flexoelectric boundary value problem, while analytical solutions of the full flexoelectric boundary value problems are attainable only in very simple settings [55, 71, 118, 171–173]. Second, Eq. (6.15) has been obtained for a circular cross-section and thus assumes zero warping. For a general cross-section, Eq. (6.15) neglects the first term in Eq. (6.14), as well as the radial and the longitudinal polarization components, P_ρ and P_z in Eqs. (6.14a) and (6.14c), respectively. All these contributions depend not only on the shear flexoelectric coefficient μ_s, but also on the other flexoelectric coefficients as well. In particular, the neglected term in Eq. (6.14b) depends also on the transversal flexoelectric coefficient μ_t, and thus prevents an independent quantification of μ_s. For a semi-circular cross-section, significant warping of the cross-section occurs, as shown in Fig. 6.11, which induces non-zero radial and longitudinal polarization components, cf. Eqs. (6.14).

Deriving analytical expressions for the warping functions in general cross-sections is challenging and has been achieved only for a few geometries, such as elliptic and hyperbolic cross-sections [174]. Thus, to improve the precision of the quantification of the elusive shear flexoelectric coefficient μ_s, we use computational simulations to derive corrections for the analytical estimate in Eq. (6.15) accounting for (1) the effect of the two-way flexoelectric coupling, (2) the warping of the cross-section, and (3) the effect of the longitudinal and transversal flexoelectric components.

We first target the first two sources of deviation by comparing the analytical estimate with the self-consistent computational solution of the flexoelectric boundary value problem with $\mu_s = 121$ µC/m and $\mu_\ell = \mu_t = 0$. Figure 6.12 shows the longitudinal variation along the half-truncated cone of the cross-section simulated polarization P_θ and the analytically approximated polarization, P_θ^a, as computed with Eq. (6.15). Both the analytically estimated and the simulated polarization exhibit the same trend, however, the analytical approximation overestimates the polarization magnitude by over two times. As the analytical estimate is not the self-consistent solution of the flexoelectric boundary value problem, it does not satisfy the charge-free electrical boundary condition, cf. Fig. 6.12(a), where we plot

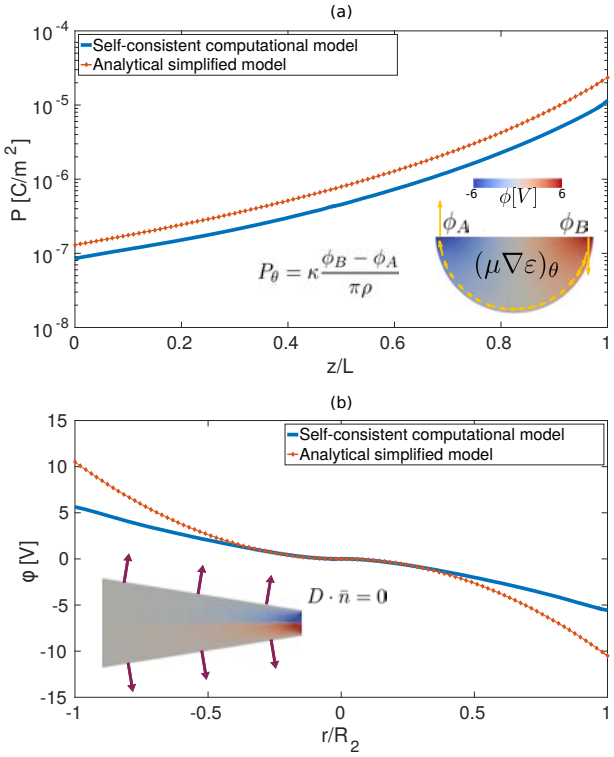

FIGURE 6.12: (a) Polarization P_θ as a function of the z coordinate obtained from the simplified analytical model and three-dimensional self-consistent simulation results. The inset shows the simulation result for the electric potential distribution in a semi-circular cross-section of the bar. The yellow arrows represent the angular polarization P_θ calculated from the electric potential values ϕ_B and ϕ_A at the opposite corners of the semi-circular cross-section, i.e. $\phi_B = \phi(R, 0, z)$, $\phi_A = \phi(R, \pi, z)$ and $\rho = R$. (b) Electric potential $\phi(\rho, 0, L)$ as a function of the radial position ρ, obtained from the simplified analytical model and simulation. The inset shows the distribution of the normalized radial electric field E_ρ on the flat surface of the beam obtained from the simulation. The electric field diminishes by approaching the beam edges due to the charge-free surface boundary condition $\mathbf{D} \cdot \mathbf{n} = 0$, consequently leading to a decrease in electric potential. This effect is not captured in the simplified analytical model.

the electric potential on the flat surface of the free-end cross-section as a function of the radial coordinate, i.e. $\phi(\rho, 0, L)$. The analytical estimate is obtained from Eq. (6.13), using the antisymmetry of the field $\phi(\rho, \pi, L)$ = -$\phi(\rho, 0, L)$, as

$$\phi(\rho, 0, L) = \frac{\pi\rho P_\theta^a(\rho, L)}{2\kappa}. \tag{6.16}$$

showing the radial distribution of the electric potential along the flat surface of the cross-section at the free-end, i.e. $\phi(\rho, 0, L)$ obtained from the solution of the flexoelectric boundary value problem. The simplified analytical model overestimates the flexoelectrically generated electric potential, particularly at the lateral surface of the half truncated cone. The charge-free surface boundary condition, $\mathbf{D} \cdot \mathbf{n} = 0$, on the lateral surface forces the electric field $\mathbf{E} = -\nabla\phi$ to diminish as it approaches the lateral surface $\bar{\rho} = 1$, cf. inset in Fig. 6.12. Consequently, the induced electric potential decreases with respect to the simplified analytical solution. This effect is not captured by the analytical estimate.

We define the deviation of the estimate with respect to the self-consistent solution as

$$\mathcal{D}(\rho, z; R_1, R_2, L, E, \nu, \kappa, \mu_\ell, \mu_t, \mu_s) = \frac{P^a_\theta(\rho, z; R_1, R_2, L, E, \nu, \mu_s)}{P_\theta(\rho, z; R_1, R_2, L, E, \nu, \kappa, \mu_\ell, \mu_t, \mu_s)}, \tag{6.17}$$

where P_θ and P^a_θ are given in Eqs. (6.13) and (6.15), respectively. To systematically study this deviation, we perform a number of simulations considering different geometries and material parameters. We have observed a small variation in $\mathcal{D}$ (not shown) by changing the configuration and elastic properties, since the corresponding parameters R_1, R_2, L, J_s and G have already encoded these changes in the analytical model in Eq. (6.15). However, a considerable variation in $\mathcal{D}$ occurs by considering non-zero values for the longitudinal μ_ℓ and transversal μ_t coefficients of flexoelectricity. The main reason is due to additional effects of warping since the out-of-plane displacement u_z induces other non-zero strain gradient components as reported in Eqs. (6.3), which in turn activate the longitudinal and transversal components of flexoelectricity, contaminating the pure shear flexoelectric response. Since the strongest response is induced over the free-end semi-circular surface, we quantify the deviation $\mathcal{D}_v = \mathcal{D}(R_2, L)$ by performing a number of simulations using different values of μ_ℓ and μ_t. Figure 6.13(a) presents the results which can be summarized by the following fit:

$$\begin{aligned}\mathcal{D}_v(\mu_\ell, \mu_t) =& f_{00} + f_{10}\mu_\ell + f_{01}\mu_t + f_{20}\mu_\ell^2 + f_{11}\mu_\ell\mu_t && (6.18)\\ &+ f_{02}\mu_t^2 + f_{30}\mu_\ell^3 + f_{21}\mu_\ell^2\mu_t + f_{12}\mu_\ell\mu_t^2 + f_{03}\mu_t^3 && (6.19)\\ &+ f_{31}\mu_\ell^3\mu_t + f_{22}\mu_\ell^2\mu_t^2 + f_{13}\mu_\ell\mu_t^3 + f_{04}\mu_t^4, && (6.20)\end{aligned}$$

where the f coefficients are presented in Table 6.2. A noticeable deviation is observed in Fig. 6.13(b) by considering a non-zero value for either the flexoelectric coefficient μ_ℓ or μ_t. Equation (6.20) provides a practical way to quantify this deviation and correct the simplified analytical estimation in Eq. (6.15).

TABLE 6.2: f coefficients

f_{00}	f_{10}	f_{01}	f_{20}	f_{11}	f_{02}	f_{30}
2.09	21.97	-19	160.6	-271.8	90.11	224.1
f_{21}	f_{12}	f_{03}	f_{31}	f_{22}	f_{13}	f_{04}
-119.5	-493.1	230.3	7878	$-1.641e^4$	7993	2222

Finally, after providing an analytical expression for the deviation, we suggest a method to quantify the shear flexoelectric coefficient μ_s. This is done by expanding and rearranging Eq. (6.17) using Eqs. (6.13) and (6.15) as

$$\mu_s = \frac{\kappa \mathcal{D}_v L J_s G \Delta\phi}{4\pi T R_2 (R_1 - R_2)}, \tag{6.21}$$

where $\Delta\phi = \phi(R_2, 0, L) - \phi(R_2, \pi, L)$. This equation could be employed for two purposes:

- To validate computational models of flexoelectricity. In this case, by considering the same parameters of the simulation model and the voltage difference $\Delta\phi$ obtained from the simulation results, Eq. (6.21) should give the same value of μ_s used in the simulation, in order to validate the model.
- To quantify the shear flexoelectric coefficient μ_s from experimental measurements. By using the configuration and material parameters of the sample, the applied torque

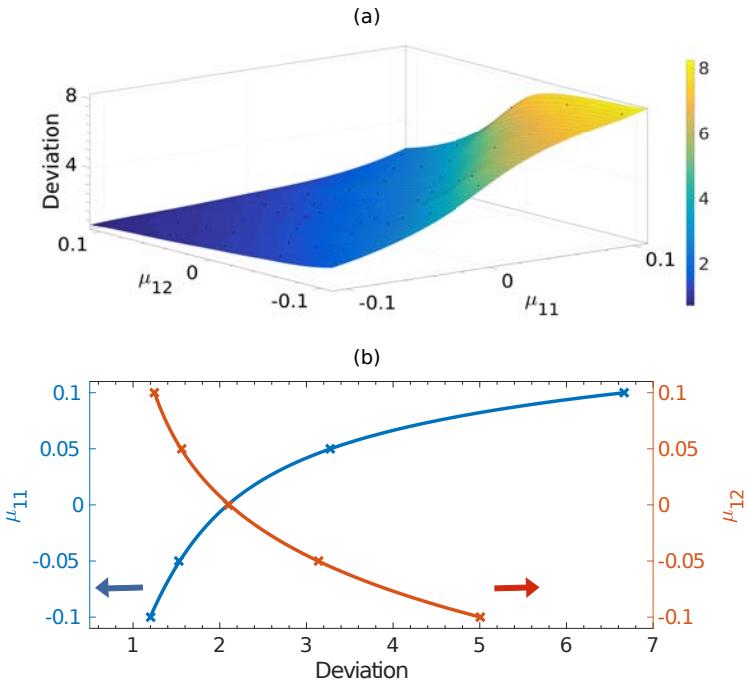

FIGURE 6.13: a) Deviation between the simulation and analytical results as a function of the longitudinal μ_l and transversal μ_t flexoelectric coefficients. (b) Cross-sections of the deviation plot where $\mu_l = 0$ (right) and $\mu_t = 0$ (left).

and the voltage difference $\Delta\phi$ obtained from the experimental measurement, Eq. (6.21) calculates the value of μ_s for the tested flexoelectric material.

The results presented in this section have been extrapolated and modified from [63][2].

6.4 Concluding remarks

Even though torsion of thin rods is a canonical means of generating large strain gradients, flexoelectricity had been barely examined in this setting. Here, based on simplified analytical derivations and supported by 3D self-consistent electromechanical calculations we have investigated several flexoelectric rods under torsion. We have shown that no polarization can be induced in ordinary flexoelectric cylindrical rods, irrespective of their cross-sections. Longitudinal gradients can be obtained in truncated conical geometries, and well-defined domain patterns have been observed. Focusing on the cubic symmetry of paraelectric ceramics with high flexocoupling, we have shown that the symmetry of the domains is directly related to the symmetry of the flexoelectric tensor. Furthermore, the magnitude of the induced electric potential linearly depends on a measure of flexoelectric anisotropy and can be tuned by the geometry of the rod [62].

Further investigation suggests possible configurations to quantify the elusive shear flexoelectric coefficient in cubic perovskites [63]. A well-defined polarization in a particular setup (the half truncated cone) under torsion is produced and can be exploited to quantify the shear flexoelectricity. Simulation and analytical results of this polarization have been used to propose a simple equation to quantify the shear flexoelectric coefficient in cubic ferroelectrics. This equation suggests a practical opportunity for proper quantification of shear

[2] *A.Mocci, A.Abdollahi, and I.Arias. Flexoelectric bars under torsion: chasing the elusive shear flexoelectricity.* (To be submitted).

flexoelectricity as well as a validation benchmark for computational models of flexoelectricity.

Chapter 7

Conclusions and future work

Ubiquitous technologies involving sensing, actuation, and energy harvesting rely on piezoelectricity, supported by a restricted class of materials, which introduces limiting trade-offs regarding performance, toughness, toxicity or operating temperature. The main contribution of this work is the identification of general geometrical rules to turn a micro-architected metamaterial into a piezoelectric. Other important contributions of this Ph.D. thesis are summarized next.

We have proposed a new class of geometrically-polarized lattice architecture achieving significant piezoelectricity. The non-piezoelectric constituents at the small-scale are arranged in such a way that can mobilize the flexoelectric effect and make it available at the meso- or macro-scale as apparent piezoelectricity. Low-weight and high-stiffness is generally required in structural applications where stretching-dominated structures are generally preferred. However, since our objective of maximizing the gradients and efficiently exploit the flexoelectricity of the micro-constituents, we opted for bending-dominated structures with low connectivity. Assisted by an accurate self-consistent computational model we have characterized and quantified their longitudinal performance accounting for the response aligned with the loading direction. The effect of volume fraction was found to be nontrivial. Reducing thickness, indeed, leads to slender constituents which can in principle mobilize more gradients nevertheless it also leads to a competition with the reduced amount of active material. We have also studied the highly anisotropic behavior of our geometries and identified the preferential orientation combined with the optimal volume fraction. By comparison with values for well-known piezoelectrics we predict that for a base material with a sufficient flexoelectric coupling, we could reach significant pressure or stress sensors comparable to PZT and quartz while measuring displacement response in actuation mode competitive to quartz and not far from PZT. Thus, according to our results, our designs favorably compete with the best piezoelectric when using good flexoelectric ceramics and feature sizes of about 100 nm. Although challenging, fabricating such materials is possible thanks to recent advances in microfabrication as discussed in Section 3.3. Furthermore, exploiting the recently demonstrated flexoelectret effect, it should be possible to implement our ideas using soft materials with millimeter-sized features, and thus much easier to fabricate. This scenario is particularly appealing as geometrical instabilities in soft metamaterials may generate or modify its geometric polarization, and hence lead to tunable or switchable piezoelectricity. Interestingly, the growing field of buckling-induced shape transformations in mechanical metamaterials has not explored the control of centro-symmetry so far.

An efficient computational homogenization technique has also been proposed and employed to extend the understanding of our metamaterials, hence characterizing their overall

behavior. Due to this comprehensive analysis, we were able to identify the preferred operation mode for each design. Indeed, we spot that the longitudinal piezoelectric coefficient was not necessarily the larger for each design, but instead, the lattices exhibiting lower symmetries might perform better in shear or transverse mode.

We presented a systematic shape and material optimization study based on gradient and genetic algorithms. We concluded that more compliant designs able to accommodate the deformations are thus extremely suitable for stress sensors for which we predict performances comparable to the best piezoelectrics. We find a similar situation for actuators when displacements are measured. On the contrary, the competition between slenderness and amount of materials is evidently in favor of the latter when displacements are imposed or stress is measured. For these setups, stiffer structures with small unit cells and well-oriented constituents are preferred. However, we end by highlighting that low-area fraction lattices are ultimately not appropriate for measuring the stress mobilized by an applied electric field.

Besides imprinting polarity geometrically in a lattice metamaterial, the overall symmetry of the system can be broken through multimaterial arrangements and boundary conditions. This concept was explored in detail and designs for flexoelectric devices combining two materials were proposed, analyzed and quantified.

In view of extending our work to 3D we focused on establishing new building blocks for three-dimensional metamaterials involving more complex ways of mobilizing gradients. We presented a comprehensive study of flexoelectric rods under torsion in cubic ferroelectrics. As predicted by a simplified analytical calculation, the 3D self-consistent computational approach confirmed that no flexoelectric polarization can be induced in trivial geometrical setups such as cylindrical rods subjected to a constant torque. The longitudinal gradient induced by varying cross-sections along the rods axis leads to well-defined polarization domains in truncated conical rods under torsion. We have demonstrated that the symmetry of the polarization domains is directly related to the symmetry of the flexoelectric tensor, whereas a measure of its anisotropy determines its magnitude, which can be tuned by the geometrical parameters of the rod. In further investigations, we also suggested other possible configurations, such as the half truncated cone under torsion where a well-defined polarization was induced. This configuration was proposed as a means to quantify the shear flexoelectric coefficient. In addition, it represents and has been used [59] as a validation benchmark for computational models of flexoelectricity.

7.1 Future work

In this Ph.D. thesis, we have broadly investigated the behavior of the proposed 2D low-area fraction bending-dominated lattices. During the investigation process, we gained meaningful insights, nonetheless the final objective of this work would naturally be to extend our knowledge to 3D, where we expect that our designs may further enhance the effective piezoelectricity.

In two-dimension the topological design of our rational metamaterials was mainly guided by intuition, however, in 3D the design space for optimal concepts able to attain substantial effective piezoelectricity might be challenging to achieve. Topological rearrangements and

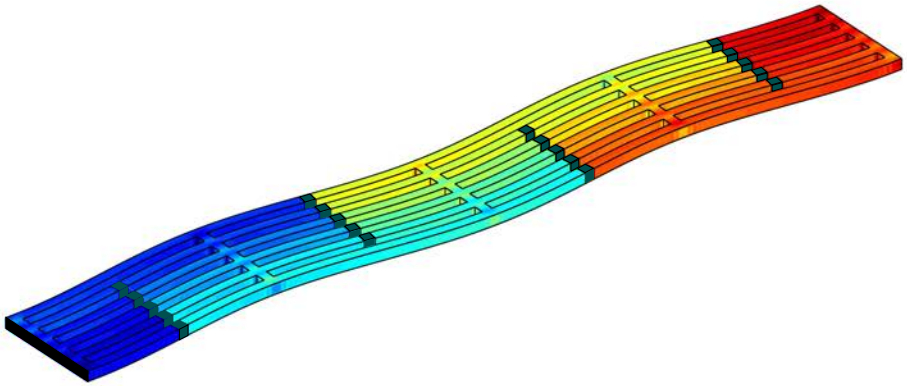

FIGURE 7.1: Electric potential distribution in the 3D extruded scalable flexoelectric device under bending.

alterations, as well as shape optimization based on genetic algorithm, are effective procedures that can lead to outstanding performances in non-trivial configurations. However, besides being computationally expensive these methods ensure no guarantees about the convergence to the global minimum, i.e. the certainly optimal design. Topology optimization is a mathematical method and design technology used to identify the optimal distribution of the material. Machine learning can be used to train artificial neural networks to identify patterns within the design space and target the optimal material configuration. Within a given design space, topology optimization at a first stage of the design process can provide a hint on the optimal spatial distribution of the micro-constituents, their orientation, and their mutual connections, yielding to an initial configuration plausibly closer to the optimal design and thereafter amenable for further parameters optimization analysis.

Traditionally, in structural applications, a critical issue is represented by elastic instabilities which are commonly prevented. As such instabilities are produced, dramatic changes in the static configuration are caused, generally leading to the failure of the structural elements. However, over the last decade, a new perspective has caught on. Elastic instabilities can be induced, controlled, and exploited in several operating systems [103], such as soft responsive and reconfigurable devices requiring wide changes in shape [175] or high-damping devices suitable for kinetic energy dissipation [176]. Buckling of thin structures can be easily achieved in soft materials, making it possible to conceive materials with tunable or switchable piezoelectricity provided that the buckling pattern introduces geometrical polarization.

Nested constituents at different length scales can be used to design hierarchical structures [136], ubiquitous in nature and engineered materials. Each constituent might mobilize more gradients, hence improving the performance of flexoelectric-based materials.

We end by mentioning that geometries including multi-material such as the scalable beam-bending flexoelectric device, presented in Ch. 3, (Fig. 3.4) could be easily extended to 3D. The iHB-Spline code and the required interface boundary conditions have already been tested in the 3D extruded lattice, shown in Fig. 7.1. Genuinely, a three-dimensional grid, with a well-defined path for the electric potential, will notably increase the scalability of the response. Moreover, optimization tools might assist us in detecting the finest material arrangement that lead to the optimal electric response.

Appendix A

Immersed boundary B-Spline framework

A.1 Material tensors

The material properties involved in the electromechanical bulk enthalpy defined in Eq. (2.2.1) and (2.2.2) are characterized by specifying the material tensors. Only non-zero components are specified.

Elasticity tensor C

The fourth-order tensor $\mathbb{C}$ characterizing isotropic elasticity is given by

$$\begin{aligned} \mathbb{C}_{iiii} &= C_l, && i = 1,2, \\ \mathbb{C}_{iijj} &= C_t, && i,j = 1,2 \quad \text{with} \quad i \neq j, \\ \mathbb{C}_{ijij} = \mathbb{C}_{ijji} &= C_s, && i,j = 1,2 \quad \text{with} \quad i \neq j, \end{aligned} \tag{A.1}$$

with C_l, C_t and C_s defined in 2D plain strain condition in terms of Young's modulus Y and Poisson's ratio ν as

$$C_l = \frac{Y(1-\nu)}{(1+\nu)(1-2\nu)}, \qquad C_t = \frac{Y\nu}{(1+\nu)(1-2\nu)}, \qquad C_s = \frac{Y}{2(1+\nu)}. \tag{A.2}$$

Strain gradient elasticity tensor h

A simplified form of isotropic strain-gradient elasticity is used, allowing us to write the sixth-rank strain-gradient tensor $\mathbf{h}$ in terms of these elastic parameters and a length-scale ℓ_{mech} [177, 178] as

$$\begin{aligned} h_{iikiik} &= \ell_{\text{mech}}^2 C_l, && i,k = 1,2, \\ h_{iikjjk} &= \ell_{\text{mech}}^2 C_t, && i,j,k = 1,2 \quad \text{with} \quad i \neq j, \\ h_{ijkijk} = h_{ijkjik} &= \ell_{\text{mech}}^2 C_s, && i,j,k = 1,2 \quad \text{with} \quad i \neq j. \end{aligned} \tag{A.3}$$

Dielectricity tensor κ

The second-order isotropic dielectricity tensor is written is terms of the dielectric permittivity ϵ as

$$\kappa_{ii} = \epsilon, \qquad i = 1, 2. \tag{A.4}$$

Electric field gradient dielectricity b

Analogously to the strain gradient elasticity, the fourth-order electric field gradient dielectricity tensor $\mathbf{b}$ is also defined in terms of κ_l and a second length scale parameter ℓ_{elec} as

$$b_{ijkl} = \epsilon \ell_{\text{elec}}^2 \delta_{ik} \delta_{jl}, \qquad i, j, k, l = 1, 2. \tag{A.5}$$

Flexoelectricity tensor μ

Flexoelectricity is characterized by a fourth-rank tensor, $\boldsymbol{\mu}$. Ferroelectric perovskites in their paraelectric phase belong to the cubic point group $m3m$ with only three independent flexoelectric components [32], namely longitudinal μ_ℓ, transverse μ_{t} and shear μ_{s}.

$$\begin{aligned} \mu_{iiii} &= \mu_\ell, & i &= 1, 2, \\ \mu_{ijji} &= \mu_t, & i, j &= 1, 2 \quad \text{with} \quad i \neq j, \\ \mu_{iijj} = \mu_{ijij} &= \mu_s, & i, j &= 1, 2 \quad \text{with} \quad i \neq j. \end{aligned} \tag{A.6}$$

For isotropic flexoelectricity, $\mu_{\text{s}} = \frac{1}{2}(\mu_{\text{l}} - \mu_{\text{t}})$ and only two independent components remain [33].

A.1.1 Strain gradient elasticity and electric field gradient dielectricity: sensitivity analysis

The elastic ℓ_{mech} and electric ℓ_{elec} length-scale parameters, in Eqs. (A.3) and (A.5), are required for stability of the formulation [59, 118].

Due to self-evident difficulties in the experimental quantification, the length-scale parameters are not well characterized to our knowledge and the choice of the right values is far from trivial. Here, we report a sensitivity analysis, for the flexoelectric cantilever beam under bending and for the lattice metamaterials discussed in the thesis. Different thicknesses have also been considered in the analysis.

Cantilever beam bending

At first, we performed the study in a flexoelectric cantilever beam defined by its thickness $t = 160\text{nm}$ and length $\ell = 1.28\mu\text{m}$. The contour plots in Fig. A.1 show the measured electric potential ϕ (Fig. A.1a), and mechanical deflection ψ (Fig. A.1b), respectively for sensor and actuator mode. The ℓ_{elec} length scale has no effect on the actuator mode, while it is negligible for sensor mode if compared with the effect of ℓ_{mech}. The study were repeated for beam having different thickness t ranging from $t = 40\text{nm}$ to $t = 400\text{nm}$, confirming the same response.

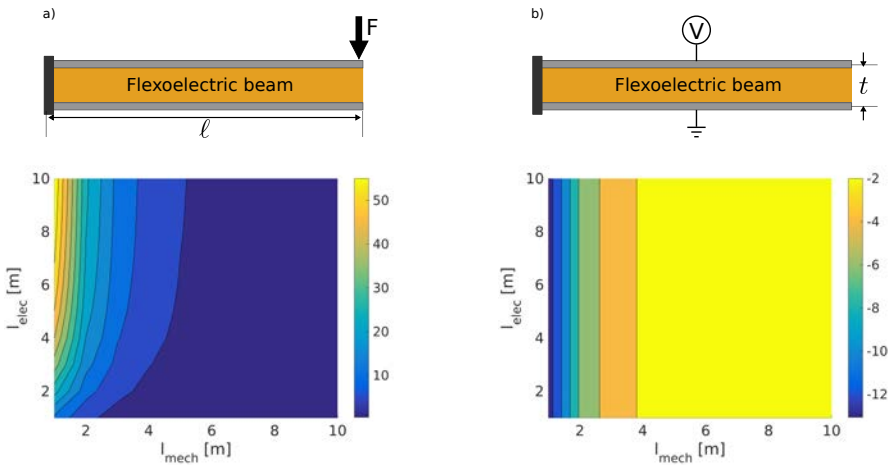

FIGURE A.1: Flexoelectric cantilever beam with thickness $t = 160$nm. (a) Sensor mode, a force F is enforced at the free end of the cantilever beam, the electric potential ϕ, reported in the contour plot, is measured at the top surface. (b) Actuator mode, an electric potential V is applied on the top face, while the bottom side has been grounded. The deflection φ is measured.

Bending-dominated lattice metamaterials

We repeated the same analysis for our lattice metamaterials. In Fig. A.2 we report the results of the analysis for Design D for $t = 40$nm and $t = 400$nm, for sensor (Fig. A.2a) and actuator (Fig. A.2b) mode, respectively. The red dot indicates the values for the two length-scale parameters that we used to perform our study.

In sensor mode (quantified by $\bar{\mathbf{h}}$) in Fig. A.2a, where electric field gradients are generated, the device is significantly more sensitive to the electric length-scale parameter ℓ_{elec}. By increasing the thickness of the constituents we observed a similar trend.

Focusing on actuator mode (quantified by $\bar{\mathbf{d}}$) in Fig. A.2b, the lattice appears now to be sensitive to both length-scale parameters. As expected, increasing the elastic length-scale, which controls the breakdown of local elasticity at small scales and depends on the microstructure of the material, results in a diminished response. We notice that this effect is strongly dependent on the beam thickness that characterized our lattice. As regards the electric length-scale parameter, we observed that for smaller values of ℓ_{elec} the local fields were entirely concentrated at the corners leading to oscillations of the solution and unphysical deformations. On the contrary higher values (closer to the pick region) allow us to mitigate the gradients and appreciate the bending of the constituents.

We perform a similar analysis for all the lattices, considering different beam thicknesses. Finally, the parameter ℓ_{mech} was chosen in the order given by [123], whereas, the ℓ_{elec} parameter was chosen as an average value such that our simulations remained stable and devoid of oscillations.

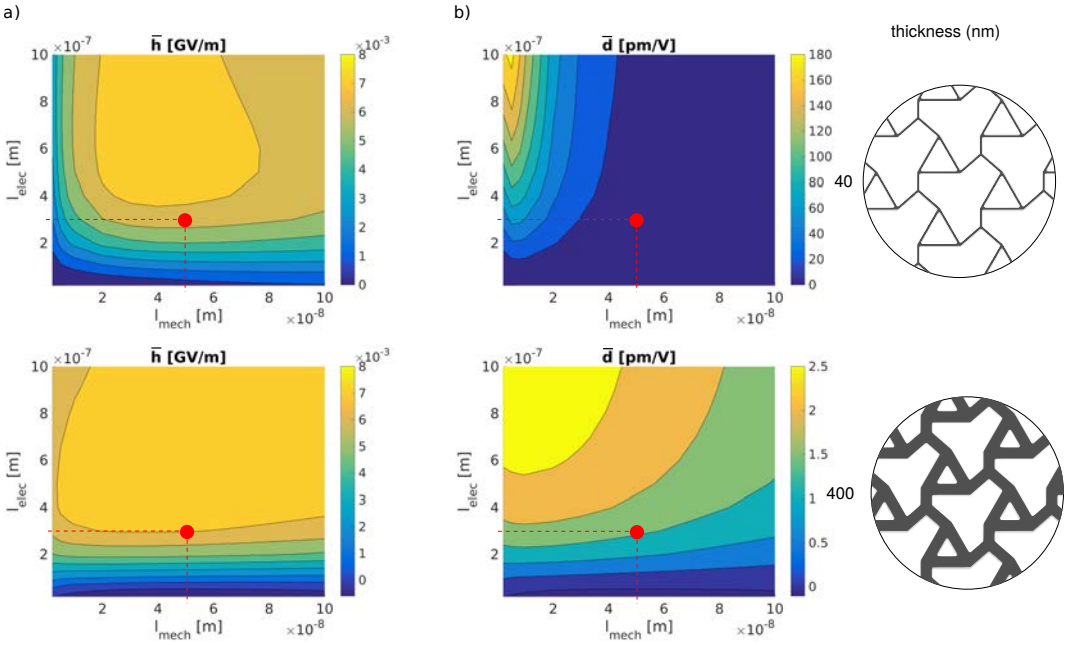

FIGURE A.2: Sensitivity analysis for Design D, with $t = 40$nm and $t = 400$nm.

Appendix B

Piezoelectric coefficients and boundary conditions derivation for the homogenized RVE

B.1 Piezoelectricity

In Eq. (3.1) we introduced four *effective* piezoelectric coupling coefficients to quantify the response of our metamaterials, each of them pertinent to a distinct sensing or actuation scenario and derived from a different form of the energy based upon different choice or set of independent variables, namely, stress, strain, electric field and electric displacement. The transition from one set to another is accomplished by the so called Legendre transformation.

The electric enthalpy $\mathcal{H}$, to which we mostly refer in this manuscript, leads to the direct derivation of e. Here, for completeness we will report the derivation of the four piezoelectric coefficients. Note that the aforementioned derivation follows classical piezoelectricity [5] and therefore in this section we will not refer to effective properties. The energy forms describe a piezoelectric (non-flexoelectric) uniform material.

B.1.1 Energy forms

Internal energy $\mathcal{U}\ (\boldsymbol{\varepsilon}, \mathbf{D})$, h-form

The incremental change in the internal energy $\mathcal{U}$ for a dielectric elastic body subjected to small changes in the strains and electric displacements is defined as:

$$\mathrm{d}\mathcal{U}(\varepsilon_{ij}, D_i) = \sigma_{ij}\,\mathrm{d}\varepsilon_{ij} + E_i\,\mathrm{d}D_i. \tag{B.1}$$

In this form of the energy the independent set of the variables are strain and electric displacement (ε_{kl}, D_k) . We can thus write the total derivative form of the strain energy density $\mathcal{U}$ as

$$\mathrm{d}\mathcal{U}(\varepsilon_{ij}, D_i) = \left.\frac{\partial \mathcal{U}}{\partial \varepsilon_{ij}}\right|_{\mathbf{D}} \mathrm{d}\varepsilon_{ij} + \left.\frac{\partial \mathcal{U}}{\partial D_i}\right|_{\boldsymbol{\varepsilon}} \mathrm{d}D_i. \tag{B.2}$$

Upon comparing (B.1) and (B.2),

$$\left.\frac{\partial \mathcal{U}}{\partial \varepsilon_{ij}}\right|_{\mathbf{D}} = \sigma_{ij}, \quad \left.\frac{\partial \mathcal{U}}{\partial D_i}\right|_{\boldsymbol{\varepsilon}} = E_i. \tag{B.3}$$

Since $(\boldsymbol{\varepsilon}, \mathbf{D})$ are independent variables, it implies that stresses and electric fields can be related to strains and electric displacements as:

$$\mathrm{d}\sigma_{ij}(\varepsilon_{kl}, D_k) = \left.\frac{\partial \sigma_{ij}}{\partial \varepsilon_{kl}}\right|_{\mathbf{D}} \mathrm{d}\varepsilon_{kl} + \left.\frac{\partial \sigma_{ij}}{\partial D_k}\right|_{\boldsymbol{\varepsilon}} \mathrm{d}D_k, \tag{B.4}$$

$$\mathrm{d}E_i(\varepsilon_{kl}, D_k) = \left.\frac{\partial E_i}{\partial \varepsilon_{kl}}\right|_{\mathbf{D}} \mathrm{d}\varepsilon_{kl} + \left.\frac{\partial E_i}{\partial D_k}\right|_{\boldsymbol{\varepsilon}} \mathrm{d}D_k. \tag{B.5}$$

This leads to the standard definition of the third-order piezoelectric tensor $\mathbf{h}$ for both the direct and converse effect

$$h_{kij} = -\left.\frac{\partial \sigma_{ij}}{\partial D_k}\right|_{\boldsymbol{\varepsilon}} = -\left.\frac{\partial}{\partial D_k}\right|_{\boldsymbol{\varepsilon}} \left.\frac{\partial \mathcal{U}}{\partial \varepsilon_{ij}}\right|_{\mathbf{D}} = -\left.\frac{\partial}{\partial \varepsilon_{ij}}\left(\left(\frac{\partial \mathcal{U}}{\partial D_k}\right)\right|_{\boldsymbol{\varepsilon}}\right)\right|_{\mathbf{D}} = -\left.\frac{\partial E_k}{\partial \varepsilon_{ij}}\right|_{\mathbf{D}}. \tag{B.6}$$

Gibbs energy Φ $(\sigma, \mathbf{E})$, d-form

To convert the independent set of variables from strain and electric displacement (ε_{ij}, D_i) to stress and electric field (σ_{ij}, E_i), we use *Legendre Transformation*. Hence we define a new function Φ (Gibbs function) as

$$\Phi(\sigma_{ij}, E_i) = U - \sigma_{ij}\varepsilon_{ij} - E_i D_i. \tag{B.7}$$

Upon differentiating the above equation and substituting (B.1), we obtain:

$$\mathrm{d}\Phi(\sigma_{ij}, E_i) = -\varepsilon_{ij}\,\mathrm{d}\sigma_{ij} - D_i\,\mathrm{d}E_i. \tag{B.8}$$

Hence, we again notice that Φ now solely depends on (σ_{ij}, E_i), therefore its total derivative appears as

$$\mathrm{d}\Phi(\sigma_{ij}, E_i) = \left.\frac{\partial \Phi}{\partial \sigma_{ij}}\right|_{\mathbf{E}} \mathrm{d}\sigma_{ij} + \left.\frac{\partial \Phi}{\partial E_i}\right|_{\sigma} \mathrm{d}E_i. \tag{B.9}$$

Thus, upon comparing,

$$\left.\frac{\partial \Phi}{\partial \sigma_{ij}}\right|_{\mathbf{E}} = -\varepsilon_{ij}, \quad \left.\frac{\partial \Phi}{\partial E_i}\right|_{\sigma} = -D_i. \tag{B.10}$$

As $(\boldsymbol{\sigma}, \mathbf{E})$ are independent variables, it implies that strains and electric displacements can be related to stresses and electric fields as

$$\mathrm{d}\varepsilon_{ij}(\sigma_{kl}, E_k) = \left.\frac{\partial \varepsilon_{ij}}{\partial \sigma_{kl}}\right|_{\mathbf{E}} \mathrm{d}\sigma_{kl} + \left.\frac{\partial \varepsilon_{ij}}{\partial E_k}\right|_{\sigma} \mathrm{d}E_k, \tag{B.11}$$

$$\mathrm{d}D_i(\sigma_{kl}, E_k) = \left.\frac{\partial D_i}{\partial \sigma_{kl}}\right|_{\mathbf{E}} \mathrm{d}\sigma_{kl} + \left.\frac{\partial D_i}{\partial E_k}\right|_{\sigma} \mathrm{d}E_k. \tag{B.12}$$

It follows the definition of the third-order piezoelectric tensor **d** for both the direct and converse effect

$$d_{kij} = \left.\frac{\partial \varepsilon_{ij}}{\partial E_k}\right|_{\sigma} = -\left(\frac{\partial}{\partial \sigma_{ij}}\left(\frac{\partial \Phi}{\partial E_k}\right)\Bigg|_{\sigma}\right)\Bigg|_{\mathbf{E}} = \left.\frac{\partial D_k}{\partial \sigma_{ij}}\right|_{\mathbf{E}}. \tag{B.13}$$

Electric enthalpy $\mathcal{H}$ $(\varepsilon, \mathbf{E})$, e-form

To convert the independent set of variables from strain and electric displacement (ε_{ij}, D_i) to strain and electric field (ε_{ij}, E_i), we use *Legendre Transformation*. Hence we define a new function $\mathcal{H}$ (electric enthalpy) as

$$\mathcal{H}(\varepsilon_{ij}, E_i) = \mathcal{U} - D_i E_i. \tag{B.14}$$

Upon differentiating the above equation and substituting (B.1), we obtain:

$$d\mathcal{H}(\varepsilon_{ij}, E_i) = \sigma_{ij} d\varepsilon_{ij} - D_i dE_i. \tag{B.15}$$

The electric enthalpy $\mathcal{H}$ now solely depends on (ε_{ij}, E_i), therefore its total derivative appears as

$$d\mathcal{H}(\varepsilon_{ij}, E_i) = \left.\frac{\partial \mathcal{H}}{\partial \varepsilon_{ij}}\right|_{\mathbf{E}} d\varepsilon_{ij} + \left.\frac{\partial \mathcal{H}}{\partial E_i}\right|_{\boldsymbol{\varepsilon}} dE_i. \tag{B.16}$$

Thus, upon comparing,

$$\left.\frac{\partial \mathcal{H}}{\partial \varepsilon_{ij}}\right|_{\mathbf{E}} = \sigma_{ij}, \quad \left.\frac{\partial \mathcal{H}}{\partial E_i}\right|_{\boldsymbol{\varepsilon}} = -D_i. \tag{B.17}$$

Being $(\boldsymbol{\varepsilon}, \mathbf{E})$ independent state variables, it implies that stresses and dielectric displacements can be related to strains and electric fields as

$$d\sigma_{ij}(\varepsilon_{kl}, E_k) = \left.\frac{\partial \sigma_{ij}}{\partial \varepsilon_{kl}}\right|_{\mathbf{E}} d\varepsilon_{kl} + \left.\frac{\partial \sigma_{ij}}{\partial E_k}\right|_{\boldsymbol{\varepsilon}} dE_k, \tag{B.18}$$

$$dD_i(\varepsilon_{kl}, E_k) = \left.\frac{\partial D_i}{\partial \varepsilon_{kl}}\right|_{\mathbf{E}} d\varepsilon_{kl} + \left.\frac{\partial D_i}{\partial E_k}\right|_{\boldsymbol{\varepsilon}} dE_k. \tag{B.19}$$

It follows the definition of the third-order piezoelectric tensor **e** for both the direct and converse effect

$$e_{ijk} = -\left.\frac{\partial \sigma_{ij}}{\partial E_k}\right|_{\boldsymbol{\varepsilon}} = \left(\frac{\partial}{\partial \varepsilon_{ij}}\left(\frac{\partial \mathcal{H}}{\partial E_k}\right)\Bigg|_{\boldsymbol{\varepsilon}}\right)\Bigg|_{\mathbf{E}} = \left.\frac{\partial D_k}{\partial \varepsilon_{ij}}\right|_{\mathbf{E}}. \tag{B.20}$$

Elastic Gibbs function $\mathcal{G}_1$ $(\sigma, \mathbf{D})$, g-form

To convert the independent set of variables from strain and electric displacement (ε_{ij}, D_i) to stress and electric displacement (σ_{ij}, D_i), we use *Legendre Transformation*. Hence we define a new function $\mathcal{G}$ (elastic Gibbs function) as

$$\mathcal{G}_1(\sigma_{ij}, D_i) = \mathcal{U} - \sigma_{ij}\varepsilon_{ij}. \tag{B.21}$$

Upon differentiating the above equation and substituting (B.1), we obtain:

$$d\mathcal{G}_1(\sigma_{ij}, D_i) = -\varepsilon_{ij} d\sigma_{ij} + E_i dD_i. \tag{B.22}$$

$\mathcal{G}_1$ now solely depends on (σ_{ij}, D_i), therefore its total derivative appears as

$$d\mathcal{G}_1(\sigma_{ij}, D_i) = \left.\frac{\partial \mathcal{G}_1}{\partial \sigma_{ij}}\right|_{\mathbf{D}} d\sigma_{ij} + \left.\frac{\partial \mathcal{G}_1}{\partial D_i}\right|_{\sigma} dD_i. \tag{B.23}$$

Thus, upon comparing,

$$\left.\frac{\partial \mathcal{G}_1}{\partial \sigma_{ij}}\right|_{\mathbf{D}} = -\varepsilon_{ij}, \quad \left.\frac{\partial \mathcal{G}_1}{\partial D_i}\right|_{\sigma} = E_i. \tag{B.24}$$

Being $(\sigma, \mathbf{D})$ independent state variables, it implies that stresses and dielectric displacements can be related to stress and electric displacement as

$$d\varepsilon_{ij}(\sigma_{kl}, D_k) = \left.\frac{\partial \varepsilon_{ij}}{\partial \sigma_{kl}}\right|_{\mathbf{D}} d\sigma_{kl} + \left.\frac{\partial \varepsilon_{ij}}{\partial D_k}\right|_{\sigma} dD_k, \tag{B.25}$$

$$dE_i(\sigma_{kl}, D_k) = \left.\frac{\partial E_i}{\partial \sigma_{kl}}\right|_{\mathbf{D}} d\sigma_{kl} + \left.\frac{\partial E_i}{\partial D_k}\right|_{\sigma} dD_k. \tag{B.26}$$

It follows the definition of the third-order piezoelectric tensor $\mathbf{g}$ for both the direct and converse effect

$$g_{ijk} = \left.\frac{\partial \varepsilon_{ij}}{\partial D_k}\right|_{\sigma} = \left.\left(\frac{\partial}{\partial \sigma_{ij}}\left(\frac{\partial \mathcal{G}_1}{\partial D_k}\right)\right|_{\sigma}\right)\right|_{\mathbf{D}} = -\left.\frac{\partial E_k}{\partial \sigma_{ij}}\right|_{\mathbf{D}}. \tag{B.27}$$

B.1.2 Relationship between piezoelectric tensors

The four piezoelectric coefficients are related to one another through the elasticity and dielectricity tensors or their inverse. For the sake of clarity, here we show the relationship

between all the above forms for linear constitutive relation:

$$h^c_{ijk} = -\left.\frac{\partial \sigma_{ij}}{\partial D_k}\right|_{\varepsilon} = -\left.\frac{\partial \sigma_{ij}}{\partial E_n}\right|_{\varepsilon}\left.\frac{dE_n}{dD_k}\right|_{\varepsilon} = e^c_{ijn}\beta^{\varepsilon}_{nk}, \tag{B.28a}$$

$$h^d_{ijk} = -\left.\frac{\partial E_k}{\partial \varepsilon_{ij}}\right|_{\mathbf{D}} = -\left.\frac{\partial E_k}{\partial \sigma_{mn}}\right|_{\mathbf{D}}\left.\frac{d\sigma_{mn}}{d\varepsilon ij}\right|_{\mathbf{D}} = g^d_{mnk}C^{\mathbf{D}}_{mnij}, \tag{B.28b}$$

$$d^c_{ijk} = \left.\frac{\partial \varepsilon_{ij}}{\partial E_k}\right|_{\sigma} = \left.\frac{\partial \varepsilon_{ij}}{\partial D_n}\right|_{\sigma}\left.\frac{dD_n}{dE_k}\right|_{\sigma} = g^c_{ijn}\kappa^{\sigma}_{nk}, \tag{B.28c}$$

$$d^d_{ijk} = \left.\frac{\partial D_k}{\partial \sigma_{ij}}\right|_{\mathbf{E}} = \left.\frac{\partial D_k}{\partial \varepsilon_{mn}}\right|_{\mathbf{E}}\left.\frac{d\varepsilon_{mn}}{d\sigma_{ij}}\right|_{\mathbf{E}} = e^d_{mnk}S^{\mathbf{E}}_{mnij}, \tag{B.28d}$$

$$e^c_{ijk} = -\left.\frac{\partial \sigma_{ij}}{\partial E_k}\right|_{\varepsilon} = -\left.\frac{\partial \sigma_{ij}}{\partial D_n}\right|_{\varepsilon}\left.\frac{dD_n}{dE_k}\right|_{\varepsilon} = h^c_{ijn}\kappa^{\varepsilon}_{nk}, \tag{B.28e}$$

$$e^d_{ijk} = \left.\frac{\partial D_k}{\partial \varepsilon_{ij}}\right|_{\mathbf{E}} = \left.\frac{\partial D_k}{\partial \sigma_{mn}}\right|_{\mathbf{E}}\left.\frac{d\sigma_{mn}}{d\varepsilon ij}\right|_{\mathbf{E}} = d^d_{mnk}C^{\mathbf{E}}_{mnij}, \tag{B.28f}$$

$$g^c_{ijk} = \left.\frac{\partial \varepsilon_{ij}}{\partial D_k}\right|_{\sigma} = \left.\frac{\partial \varepsilon ij}{\partial E_n}\right|_{\sigma}\left.\frac{dE_n}{dD_k}\right|_{\sigma} = d^c_{ijn}\beta^{\sigma}_{nk}, \tag{B.28g}$$

$$g^d_{ijk} = -\left.\frac{\partial E_k}{\partial \sigma_{ij}}\right|_{\mathbf{D}} = -\left.\frac{\partial E_k}{\partial \varepsilon_{mn}}\right|_{\mathbf{D}}\left.\frac{d\varepsilon_{mn}}{d\sigma_{ij}}\right|_{\mathbf{D}} = h^d_{mnk}S^{\mathbf{D}}_{mnij}, \tag{B.28h}$$

where $\boldsymbol{C}$ is the elasticity tensor, $\boldsymbol{\kappa}$ is the dielectricity tensor, $\boldsymbol{S}$ is the inverse of the elasticity tensor, i.e. the compliance tensor, and $\boldsymbol{\beta}$ the inverse of the dielectricity tensor, while ^{d} and ^{c} refer to direct and converse piezoelectricity, respectively.

B.2 Tensor surface representation

Once defined the effective material tensors, all the material properties can be graphically represented through surfaces that contain the overall information about the homogenized medium. The 3D surface representation is expressed in spherical coordinates, sketched in Fig. B.1. Given a point P, it can be expressed by the *polar angle* θ representing the angle between the zenith direction k and OP and conventionally assumed $0 < \theta < \pi$, the *azimuthal angle* $0 < \phi < 2\pi$ measured between the azimuth reference direction i and the projection of OP on the reference plane $\langle iOj \rangle$, and the *radial distance* r from the origin O to P. The spherical coordinate representation of tensors are specified by the orthonormal basis $\{e_r, e_\theta, e_\phi\}$.

Here, for sake of brevity, we will only illustrate the procedure to obtain the surface representation for the second-order dielectric tensor, however other rank tensors such as elasticity and piezoelectric can be plotted following the same process.

After transforming our Cartesian tensor in Voigt notation we evaluate a scalar function $f(x, y, z)$ such that

$$f(x,y,z) = \begin{pmatrix} x & y & z \end{pmatrix}\begin{pmatrix} \kappa_{11} & \kappa_{12} & \kappa_{13} \\ \kappa_{21} & \kappa_{22} & \kappa_{23} \\ \kappa_{31} & \kappa_{32} & \kappa_{33} \end{pmatrix}\begin{pmatrix} x \\ y \\ z \end{pmatrix} = \kappa_{11}x^2 + \kappa_{12}yx + \kappa_{31}zx + ... + \kappa_{33}z^2. \tag{B.29}$$

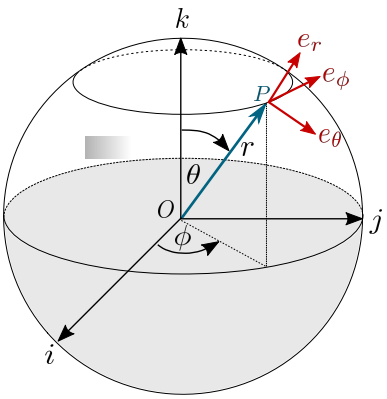

FIGURE B.1: Spherical reference system $Or\theta\phi$.

The Cartesian scalar function is thus transformed in a spherical coordinate system $f(x, y, z) \rightarrow f'(r, \theta, \phi)$ which contains all the information about our homogenized tensor and its symmetry and can thus be plotted in spherical coordinate.

Appendix C

Meshfree approximation method

C.1 Material characterization

The material properties involved in the electromechanical bulk enthalpy defined in Eq. (2.2.1) and (2.2.2) are characterized by specifying the material tensors, here we report all the tensors involved in Voigt notation as they are implemented.

Elasticity tensor C

The fourth-order tensor **C** charcaterizing isotropic elasticity is given by

$$\boldsymbol{C} = \begin{bmatrix} C_l & C_t & C_t & 0 & 0 & 0 \\ C_t & C_l & C_t & 0 & 0 & 0 \\ C_t & C_t & C_l & 0 & 0 & 0 \\ 0 & 0 & 0 & C_s & 0 & 0 \\ 0 & 0 & 0 & 0 & C_s & 0 \\ 0 & 0 & 0 & 0 & 0 & C_s \end{bmatrix}, \tag{C.1}$$

with C_l, C_t and C_s defined in 2D plain strain condition in terms of Young's modulus Y and Poisson's ratio ν as

$$C_l = \frac{Y(1-\nu)}{(1+\nu)(1-2\nu)}, \qquad C_t = \frac{Y\nu}{(1+\nu)(1-2\nu)}, \qquad C_s = \frac{Y}{2(1+\nu)}. \tag{C.2}$$

Dielectricity tensor κ

The second-order isotropic dielectricity tensor is written in terms of dielectric permittivity ϵ as

$$\boldsymbol{\kappa} = \begin{bmatrix} \epsilon & 0 & 0 \\ 0 & \epsilon & 0 \\ 0 & 0 & \epsilon \end{bmatrix}, \tag{C.3}$$

Flexoelectricity tensor μ

Flexoelectricity is characterized by the fourth-rank tensor $\boldsymbol{mu}$. Ferroelectric perovskites in their paraelectric phase belong to the cubic point group $m3m$ with only three independent flexoelectric components[32], namely longitudinal $\mu_\ell = \mu_{11}$, transverse $\mu_\mathrm{t} = \mu_{12}$ and shear $\mu_\mathrm{s} = \mu_{44}$.

$$\boldsymbol{\mu} = \begin{bmatrix} \mu_{11} & 0 & 0 & \mu_{12} & 0 & 0 & \mu_{12} & 0 & 0 & 0 & \mu_{44} & 0 & 0 & 0 & \mu_{44} & 0 & 0 & 0 \\ 0 & \mu_{12} & 0 & 0 & \mu_{11} & 0 & 0 & \mu_{12} & 0 & \mu_{44} & 0 & 0 & 0 & 0 & 0 & 0 & 0 & \mu_{44} \\ 0 & 0 & \mu_{12} & 0 & 0 & \mu_{12} & 0 & 0 & \mu_{11} & 0 & 0 & 0 & \mu_{44} & 0 & 0 & 0 & \mu_{44} & 0 \end{bmatrix}, \tag{C.4}$$

where

$$\mu_{iiii} = \mu_\ell \qquad i = 1,2,3; \tag{C.5a}$$

$$\mu_{ijji} = \mu_t \qquad i = 1,2,3; \quad \text{such that} \quad i \neq j \tag{C.5b}$$

$$\mu_{iijj} = \mu_{ijij} = \mu_s \qquad i = 1,2,3; \quad \text{such that} \quad i \neq j, \tag{C.5c}$$

Gradient operators $\mathbf{B_u}$ and $\mathbf{B}_\phi$

The gradient operators can be written as

$$\boldsymbol{B}_\mathbf{u} = \begin{bmatrix} \frac{\partial}{\partial x} & 0 & 0 & \frac{\partial}{\partial y} & 0 & \frac{\partial}{\partial z} \\ 0 & \frac{\partial}{\partial y} & 0 & \frac{\partial}{\partial x} & \frac{\partial}{\partial z} & 0 \\ 0 & 0 & \frac{\partial}{\partial z} & 0 & \frac{\partial}{\partial y} & \frac{\partial}{\partial x} \end{bmatrix}, \tag{C.6}$$

and

$$\boldsymbol{B}_\phi = \begin{bmatrix} \frac{\partial}{\partial x} & \frac{\partial}{\partial y} & \frac{\partial}{\partial z} \end{bmatrix}. \tag{C.7}$$

Hessian operators $\mathbf{H_u}$ and $\mathbf{H}_\phi$

$$\boldsymbol{H}_\mathbf{u} = \begin{bmatrix} \frac{\partial^2}{\partial x^2} & \frac{\partial^2}{\partial x \partial y} & \frac{\partial^2}{\partial x \partial z} & 0 & 0 & 0 & 0 & 0 & 0 & \\ 0 & 0 & 0 & \frac{\partial^2}{\partial y \partial x} & \frac{\partial^2}{\partial y^2} & \frac{\partial^2}{\partial y \partial z} & 0 & 0 & 0 & \dots \\ 0 & 0 & 0 & 0 & 0 & 0 & \frac{\partial^2}{\partial z \partial x} & \frac{\partial^2}{\partial z \partial y} & \frac{\partial^2}{\partial z^2}. & \end{bmatrix}$$

$$\begin{bmatrix} \frac{\partial^2}{\partial y \partial x} & \frac{\partial^2}{\partial y^2} & \frac{\partial^2}{\partial y \partial z} & \frac{\partial^2}{\partial z \partial x} & \frac{\partial^2}{\partial z \partial y} & \frac{\partial^2}{\partial z^2} & 0 & 0 & 0 \\ \dots \quad \frac{\partial^2}{\partial x^2} & \frac{\partial^2}{\partial x \partial y} & \frac{\partial^2}{\partial x \partial z} & 0 & 0 & 0 & \frac{\partial^2}{\partial z \partial x} & \frac{\partial^2}{\partial z \partial y} & \frac{\partial^2}{\partial z^2} \\ 0 & 0 & 0 & \frac{\partial^2}{\partial x^2} & \frac{\partial^2}{\partial x \partial y} & \frac{\partial^2}{\partial x \partial z} & \frac{\partial^2}{\partial y \partial x} & \frac{\partial^2}{\partial y^2} & \frac{\partial^2}{\partial y \partial z} \end{bmatrix} \tag{C.8}$$

C.2 Derivation of the elastic torsion problem in cylindrical coordinates

The displacement field for the elastic torsion problem in cylindrical coordinates is written as

$$\begin{cases} u_\rho = 0, \\ u_\theta = \alpha(z)\rho z, \\ u_z = \alpha(z)\psi(\rho,\theta,z). \end{cases} \tag{C.9}$$

From here, the non-zero strain gradient components can be derived as reported below

$$\varepsilon_{zz,z} = \alpha''\psi + 2\alpha'\frac{\partial\psi}{\partial z} + \alpha\frac{\partial^2\psi}{\partial z^2}, \tag{C.10a}$$

$$\varepsilon_{zz,\theta} = \frac{1}{\rho}\left(\alpha'\frac{\partial\psi}{\partial\theta} + \alpha\frac{\partial^2\psi}{\partial\theta\partial z}\right), \tag{C.10b}$$

$$\varepsilon_{zz,\rho} = \frac{1}{\rho}\left(\alpha'\psi + \alpha\frac{\partial\psi}{\partial z}\right) + \alpha'\frac{\partial\psi}{\partial\rho} + \alpha\frac{\partial^2\psi}{\partial\rho\partial z}, \tag{C.10c}$$

$$\varepsilon_{\theta z,z} = \varepsilon_{z\theta,z} = \frac{1}{2}\left(\alpha''\rho z + 2\alpha'\rho + \frac{1}{\rho}\alpha'\frac{\partial\psi}{\partial\theta} + \frac{1}{\rho}\alpha\frac{\partial^2\psi}{\partial\theta\partial z}\right), \tag{C.10d}$$

$$\varepsilon_{\rho z,z} = \varepsilon_{z\rho,z} = \frac{\alpha}{2}\frac{\partial^2\psi}{\partial\rho\partial z}, \tag{C.10e}$$

$$\varepsilon_{\theta z,\theta} = \varepsilon_{z\theta,\theta} = \frac{\alpha}{2}\left(\frac{1}{\rho}\frac{\partial\psi}{\partial\rho} + \frac{\partial^2\psi}{\partial\rho^2}\right), \tag{C.10f}$$

where $\alpha' = \partial\alpha/\partial z$ and $\alpha'' = \partial^2\alpha/\partial z^2$.

C.3 Mesh and convergence

Axisymmetric structured meshes have been used in order to avoid mesh-dependent symmetries. Figure C.1(a) shows the electric potential distribution on a quarter cross-section obtained from simulations with two different meshes, where the second one (right) has been obtained upon rotation of the first one (left) by an angle $\zeta = 20$. The observed patterns agree perfectly and bear no relation with the computational mesh, thereby discarding any numerical artifact. Furthermore, the observed domain patterns are converged as illustrated in Figure C.1(b) showing that the electric potential distribution on a quarter cross-section is not affected by mesh refinement. All simulation results in the paper have been obtained with the finest mesh (right).

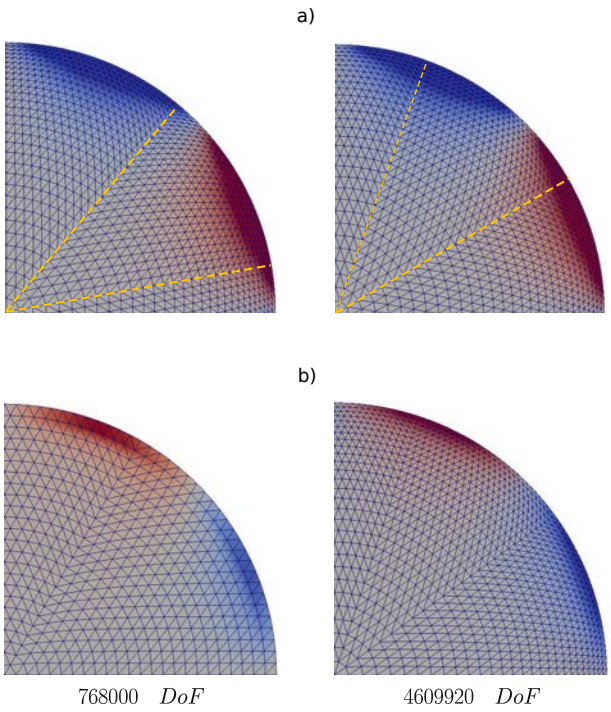

FIGURE C.1: (a) The rotation of the structured mesh by an angle $\zeta = 20$ degrees does not affect the generation of the patterns in the electric potential distribution. Yellow lines have been added to highlight the rotation of the mesh. (b) Convergence study of the numerical simulations. The electric potential distribution does not change upon mesh refinement.

Bibliography

[1] Canan Dagdeviren et al. “Recent progress in flexible and stretchable piezoelectric devices for mechanical energy harvesting, sensing and actuation”. In: *Extreme mechanics letters* 9 (2016), pp. 269–281.

[2] Gustav Gautschi. “Piezoelectric sensors”. In: *Piezoelectric Sensorics*. Springer, 2002, pp. 73–91.

[3] Mohsen Safaei, Henry A Sodano, and Steven R Anton. “A review of energy harvesting using piezoelectric materials: state-of-the-art a decade later (2008–2018)”. In: *Smart Materials and Structures* 28.11 (2019), p. 113001.

[4] Nipun Sinha et al. “Piezoelectric aluminum nitride nanoelectromechanical actuators”. In: *Applied Physics Letters* 95.5 (2009), p. 053106.

[5] Takuro Ikeda. *Fundamentals of piezoelectricity*. Oxford Science Publications. Oxford University Press, 1997.

[6] Jürgen Rödel et al. “Perspective on the development of lead-free piezoceramics”. In: *Journal of the American Ceramic Society* 92.6 (2009), pp. 1153–1177.

[7] B Jaffe, RS Roth, and S Marzullo. “Properties of Piezoelectric Cerdmics in the Solid-Solution”. In: *Journal of research of the National Bureau of Standards* 55 (1955), p. 239.

[8] Eric Cross. “Lead-free at last”. In: *Nature* 432.7013 (2004), pp. 24–25.

[9] Chang-Hyo Hong et al. “Lead-free piezoceramics–Where to move on?” In: *Journal of Materiomics* 2.1 (2016), pp. 1–24.

[10] Yasuyoshi Saito et al. “Lead-free piezoceramics”. In: *Nature* 432.7013 (2004), pp. 84–87.

[11] Jiagang Wu. “Perovskite lead-free piezoelectric ceramics”. In: *Journal of Applied Physics* 127.19 (2020), p. 190901.

[12] V Sundar and RE Newnham. “Electrostriction and polarization”. In: *Ferroelectrics* 135.1 (1992), pp. 431–446.

[13] David Codony. “Mathematical and computational modeling of flexoelectricity at mesoscopic and atomistic scales”. PhD thesis. Universitat Politècnica de Catalunya, 2021.

[14] VS Mashkevich and KB Tolpygo. “Electrical, optical and elastic properties of diamond type crystals”. In: *Sov. Phys. JETP* 5.3 (1957), pp. 435–439.

[15] Sh M Kogan. “Piezoelectric effect during inhomogeneous deformation and acoustic scattering of carriers in crystals”. In: *Soviet Physics-Solid State* 5.10 (1964), pp. 2069–2070.

[16] EV Bursian and ZAIKOVSK. OI. “Changes in curvature of a ferroelectric film due to polarization”. In: *Soviet Physics Solid State, USSR* 10.5 (1968), pp. 1121–+.

[17] Robert B Meyer. "Piezoelectric effects in liquid crystals". In: *Physical Review Letters* 22.18 (1969), p. 918.

[18] W Huang, F-G Yuan, and X Jiang. "Flexoelectric effect, materials, and structures". In: *Structural Health Monitoring (SHM) in Aerospace Structures*. Elsevier, 2016, pp. 119–148.

[19] M Marvan and A Havránek. "Flexoelectric effect in elastomers". In: *Relationships of Polymeric Structure and Properties*. Springer, 1998, pp. 33–36.

[20] Qian Deng, Liping Liu, and Pradeep Sharma. "Flexoelectricity in soft materials and biological membranes". In: *Journal of the Mechanics and Physics of Solids* 62 (2014), pp. 209–227.

[21] Matthew Grasinger, Kosar Mozaffari, and Pradeep Sharma. "Flexoelectricity in soft elastomers and the molecular mechanisms underpinning the design and emergence of giant flexoelectricity". In: *Proceedings of the National Academy of Sciences* 118.21 (2021).

[22] Dennis S Bruhn, Michael A Lomholt, and Himanshu Khandelia. "Quantifying the relationship between curvature and electric potential in lipid bilayers". In: *The Journal of Physical Chemistry B* 120.21 (2016), pp. 4812–4817.

[23] Haoyu Chen, Daniel Garcia-Gonzalez, and Antoine Jérusalem. "Computational model of the mechanoelectrophysiological coupling in axons with application to neuromodulation". In: *Physical Review E* 99.3 (2019), p. 032406.

[24] Kathryn D Breneman, William E Brownell, and Richard D Rabbitt. "Hair cell bundles: flexoelectric motors of the inner ear". In: *PLoS One* 4.4 (2009), e5201.

[25] Elisabetta Sassaroli and Natalia Vykhodtseva. "Acoustic neuromodulation from a basic science prospective". In: *Journal of therapeutic ultrasound* 4.1 (2016), pp. 1–14.

[26] Fabian Vasquez-Sancho et al. "Flexoelectricity in bones". In: *Advanced materials* 30.9 (2018), p. 1705316.

[27] Pavlo Zubko, Gustau Catalan, and Alexander K Tagantsev. "Flexoelectric effect in solids". In: *Annual Review of Materials Research* 43 (2013).

[28] P Ivaldi et al. "50 nm thick AlN film-based piezoelectric cantilevers for gravimetric detection". In: *Journal of Micromechanics and Microengineering* 21.8 (2011), p. 085023.

[29] Seok Ju Kang et al. "Printable ferroelectric PVDF/PMMA blend films with ultralow roughness for low voltage non-volatile polymer memory". In: *Advanced Functional Materials* 19.17 (2009), pp. 2812–2818.

[30] Amir Abdollahi and Irene Arias. "Constructive and destructive interplay between piezoelectricity and flexoelectricity in flexural sensors and actuators". In: *Journal of Applied Mechanics* 82.12 (2015).

[31] Longlong Shu et al. "Symmetry of flexoelectric coefficients in crystalline medium". In: *Journal of Applied Physics* 110.10 (2011), p. 104106.

[32] Longlong Shu et al. "Erratum:"Symmetry of flexoelectric coefficients in crystalline medium"[J. Appl. Phys. 110, 104106 (2011)]". In: *Journal of Applied Physics* 116.12 (2014), p. 129901.

[33] H Le Quang and Q-C He. "The number and types of all possible rotational symmetries for flexoelectric tensors". In: *Proceedings of the Royal Society A: Mathematical, Physical and Engineering Sciences* 467.2132 (2011), pp. 2369–2386.

[34] Amir Abdollahi et al. "Revisiting pyramid compression to quantify flexoelectricity: A three-dimensional simulation study". In: *Physical Review B* 91.10 (2015), p. 104103.

[35] L Eric Cross. "Flexoelectric effects: Charge separation in insulating solids subjected to elastic strain gradients". In: *Journal of Materials Science* 41.1 (2006), pp. 53–63.

[36] Wenhui Ma and L Eric Cross. "Large flexoelectric polarization in ceramic lead magnesium niobate". In: *Applied Physics Letters* 79.26 (2001), pp. 4420–4422.

[37] Wenhui Ma and L Eric Cross. "Flexoelectric polarization of barium strontium titanate in the paraelectric state". In: *Applied Physics Letters* 81.18 (2002), pp. 3440–3442.

[38] Wenhui Ma and L Eric Cross. "Flexoelectric effect in ceramic lead zirconate titanate". In: *Applied Physics Letters* 86.7 (2005), p. 072905.

[39] Wenhui Ma and L Eric Cross. "Flexoelectricity of barium titanate". In: *Applied Physics Letters* 88.23 (2006), p. 232902.

[40] Amir Abdollahi et al. "Computational evaluation of the flexoelectric effect in dielectric solids". In: *Journal of Applied Physics* 116.9 (2014), p. 093502.

[41] Wenyi Zhu et al. "Piezoelectric composite based on the enhanced flexoelectric effects". In: *Applied physics letters* 89.19 (2006), p. 192904.

[42] Umesh Kumar Bhaskar et al. "Flexoelectric MEMS: towards an electromechanical strain diode". In: *Nanoscale* 8.3 (2016), pp. 1293–1298.

[43] Wenbin Huang et al. "Flexoelectric strain gradient detection using Ba0. 64Sr0. 36TiO3 for sensing". In: *Applied Physics Letters* 101.25 (2012), p. 252903.

[44] Victor Ishrayelu Merupo et al. "Flexoelectric response in soft polyurethane films and their use for large curvature sensing". In: *Journal of Applied Physics* 122.14 (2017), p. 144101.

[45] X Yan et al. "Design of a curvature sensor using a flexoelectric material". In: *Sensors and Smart Structures Technologies for Civil, Mechanical, and Aerospace Systems 2013*. Vol. 8692. International Society for Optics and Photonics. 2013, 86920N.

[46] Lu Qi et al. "On the mechanics of curved flexoelectric microbeams". In: *International Journal of Engineering Science* 124 (2018), pp. 1–15.

[47] Longlong Shu et al. "Flexoelectric materials and their related applications: A focused review". In: *Journal of Advanced Ceramics* (2019), pp. 1–21.

[48] KF Wang and BL Wang. "Energy gathering performance of micro/nanoscale circular energy harvesters based on flexoelectric effect". In: *Energy* 149 (2018), pp. 597–606.

[49] Gustau Catalan et al. "Flexoelectric rotation of polarization in ferroelectric thin films". In: *Nature materials* 10.12 (2011), pp. 963–967.

[50] Haidong Lu et al. "Mechanical writing of ferroelectric polarization". In: *Science* 336.6077 (2012), pp. 59–61.

[51] Sung Min Park et al. "Selective control of multiple ferroelectric switching pathways using a trailing flexoelectric field". In: *Nature Nanotechnology* 13.5 (2018), pp. 366–370.

[52] Sana Krichen and Pradeep Sharma. "Flexoelectricity: A perspective on an unusual electromechanical coupling". In: *Journal of Applied Mechanics* 83.3 (2016).

[53] ND Sharma, Ravi Maranganti, and P Sharma. "On the possibility of piezoelectric nanocomposites without using piezoelectric materials". In: *Journal of the Mechanics and Physics of Solids* 55.11 (2007), pp. 2328–2350.

[54] Chang Liu, Huaping Wu, and Jie Wang. "Giant piezoelectric response in piezoelectric/dielectric superlattices due to flexoelectric effect". In: *Applied Physics Letters* 109.19 (2016), p. 192901.

[55] Qian Deng et al. "Nanoscale flexoelectric energy harvesting". In: *International Journal of Solids and Structures* 51.18 (2014), pp. 3218–3225.

[56] J Fousek, LE Cross, and DB Litvin. "Possible piezoelectric composites based on the flexoelectric effect". In: *Materials Letters* 39.5 (1999), pp. 287–291.

[57] John Y Fu et al. "Gradient scaling phenomenon in microsize flexoelectric piezoelectric composites". In: *Applied Physics Letters* 91.18 (2007), p. 182910.

[58] Baojin Chu et al. "Flexure mode flexoelectric piezoelectric composites". In: *Journal of Applied Physics* 106.10 (2009), p. 104109.

[59] David Codony et al. "An Immersed Boundary Hierarchical B-spline method for flexoelectricity". In: *Computer Methods in Applied Mechanics and Engineering* 354 (2019), pp. 750–782.

[60] Alice Mocci et al. "Geometrically polarized architected dielectrics with effective piezoelectricity". In: *Submitted for publication* (2021).

[61] Alice Mocci, Prakhar Gupta, and Irene Arias. "Shape optimization of architected dielectrics with effective piezoelectricity using computational homogenization". In: *In preparation* (2021).

[62] Alice Mocci, Amir Abdollahi, and Irene Arias. "Flexoelectricity in dielectrics under torsion." In: *Submitted for publication* (2020).

[63] Alice Mocci, Amir Abdollahi, and Irene Arias. "Flexoelectric bars under torsion: chasing the elusive shear flexoelectricity." In: *To be submitted* (2021).

[64] David Codony et al. "Wheel-shaped and helical torsional flexoelectric devices". In: *In preparation* (2021).

[65] Jordi Barceló-Mercader et al. "Generalized periodicity conditions for the computational modeling of flexoelectric metamaterials". In: *Submitted for publication* (2021).

[66] Raymond David Mindlin and NN Eshel. "On first strain-gradient theories in linear elasticity". In: *International Journal of Solids and Structures* 4.1 (1968), pp. 109–124.

[67] AK Tagantsev. "Piezoelectricity and flexoelectricity in crystalline dielectrics". In: *Physical Review B* 34.8 (1986), p. 5883.

[68] Alexander K Tagantsev. "Electric polarization in crystals and its response to thermal and elastic perturbations". In: *Phase Transitions: A Multinational Journal* 35.3-4 (1991), pp. 119–203.

[69] PV Yudin and AK Tagantsev. "Fundamentals of flexoelectricity in solids". In: *Nanotechnology* 24.43 (2013), p. 432001.

[70] Thanh D Nguyen et al. "Nanoscale flexoelectricity". In: *Advanced Materials* 25.7 (2013), pp. 946–974.

[71] MS Majdoub, P Sharma, and T Cagin. "Enhanced size-dependent piezoelectricity and elasticity in nanostructures due to the flexoelectric effect". In: *Physical Review B* 77.12 (2008), p. 125424.

[72] MS Majdoub, P Sharma, and T Çağin. "Erratum: Enhanced size-dependent piezoelectricity and elasticity in nanostructures due to the flexoelectric effect [Phys. Rev. B 77, 125424 (2008)]". In: *Physical Review B* 79.11 (2009), p. 119904.

[73] P Zubko et al. "Strain-gradient-induced polarization in SrTiO 3 single crystals". In: *Physical Review Letters* 99.16 (2007), p. 167601.

[74] Amir Abdollahi et al. "Fracture toughening and toughness asymmetry induced by flexoelectricity". In: *Physical Review B* 92.9 (2015), p. 094101.

[75] Xiaoying Zhuang et al. "Computational modeling of flexoelectricity—a review". In: *Energies* 13.6 (2020), p. 1326.

[76] E Amanatidou and N Aravas. "Mixed finite element formulations of strain-gradient elasticity problems". In: *Computer Methods in Applied Mechanics and Engineering* 191.15-16 (2002), pp. 1723–1751.

[77] John Y Shu, Wayne E King, and Norman A Fleck. "Finite elements for materials with strain gradient effects". In: *International Journal for Numerical Methods in Engineering* 44.3 (1999), pp. 373–391.

[78] Sheng Mao, Prashant K Purohit, and Nikolaos Aravas. "Mixed finite-element formulations in piezoelectricity and flexoelectricity". In: *Proceedings of the Royal Society A: Mathematical, Physical and Engineering Sciences* 472.2190 (2016), p. 20150879.

[79] Hamid Ghasemi, Harold S Park, and Timon Rabczuk. "A level-set based IGA formulation for topology optimization of flexoelectric materials". In: *Computer Methods in Applied Mechanics and Engineering* 313 (2017), pp. 239–258.

[80] BH Nguyen, X Zhuang, and Timon Rabczuk. "NURBS-based formulation for nonlinear electro-gradient elasticity in semiconductors". In: *Computer Methods in Applied Mechanics and Engineering* 346 (2019), pp. 1074–1095.

[81] Carl De Boor and Carl De Boor. *A practical guide to splines*. Vol. 27. springer-verlag New York, 1978.

[82] Charles S Peskin. "The immersed boundary method". In: *Acta numerica* 11 (2002), pp. 479–517.

[83] Rajat Mittal and Gianluca Iaccarino. "Immersed boundary methods". In: *Annu. Rev. Fluid Mech.* 37 (2005), pp. 239–261.

[84] Freddie D Witherden and Peter E Vincent. "On the identification of symmetric quadrature rules for finite element methods". In: *Computers & Mathematics with Applications* 69.10 (2015), pp. 1232–1241.

[85] William E Lorensen and Harvey E Cline. "Marching cubes: A high resolution 3D surface construction algorithm". In: *ACM siggraph computer graphics* 21.4 (1987), pp. 163–169.

[86] Onofre Marco et al. “Exact 3D boundary representation in finite element analysis based on Cartesian grids independent of the geometry”. In: *International Journal for Numerical Methods in Engineering* 103.6 (2015), pp. 445–468.

[87] Ruben Sevilla, Sonia Fernández-Méndez, and Antonio Huerta. “NURBS-enhanced finite element method (NEFEM)”. In: *International Journal for Numerical Methods in Engineering* 76.1 (2008), pp. 56–83.

[88] Ruben Sevilla and Sonia Fernández-Méndez. “Numerical integration over 2D NURBS-shaped domains with applications to NURBS-enhanced FEM”. In: *Finite Elements in Analysis and Design* 47.10 (2011), pp. 1209–1220.

[89] Klaus Höllig, Jörg Hörner, and Axel Hoffacker. “Finite element analysis with B-splines: weighted and isogeometric methods”. In: *International Conference on Curves and Surfaces*. Springer. 2010, pp. 330–350.

[90] Marino Arroyo and Michael Ortiz. “Local maximum-entropy approximation schemes: a seamless bridge between finite elements and meshfree methods”. In: *International journal for numerical methods in engineering* 65.13 (2006), pp. 2167–2202.

[91] Marino Arroyo and Michael Ortiz. “Local maximum-entropy approximation schemes”. In: *Meshfree methods for partial differential equations III*. Springer, 2007, pp. 1–16.

[92] Adrian Rosolen, Daniel Millán, and Marino Arroyo. “On the optimum support size in meshfree methods: a variational adaptivity approach with maximum-entropy approximants”. In: *International Journal for Numerical Methods in Engineering* 82.7 (2010), pp. 868–895.

[93] Victor Georgievich Veselago. “The Electrodynamics of Substances with Simultaneously Negative Values of ε and μ”. In: *Physics-Uspekhi* 10.4 (1968), pp. 509–514.

[94] Tie Jun Cui, David R Smith, and Ruopeng Liu. *Metamaterials*. Springer, 2010.

[95] Richard A Shelby, David R Smith, and Seldon Schultz. “Experimental verification of a negative index of refraction”. In: *science* 292.5514 (2001), pp. 77–79.

[96] Richard W Ziolkowski. “Metamaterial-inspired efficient electrically-small antennas: Designs and experiments”. In: *2007 International Workshop on Anti-Counterfeiting, Security and Identification (ASID)*. IEEE. 2007, pp. 4–4.

[97] Xiang Liu, Guoping Cai, and KW Wang. “Synthesizing and reconfiguring metastable modular metamaterials for adaptive wave propagation control”. In: *Journal of Sound and Vibration* 468 (2020), p. 115114.

[98] YY Chen and GL Huang. “Active elastic metamaterials for subwavelength wave propagation control”. In: *Acta Mechanica Sinica* 31.3 (2015), pp. 349–363.

[99] Vladimir M Shalaev. “Optical negative-index metamaterials”. In: *Nature photonics* 1.1 (2007), pp. 41–48.

[100] Steven A Cummer, Johan Christensen, and Andrea Alù. “Controlling sound with acoustic metamaterials”. In: *Nature Reviews Materials* 1.3 (2016), pp. 1–13.

[101] Xiaoyu Zheng et al. “Ultralight, ultrastiff mechanical metamaterials”. In: *Science* 344.6190 (2014), pp. 1373–1377.

[102] Lucas R Meza, Satyajit Das, and Julia R Greer. “Strong, lightweight, and recoverable three-dimensional ceramic nanolattices”. In: *Science* 345.6202 (2014), pp. 1322–1326.

[103] Katia Bertoldi et al. "Flexible mechanical metamaterials". In: *Nature Reviews Materials* 2.11 (2017), pp. 1–11.

[104] Sahab Babaee et al. "3D soft metamaterials with negative Poisson's ratio". In: *Advanced Materials* 25.36 (2013), pp. 5044–5049.

[105] H Coufal and A Mandelis. "Pyroelectric sensors for the photothermal analysis of condensed phases". In: *Ferroelectrics* 118.1 (1991), pp. 379–409.

[106] Zhi Yan. "Modeling of a piezoelectric/piezomagnetic nano energy harvester based on two dimensional theory". In: *Smart Materials and Structures* 27.1 (2017), p. 015016.

[107] Kenji Uchino. *Ferroelectric devices*. CRC press, 2018.

[108] Walter Heywang, Karl Lubitz, and Wolfram Wersing. *Piezoelectricity: evolution and future of a technology*. Vol. 114. Springer Science & Business Media, 2008.

[109] Gene H Haertling. "Ferroelectric ceramics: history and technology". In: *Journal of the American Ceramic Society* 82.4 (1999), pp. 797–818.

[110] Bernard Jaffe. *Piezoelectric ceramics*. Vol. 3. Elsevier, 2012.

[111] Thomas R Shrout et al. "High performance, high temperature perovskite piezoelectrics". In: *14th IEEE International Symposium on Applications of Ferroelectrics, 2004. ISAF-04. 2004*. IEEE. 2004, pp. 126–129.

[112] Roderic Lakes. "Elastic and viscoelastic behavior of chiral materials". In: *International journal of mechanical sciences* 43.7 (2001), pp. 1579–1589.

[113] Alberto Biancoli et al. "Breaking of macroscopic centric symmetry in paraelectric phases of ferroelectric materials and implications for flexoelectricity". In: *Nature materials* 14.2 (2015), pp. 224–229.

[114] Walter Guyton Cady. *Piezoelectricity: Volume Two: An Introduction to the Theory and Applications of Electromechanical Phenomena in Crystals*. Courier Dover Publications, 2018.

[115] Shashank Priya. "Advances in energy harvesting using low profile piezoelectric transducers". In: *Journal of electroceramics* 19.1 (2007), pp. 167–184.

[116] Swapnil Chandratre and Pradeep Sharma. "Coaxing graphene to be piezoelectric". In: *Applied Physics Letters* 100.2 (2012), p. 023114.

[117] Jordi Barceló-Mercader et al. "Nitsche's method for interfaces in flexoelectricity and application to periodic structures". In: *Submitted for publication* (2021).

[118] Sheng Mao and Prashant K Purohit. "Insights into flexoelectric solids from strain-gradient elasticity". In: *Journal of Applied Mechanics* 81.8 (2014).

[119] Dongchan Jang et al. "Fabrication and deformation of three-dimensional hollow ceramic nanostructures". In: *Nature materials* 12.10 (2013), pp. 893–898.

[120] Yanling Gao et al. "Nanocrystalline barium strontium titanate ceramics synthesized via the "organosol" route and spark plasma sintering". In: *Journal of the American Ceramic Society* 97.7 (2014), pp. 2139–2146.

[121] Bo Wang et al. "Flexoelectricity in solids: Progress, challenges, and perspectives". In: *Progress in Materials Science* 106 (2019), p. 100570.

[122] John Y Fu et al. "Experimental studies of the converse flexoelectric effect induced by inhomogeneous electric field in a barium strontium titanate composition". In: *Journal of Applied Physics* 100.2 (2006), p. 024112.

[123] R Maranganti and P Sharma. "Length scales at which classical elasticity breaks down for various materials". In: *Physical review letters* 98.19 (2007), p. 195504.

[124] P Hana. "Study of flexoelectric phenomenon from direct and from inverse flexoelectric behavior of PMNT ceramic". In: *Ferroelectrics* 351.1 (2007), pp. 196–203.

[125] VS Deshpande, MF Ashby, and NA Fleck. "Foam topology: bending versus stretching dominated architectures". In: *Acta materialia* 49.6 (2001), pp. 1035–1040.

[126] Christopher M Spadaccini. "Additive manufacturing and processing of architected materials". In: *MRS Bulletin* 44.10 (2019), pp. 782–788.

[127] John H Conway and Daniel H Huson. "The orbifold notation for two-dimensional groups". In: *Structural Chemistry* 13.3 (2002), pp. 247–257.

[128] AL Kholkin et al. "Piezoelectric and electrostrictive ceramics transducers and actuators: Smart ferroelectric ceramics for transducer applications". In: *Smart Materials*. CRC Press, 2008, pp. 9–1.

[129] Sarah Guerin and Damien Thompson. "Restriction boosts piezoelectricity". In: *Nature Materials* (2021), pp. 1–2.

[130] Muamer Kadic et al. "3D metamaterials". In: *Nature Reviews Physics* 1.3 (2019), pp. 198–210.

[131] Alexander K. Tagantsev and Alexander S. Yurkov. "Flexoelectric effect in finite samples". In: *Journal of Applied Physics* 112.4 (2012), p. 044103. DOI: 10.1063/1.4745037. eprint: http://dx.doi.org/10.1063/1.4745037. URL: http://dx.doi.org/10.1063/1.4745037.

[132] Julien Yvonnet, Xing Chen, and Pradeep Sharma. "Apparent flexoelectricity due to heterogeneous piezoelectricity". In: *Journal of Applied Mechanics* 87.11 (2020).

[133] Xin Wen et al. "Flexoelectret: an electret with a tunable flexoelectriclike response". In: *Physical review letters* 122.14 (2019), p. 148001.

[134] Xin Wen et al. "Inverse flexoelectret effect: bending dielectrics by a uniform electric field". In: *Physical Review Applied* 15.1 (2021), p. 014032.

[135] Martin Philip Bendsoe and Ole Sigmund. *Topology optimization: theory, methods, and applications*. Springer Science & Business Media, 2013.

[136] Lucas R Meza et al. "Resilient 3D hierarchical architected metamaterials". In: *Proceedings of the National Academy of Sciences* 112.37 (2015), pp. 11502–11507.

[137] Michel Bornert. *Homogenization in mechanics of materials*. ISTE USA, 2008.

[138] George Dvorak. *Micromechanics of composite materials*. Vol. 186. Springer Science & Business Media, 2012.

[139] D Guinovart-Sanjuán et al. "Effective predictions of heterogeneous flexoelectric multilayered composite with generalized periodicity". In: *International Journal of Mechanical Sciences* 181 (2020), p. 105755.

[140] Donald F Adams and Douglas R Doner. "Transverse normal loading of a unidirectional composite". In: *Journal of composite Materials* 1.2 (1967), pp. 152–164.

[141] Marc GD Geers, Varvara G Kouznetsova, and WAM Brekelmans. "Multi-scale computational homogenization: Trends and challenges". In: *Journal of computational and applied mathematics* 234.7 (2010), pp. 2175–2182.

[142] BA Le, Julien Yvonnet, and Q-C He. "Computational homogenization of nonlinear elastic materials using neural networks". In: *International Journal for Numerical Methods in Engineering* 104.12 (2015), pp. 1061–1084.

[143] EWC Coenen et al. "A multi-scale approach to bridge microscale damage and macroscale failure: a nested computational homogenization-localization framework". In: *International journal of fracture* 178.1-2 (2012), pp. 157–178.

[144] H Berger et al. "Finite element and asymptotic homogenization methods applied to smart composite materials". In: *Computational mechanics* 33.1 (2003), pp. 61–67.

[145] Harald Berger et al. "An analytical and numerical approach for calculating effective material coefficients of piezoelectric fiber composites". In: *International Journal of Solids and Structures* 42.21-22 (2005), pp. 5692–5714.

[146] Julien Yvonnet. *Computational homogenization of heterogeneous materials with finite elements*. Springer, 2019.

[147] Rodney Hill. "Elastic properties of reinforced solids: some theoretical principles". In: *Journal of the Mechanics and Physics of Solids* 11.5 (1963), pp. 357–372.

[148] Rodney Hill. "The essential structure of constitutive laws for metal composites and polycrystals". In: *Journal of the Mechanics and Physics of Solids* 15.2 (1967), pp. 79–95.

[149] Q-C He and Q-S Zheng. "On the symmetries of 2D elastic and hyperelastic tensors". In: *Journal of elasticity* 43.3 (1996), pp. 203–225.

[150] Sten Haastrup et al. "The Computational 2D Materials Database: high-throughput modeling and discovery of atomically thin crystals". In: *2D Materials* 5.4 (2018), p. 042002.

[151] Houssam Abdoul-Anziz, Nicolas Auffray, and Boris Desmorat. "Symmetry Classes and Matrix Representations of the 2D Flexoelectric Law". In: *Symmetry* 12.4 (2020), p. 674.

[152] Stefan J Rupitsch. *Piezoelectric sensors and actuators*. Springer, 2019.

[153] Mohammad H Malakooti and Henry A Sodano. "Piezoelectric energy harvesting through shear mode operation". In: *Smart Materials and Structures* 24.5 (2015), p. 055005.

[154] Dung-An Wang and Nine-Zeng Liu. "A shear mode piezoelectric energy harvester based on a pressurized water flow". In: *Sensors and actuators A: Physical* 167.2 (2011), pp. 449–458.

[155] Jihe Zhao et al. "Investigation of a d15 mode PZT-51 piezoelectric energy harvester with a series connection structure". In: *Smart materials and structures* 21.10 (2012), p. 105006.

[156] Henry A Sodano, Gyuhae Park, and DJ Inman. "Estimation of electric charge output for piezoelectric energy harvesting". In: *Strain* 40.2 (2004), pp. 49–58.

[157] ND Sharma, CM Landis, and P Sharma. "Piezoelectric thin-film superlattices without using piezoelectric materials". In: *Journal of Applied Physics* 108.2 (2010), p. 024304.

[158] Jorge Nocedal and Stephen Wright. *Numerical optimization*. Springer Science & Business Media, 2006.

[159] NA Fleck et al. "Strain gradient plasticity: theory and experiment". In: *Acta Metallurgica et materialia* 42.2 (1994), pp. 475–487.

[160] Y Huang et al. "Mechanism-based strain gradient plasticity—II. Analysis". In: *Journal of the Mechanics and Physics of Solids* 48.1 (2000), pp. 99–128.

[161] ACM Chong et al. "Torsion and bending of micron-scaled structures". In: *Journal of Materials Research* 16.4 (2001), pp. 1052–1058.

[162] KA Lazopoulos and AK Lazopoulos. "On the torsion problem of strain gradient elastic bars". In: *Mechanics Research Communications* 45 (2012), pp. 42–47.

[163] Shuwen Zhang et al. "Shear flexoelectric response along 3121 direction in polyvinylidene fluoride". In: *Applied Physics Letters* 107.14 (2015), p. 142902.

[164] Shuwen Zhang et al. "Investigation of the 2312 flexoelectric coefficient component of polyvinylidene fluoride: Deduction, simulation, and mensuration". In: *Scientific reports* 7.1 (2017), pp. 1–9.

[165] Alexander K Tagantsev, Eric Courtens, and Ludovic Arzel. "Prediction of a low-temperature ferroelectric instability in antiphase domain boundaries of strontium titanate". In: *Physical Review B* 64.22 (2001), p. 224107.

[166] Longlong Shu et al. "Converse flexoelectric coefficient f 1212 in bulk Ba0. 67Sr0. 33TiO3". In: *Applied Physics Letters* 104.23 (2014), p. 232902.

[167] Kaiyuan Liu et al. "Experimental decoupling of cylindrical flexoelectric coefficients". In: *Applied Physics Letters* 113.10 (2018), p. 102902.

[168] Kaiyuan Liu et al. "Decoupled shear flexoelectric effects in polymers". In: *Journal of Applied Physics* 125.17 (2019), p. 174104.

[169] IS Sokolnikoff. "Mathematical theory of elasticity". In: *Bull. Amer. Math. Soc* 52 (1946), pp. 976–978.

[170] Robert Asaro and Vlado Lubarda. *Mechanics of solids and materials*. Cambridge University Press, 2006.

[171] Z Yan and LY Jiang. "Flexoelectric effect on the electroelastic responses of bending piezoelectric nanobeams". In: *Journal of Applied Physics* 113.19 (2013), p. 194102.

[172] Xu Liang, Shuling Hu, and Shengping Shen. "Effects of surface and flexoelectricity on a piezoelectric nanobeam". In: *Smart materials and structures* 23.3 (2014), p. 035020.

[173] Runzhi Zhang, Xu Liang, and Shengping Shen. "A Timoshenko dielectric beam model with flexoelectric effect". In: *Meccanica* 51.5 (2016), pp. 1181–1188.

[174] J. Francu and P. Nováčková P. ans Janíček. "Torsion of non circular bar". In: *Engineering Mechanics, Vol. 19* (2012). URL: http://www.kmp.tul.cz/system/files/krouceni_nekruhoveho_hridele_francu.pdf.

[175] Johannes Tesse Bastiaan Overvelde, Sicong Shan, and Katia Bertoldi. "Compaction through buckling in 2D periodic, soft and porous structures: effect of pore shape". In: *Advanced Materials* 24.17 (2012), pp. 2337–2342.

[176] HW Yap, RS Lakes, and Robert W Carpick. "Negative stiffness and enhanced damping of individual multiwalled carbon nanotubes". In: *Physical Review B* 77.4 (2008), p. 045423.

[177] Raymond David Mindlin. *Microstructure in linear elasticity*. Tech. rep. Columbia Univ New York Dept of Civil Engineering and Engineering Mechanics, 1963.

[178] BS Altan and EC Aifantis. "On some aspects in the special theory of gradient elasticity". In: *Journal of the Mechanical Behavior of Materials* 8.3 (1997), pp. 231–282.

[179] A Cemal Eringen and DGB Edelen. "On nonlocal elasticity". In: *International journal of engineering science* 10.3 (1972), pp. 233–248.

[180] Janusz Dyszlewicz. *Micropolar theory of elasticity*. Vol. 15. Springer Science & Business Media, 2012.

[181] Yanmei Yue, Kaiyu Xu, and Elias C Aifantis. "Strain gradient and electric field gradient effects in piezoelectric cantilever beams". In: *Journal of the Mechanical Behavior of Materials* 24.3-4 (2015), pp. 121–127.